

Thermal Conductivity Measurements of Metal Hydrides as High Temperature Heat Storage Materials under Operating Conditions

Von der Fakultät für Ingenieurwissenschaften,
Abteilung Maschinenbau und Verfahrenstechnik der
Universität Duisburg-Essen

zur Erlangung des akademischen Grades
eines
Doktors der Ingenieurwissenschaften
Dr.-Ing.
genehmigte Dissertation

von

Rene Albert

aus

Berlin

Gutachter: Prof. Dr. Hartmut Wiggers

Gutachter: Prof. Dr. Ferdi Schüth

Tag der mündlichen Prüfung: 18.12.2019

DuEPublico

Duisburg-Essen Publications online

UNIVERSITÄT
DUISBURG
ESSEN

Offen im Denken

ub | universitäts
bibliothek

Diese Dissertation wird über DuEPublico, dem Dokumenten- und Publikationsserver der Universität Duisburg-Essen, zur Verfügung gestellt und liegt auch als Print-Version vor.

DOI: 10.17185/duepublico/71295

URN: urn:nbn:de:hbz:464-20200203-095914-4

Alle Rechte vorbehalten.

To my Family and my Friends

Acknowledgement

I am very grateful that Dr. Hartmut Wiggers accepted to be my supervisor for the Ph.D. and for the effort of proofreading the thesis and the fruitful discussions. I want to thank Professor Dr. Ferdi Schüth for the possibility to work in his department and giving me the chance to stay in such a friendly and supportive team. A big thanks goes to Michael for all support during the last years. Thank you for giving me opportunity to work on such an interesting topic and for the chance to be part of the metal-hydrogen science community.

I am grateful to:

Robert Urbanczyk for all the time he had, to discuss and teach me about engineering/scientific topics. For introducing me to my topic and for setting the bases of this work, without which I would not have had such a neat and smooth start in my research activities. Furthermore, a big thanks to him for his careful proofreading of this thesis and all the advices he gave me to completes this work.

Wolfgang, Knut, Sebastian, Ralf and the workshop of fine mechanics who constructed the measurement autoclaves with their unique experience for high pressure vessels. Furthermore, I really gratefully acknowledge that they always had time for fruitful discussions for the realization and improvement of the set-ups. Especially for the patience, helping me to get the measurement autoclaves leakage proof is acknowledged here. And thank you for all the nice interesting meetings, BBQs and celebrations which Wolfgang and his team have been hosting.

PD Dr. Claudia Weidenthaler and Jan Ternieden for all the XRD analysis and the fruitful discussions about the obtained results. Silvia Palm, Bernd Spliethoff and Hans Bongard are greatly acknowledged for investigating my samples by scanning and transmission electron microscopy and teaching me so much about analyzing obtained pictures.

Pascal's support and introduction in the lab and all the sample preparations. Arpit for staying with us for a few months, helping me investigating thermal conductivity in powder systems and showing so much enthusiasm in science. Kiki for his great support, in the lab over the last year. Especially, for conducting a lot of the experiments during my stay in Japan.

Anette Krappweis and Kirsten Kalischer for the support through my whole time here in this institute. Anette, thank you for putting so much effort in fighting for justice. To Marius and Edward, sharing the experience of writing a thesis in the

Acknowledgement

writing office. To all the people in the group, thanks for such a nice and friendly environment. Especially, I would like to thank all the people from the Hydrogen Storage group.

To Lana for all the love and support over the last years and especially during the time of writing. Thank you for making the last years so unforgettable. To my family, for the unconditional support throughout the study time in Duisburg and Mülheim. Domme and Sevi for one of the greatest inventions over the last years, the Bierumvirat and all the great time we shared, especially during the last four years. A big thanks goes to Freddy, without whom the stay and work in the Institute would not have been the same and for all the discussions and review talks, which were always interesting and entertaining. Alex B's for beer and bouldering.

Finally, I am grateful for the financial support by the International Max Planck Research School for Interface Controlled Materials for Energy Conversion (IMPRS-SurMat). A big thanks goes to Elke Gattermann for organizing the lectures, workshops and especially the annual retreats, which were not just interesting for broadening my own knowledge but real fun experiences with a lot of interesting people.

Abstract

In this work, the effective thermal conductivity measurements of magnesium-based metal hydrides for heat storage at high temperatures are discussed. To perform measurements under operating conditions measurement autoclaves have been developed which withstand temperatures up to 550 °C and hydrogen gas pressure up to 100 bar. Such an autoclave facilitates a Transient Plane Source (TPS) sensor in order to perform thermal conductivity measurements of the high-temperature metal hydrides. The challenge in developing the thermal conductivity measurement autoclave is the electrical connection from the sensor, embedded in a powder bed of highly reactive High Temperature Metal Hydride (HTMH) under high hydrogen gas pressure and high temperature to the *TPS 2500 S Hot Disk Thermal Constants Analyser* was successfully accomplished. Additionally, the investigation of the thermal conductivity of packed beds of magnesium particles under hydrogen pressure showed that the Effective Thermal Conductivity (ETC) of a particle bed of smaller particles are more susceptible to the change of the gas pressure than a the ETC of a particle bed of larger particles. Increasing the packing density increases the ETC, regardless the gas pressure. Investigated magnesium hydride was purchased and nickel activated magnesium hydride and magnesium iron hydride were thermally prepared by hydrogenation under gas pressure and temperatures above 350 °C. The measured ETC shows a dependency on the sample temperature and a strong dependency on the gas pressure, which is caused by the *Smoluchowski* effect. At temperatures above 300 °C the above mentioned metal hydrides dehydrogenate once the gas pressure is below the equilibrium pressure. The thermal conductivity strongly depends on the state of the metal hydride. In dehydrogenated state the ETC values are higher and more strongly dependent on the gas pressure, which is caused by the decreased particle size of dehydrogenated metal hydrides compared to the full hydrogenated metal hydrides. Running a hydrogenation and dehydrogenation cycle test of nickel activated magnesium hydride for more than 450 cycles shows a tremendous enhancement of the measured ETC. The maximum value for dehydrogenated nickel activated magnesium hydrides was found to be at above $8 \text{ W m}^{-1} \text{ K}^{-1}$ at 15 bar, 400 °C and after 201 cycles. Investigation by electron microscopy presents a percolated network of dehydrogenated magnesium hydride particles which were formed by coalescence and coarsening during the dehydrogenation steps and which are responsible for this enhanced thermal conductivity. Performing ETC measurements on magnesium iron hydride

showed that the thermal conductivity does not change with an increasing cycle number of de/-hydrogenation. The fact that the iron and magnesium are immiscible and do not form any alloys under these conditions are responsible for the absence of a formation of a percolated network. Therefore, no change of the ETC with increasing cycle number can be observed.

Kurzzusammenfassung

In dieser Arbeit wird die experimentelle Bestimmung der effektiven Wärmeleitfähigkeit von Metallhydriden auf Basis von Magnesium für die Anwendung im Bereich der Hochtemperatur-Energiespeicherung diskutiert. Spezielle Messautoklaven wurden für die Messungen der Wärmeleitfähigkeit entwickelt, welche Temperaturen von bis zu 550 °C und einem Wasserstoffdruck von bis zu 100 bar widerstehen. Die Messungen wurden mittels der sogenannten Transient Plane Source Method (TPS) bis unter den oben genannten Bedingungen durchgeführt. Während dieser Arbeit ist es gelungen diese Messautoklaven zu entwickeln. Die besondere Herausforderung hierbei war es, die elektrische Kontaktierung vom Sensor im Hochdruck und – Temperaturbereich des Autoklaven zum Analysemessgerät, dem TPS 2500S Thermal Constants Analyser, außerhalb des Druckbereiches und der Temperaturzone herzustellen. Im Laufe dieser Arbeit wurden Wärmeleitfähigkeitsmessungen an Magnesiumpulverschüttungen unter Wasserstoffdruck und Temperaturen bis zu 100 °C durchgeführt. Es konnte gezeigt werden, dass sich die Wärmeleitfähigkeit einer Pulverschüttung, bestehend aus kleineren Partikeln, stärker mit einer Gasdruckveränderung verändert, als die Wärmeleitfähigkeit in einer Schüttung aus größeren Partikeln. Die Erhöhung der Pulverschüttdichte, führt ebenfalls zu einer Erhöhung der Wärmeleitfähigkeit. In dieser Arbeit wurde käuflich erworbenes Magnesiumhydrid Pulver untersucht. Des Weiteren wurde Magnesiumeisenhydrid und Nickel aktiviertes Magnesiumhydrid in thermischen Verfahren bei Temperaturen über 350 °C und unter Wasserstoffdruck hergestellt und hinsichtlich der Wärmeleitfähigkeit untersucht. Ergebnisse zeigen, dass sich die Wärmeleitfähigkeit einer Pulverschüttung mit steigender Temperatur und steigendem Gasdruck erhöht. Der Einfluss des Gasdruckes ist stärker ausgeprägt, was sich durch den Smoluchowski Effekt erklären lässt. Bei den untersuchten Metallhydriden kommt es bei Temperaturen oberhalb von 300 °C und unterhalb des Gleichgewichtsdampfdruckes zu einer Dehydrierungsreaktion. Es hat sich gezeigt, dass dehydriertes Material eine stark erhöhte Wärmeleitfähigkeit aufweist. Die Gasdruckabhängigkeit ist in einer Pulverschüttung aus dehydriertem Magnesiumhydrid stärker ausgeprägt als in einer Pulverschüttung aus hydriertem Magnesiumhydrid. Dies hängt mit der kleineren Partikelgröße der dehydrierten Partikel gegenüber den größeren, hydrierten Partikeln zusammen. Ein Langzeitversuch zur Messung der Wärmeleitfähigkeit einer Pulverschüttung aus Nickel aktiviertem Magnesiumhydrid mit mehr als 450 De-/Hydrierzyklen hat gezeigt, dass sich die Wärmeleitfähigkeit mit steigender

Zyklenzahl stark erhöht. Im dehydrierten Zustand des Materials konnte ein Wert von $8 \text{ W m}^{-1} \text{ K}^{-1}$ bei einem Druck von 15 bar, einer Temperatur von $400 \text{ }^\circ\text{C}$ und nach 201 Zyklen gemessen werden. Der zum Teil starke Anstieg der Wärmeleitfähigkeit kann auf die Bildung eines perkolierten Netzwerkes zurückgeführt werden. Dieses hat sich aufgrund der wiederholten Dehydrier- und Hydrierreaktionen der Partikel gebildet. Bei der Untersuchung der Wärmeleitfähigkeit einer Magnesiumeisenhydrid Pulverschüttung hat sich keinerlei Veränderung eingestellt. Dieses Verhalten lässt sich auf das Ausbleiben der Legierungsbildung von Magnesium und Eisen zurückführen, welche die Bildung eines perkolierten Netzwerkes unterbindet.

Contents

Acknowledgement	ii
Abstract	iv
Kurzzusammenfassung	vi
1. Introduction	1
1.1. Motivation - Change in the Energy System	1
1.2. Objective	5
2. Fundamentals of Metal Hydrides	7
2.1. Magnesium hydride	14
2.1.1. Magnesium as hydrogen and heat storage medium	14
2.1.2. Synthesis of magnesium hydride	15
2.1.3. Kinetics	16
2.1.4. Catalytic activation by introduction of additives	17
2.1.5. Catalytic activation by downsizing	18
2.2. Magnesium iron hydride	19
2.2.1. Formation of magnesium iron hydride	19
3. Fundamentals of heat transfer in powder - gas systems	21
3.1. Heat transfer in non-reacting material	21
3.1.1. Thermal conductivity of gases	24
3.1.2. Contribution of the ideal gas in a packed bed to the thermal conductivity	25
3.1.3. Thermal conductivity of solids	27
3.1.4. Contribution of the solid particles in a packed bed to the thermal conductivity	28
3.1.5. Temperature and gas pressure dependency of the heat trans- fer mechanism	28
3.2. Heat transfer in high temperature metal hydrides under operating conditions	30

Contents

3.3. Methods to determine thermal conductivity	31
3.4. Literature survey	32
3.4.1. Modelling of thermal conductivity in porous media	32
3.4.2. Experimental work on thermal conductivity measurements of metal hydrides as heat storage material	34
4. Characterization Methods of Metal Hydrides	37
4.1. Thermal Conductivity measurement	37
4.1.1. Transient-Plane-Source-Method	37
4.1.2. Measurement procedure	41
4.2. Structural and morphological characterization	45
4.3. Chemical, compositional and thermo-gravimetical investigation . .	46
5. Autoclaves Development and Experiment Design	49
5.1. Safety aspects	51
5.2. Development of the 1. generation measurement autoclave	53
5.3. Development of the 2. generation measurement autoclave	55
5.4. Development of the 3. generation measurement autoclave	58
6. Results and Discussion	63
6.1. Synthesis of nickel activated MgH_2 and Mg_2FeH_6	64
6.1.1. Set-up and preparation of the synthesis	64
6.1.2. Equilibrium pressure curve for the formation of MgH_2 and Mg_2FeH_6	66
6.1.3. Calculation of hydrogen mass content in metal hydrides . . .	67
6.1.4. Synthesis of nickel activated MgH_2	68
6.1.5. Synthesis of Mg_2FeH_6	71
6.2. ETC measurement of magnesium powder	74
6.2.1. ETC as a function of the packed bed's packing density . . .	74
6.2.2. ETC as a function of the particle size	77
6.2.3. Model for the heat transfer in a packed bed	78
6.3. ETC measurement of Magnesium hydride	80
6.3.1. Measurement of the ETC at a temperature of up to $300^\circ C$.	81
6.3.2. Temperature coefficient of electrical resistivity (TCR) of the nickel sensor	83
6.3.3. Measurement of the ETC at a temperature above $300^\circ C$. .	85
6.3.4. The dependency of ETC on the cycle number	88

6.4.	ETC measurement of nickel activated magnesium hydride	91
6.4.1.	Measurements of nickel activate MgH_2 at temperatures of up to $300^\circ C$	91
6.4.2.	Measurement of nickel activated MgH_2 at temperatures above $300^\circ C$	92
6.5.	Comparison of the ETC of MgH_2 and nickel activated MgH_2	94
6.6.	Theoretical calculation of a cylindrical heat storage tank	96
6.7.	ETC measurement of magnesium iron hydride	99
6.8.	Long term experiments	100
6.8.1.	Nickel activated magnesium hydride	101
6.8.2.	Iron magnesium hydride	116
7.	Conclusion, final Remarks and Outlook	121
A.	Appendix	125
A.1.	Calculation of the ETC Mean Value	125
A.2.	Picture of MgH_2 (4 mass-% Ni) after ETC Measurements	127
A.3.	Equilibrium pressure data of MgH_2 and Mg_2FeH_6	128
A.4.	Measurement parameters	130
A.5.	Thickness and EDX data of Mica sensor	131
A.6.	Process feed through	132
A.7.	XRD data nickel activated magnesium hydride after long term test	133
A.8.	Mass, gravimetric and packing density of samples.	134
A.9.	Raw material cost of common metal hydride systems for high tem- perature heat storage	135
A.10.	Calculation of compressibility factor of hydrogen gas for operating conditions.	136
A.11.	ETC values of Hydrogen Gas	137
A.12.	Technical drawing of first-generation measurement autoclave.	138
A.13.	Estimation of residual oxygen after purging the test rig with hydrogen	138

List of Figures

2.1. Equilibrium vapor pressure curve of metal hydrides	8
2.2. Pressure Composition Isotherm (Pressure Composition Isotherms (PCI)) of ideal system (left) and the respective van't Hoff plot (right).	10
3.1. Heat transfer mechanism in powder - gas system [72,75].	22
3.2. Hertzian contact stress of particles caused by an external force F and thus an increased contact area between these particles.	30
4.1. Simplified circuit layout which connects the sensor for measuring the thermal conductivity with the TPS method.	38
4.2. Temperature increase of the sensor with the measurement time (left) and Temperature increase as function of the time function $D(\tau)$. (Values recorded to plot these graphs were recorded during the ETC measurement of dehydrogenated Magnesium Hydride (MgH_2) at 1 bar hydrogen and 400 °C.)	41
4.3. Profile of the sensor which is embedded in sample powder.	42
4.4. Temperature drift measurement with the sensor prior to the transient reading has started is presented in the left plot. The right graph shows a residual plot of the transient reading. It presents the temperature difference between measured and fitted data. The fitted data are determined during the calculation step (see Chapter 4.1.1). (Values recorded to plot these graphs were recorded during the ETC measurement of dehydrogenated MgH_2 at 1 bar hydrogen	44
5.1. Simplified flow sheet of test rig.	50
5.2. Safety box, which is located in the high-pressure lab of the Max-Planck-Institut für Kohlenforschung.	52
5.3. Measurement autoclave of 1 st Generation.	53

List of Figures

5.4.	Removable measurement cell of the 1 st generation measurement autoclave with main parts: the TP's sensor, the thermocouple for temperature control, the heating plate and the cap, including gas inlet and sinter matrix.	54
5.5.	Picture of measurement autoclave (2nd Generation) (top) and technical sketch (bottom). The main parts are the flanges a) and f), the high body of the pressure autoclave c), the inlet for the sample b), the sensor e) and its metallic holder.	56
5.6.	2 nd Generation measurement autoclave, placed in the infra-red furnace.	58
5.7.	Technical sketch of 3 rd Generation measurement autoclave. The main parts are the flanges a) and e), the body of the high pressure autoclave b), the sensor d) and its holder c).	59
5.8.	Schematic sketch of the measurement autoclave of the 2 nd and 3 rd generation.	60
5.9.	Illustration of metal hydride particle distribution around the sensor (b) in the 2 nd Generation measurement autoclave (left) and 3 rd Generation measurement autoclave. Horizontal positioning (in the left) of the sensor can cause densified areas above the sensor (a) and less dense areas below the sensor (c).	61
5.10.	3 rd Generation measurement autoclave in IR-heater furnace.	61
6.1.	Test rig for the synthesis of the magnesium-based metal hydrides, in this work.	65
6.2.	Equilibrium pressure curve of MgH ₂ (red curve) and Magnesium Iron Hydride (Mg ₂ FeH ₂) (black curve).	67
6.3.	Hydrogen pressure of nickel activated magnesium hydride during the synthesis via 51 cycles of de-/hydrogenation (left) and the calculated hydrogen mass fraction in the nickel activated magnesium hydride as a function of the cycle number in (right).	69
6.4.	Thermogravimetric analysis (left) and X-Ray pattern (right) of synthesized nickel activated magnesium hydride.	71
6.5.	Magnesium iron hydride as synthesized from the autoclave (left) and the filled measurement cell 3 rd Generation (right).	73
6.6.	Thermogravimetric analysis (left) and XRD pattern (right) of magnesium iron hydride.	73

6.7. Effective thermal conductivity of magnesium powder of mesh 50 with different packing densities, different gas pressure and at two different temperatures.	75
6.8. Effective thermal conductivity of magnesium powder of different particle sizes with a packing density of 41 % at 100 °C. For comparison, the thermal conductivity values of hydrogen are presented by the purple marks.	77
6.9. Schematic drawing of the contact area between two spherical particles. The main heat conduction paths are the heat conduction via the contact area of the two involved particles Q_S , the heat conduction through the gas in large voids Q_g and a gas pressure-sensitive region between the particles Q_{Kn} . On the left bottom, the calculated reduced thermal conductivity of hydrogen gas is presented as a function of the distance D between two solid surfaces, at 25 °C and different gas pressures. On the right bottom the reduced thermal conductivity of hydrogen gas in a void of 100 nm distance as a function of the gas pressure.	79
6.10. Thermogravimetric analysis of MgH_2 prior ETC measurements, showing the characteristic mass loss above 400 °C (left). X-ray pattern of the same material, which shows reflexes for MgH_2 , Mg and $Mg(OH)_2$ (right).	81
6.11. Effective thermal conductivity of magnesium hydride under hydrogen gas pressure at sample temperatures between 25 °C and 300 °C.	82
6.12. The left graph presents the electrical resistance of the nickel sensor, plotted as the function of the temperature, which was recorded as the sensor was embedded in the magnesium hydride powder bed. The right graph shows the TCR of nickel as function of the temperature. The black dots are the literature values, given by <i>Hot Disk AB</i> and the red.	84
6.13. Effective thermal conductivity of magnesium hydride under 25 bar hydrogen determined with the TCR values from literature (black dots) and the newly determined values (red dots), in the temperature range of 300 °C to 400 °C.	85
6.14. Effective thermal conductivity of magnesium hydride under operating conditions.	86

List of Figures

6.15. Effective thermal conductivity of magnesium hydride at 390 °C and 410 °C as a function of the applied hydrogen pressure at different charging/discharging cycle numbers.	88
6.16. Thermogravimetric analysis of MgH ₂ after ETC measurements, showing the characteristic mass loss above 400 °C (left). X-ray pattern of the same material, which shows reflexes for MgH ₂ , Mg, and MgO (right).	90
6.17. ETC measurement of nickel activated magnesium hydride as a function of hydrogen gas pressure at temperatures up to 300 °C.	92
6.18. Effective thermal conductivity of nickel activated magnesium hydride under operating temperatures as a function of the applied gas pressure	93
6.19. Schematic draft of cross-section view on 2-D model for the theoretical calculation to estimate the influence of the ETC values of the metal hydride to the heat resistance.	96
6.20. Heat resistivity of the contributing sources for resistance with an assumed ETC in the magnesium hydride bed of 1 W m ⁻¹ K ⁻¹ (left) and the comparison of the overall heat resistivity between different ETC values of the metal hydride (right), as a function of the reactor diameter.	98
6.21. Effective thermal conductivity of Mg ₂ FeH ₂ powder under a hydrogen gas atmosphere.	100
6.22. Effective thermal conductivity of nickel activated magnesium hydride at 400 °C at 1, 15 and 25 bar hydrogen and as a function of the cycle number in the measurement cell.	103
6.23. Hydrogen content in the nickel activated magnesium hydride, during the synthesis and the cycling experiment, estimated from the difference between the dehydrogenation pressure and the hydrogenation pressure.	104
6.24. Nickel activated magnesium hydride after 51 cycles of de-/hydrogenation (left), and nickel activated magnesium hydride after 510 cycles of de-/hydrogenation in the measurement autoclave (right).	105

6.25.	The left picture shows nickel activated magnesium hydride, which was synthesized by 51 cycles of de-/hydrogenation and placed in the measurement cell for the ETC long term experiment. In the right picture, the nickel activated magnesium hydride can be seen, which experienced additionally 459 cycles of de-/hydrogenation in the measurement autoclave during the long term experiment.	106
6.26.	SEM overview (magnification: 1000) of nickel activated magnesium hydride with EDX mapping after 510 cycles.	107
6.27.	SEM overview (magnification: 1000) of nickel activated magnesium hydride in the dehydrogenated state with EDX mapping after 510 cycles.	108
6.28.	The influence of the heating power and the time which was removed from the beginning of the transient reading before the calculation of the effective thermal conductivity of MgH_2 after 502 hydrogenations, measured at 20 bar hydrogen pressure and 400°C , was performed.	113
6.29.	The influence of the heating power and the time which was removed from the beginning of the transient reading before the calculation of the effective thermal conductivity of dehydrogenated MgH_2 after 502 hydrogenations, measured at 1 bar hydrogen pressure and 400°C , was performed.	114
6.30.	Profile of TPS sensor in a powder bed with a gradient of the packing density, indicating different times t of the transient reading, which were considered for the evaluation (bottom). On the top, the schematic temperature increase of sensor as a function of measurement time with different time ranges for evaluation.	115
6.31.	ETC measurement of magnesium iron hydride powder bed as a function of the de-/hydrogenation cycles. The measurements were taken at a hydrogen pressure of 70 bar and at temperatures of 480°C (hydrogenated) and 520°C (dehydrogenated).	118
A.1.	MgH_2 (4 mass – % Ni) after 462 cycles of de-/hydrogenation during removing it from the measurement autoclave.	127
A.2.	Process feedthrough for connecting the sensor.	132
A.3.	XRD pattern of nickel activated magnesium hydride after long term test (510 cycles).	133
A.4.	ETC of hydrogen gas, plotted with data from [85]	137

List of Figures

A.5. Technical sketch of first-generation measurement autoclave. 138

List of Tables

1.1. Advantages and disadvantages of the mentioned heat storage principles.	2
1.2. Examples of different materials for heat storage applications [10,11]	3
2.1. List of metals that are forming metal hydrides (A) and metals which do not form metal hydrides (B).	8
2.2. Examples of different types of metal hydride forming alloys and intermetallic compounds.	9
2.3. Overview of high-temperature metal hydrides with key properties: the theoretical hydrogen mass ω_{H_2} , the working temperature Θ_{work} with the respective equilibrium pressure p_{eq} , the dehydrogenation enthalpy ΔH_{Des} and the thermal energy density ρ_{Th} [20]. For comparison the low temperature metal hydride $\text{TiMn}_{1.5}\text{H}_{2.5}$ was added to this table.	14
2.4. Hydrogen content and energy densities for magnesium hydride and magnesium iron hydride [10,69].	20
3.1. Flow regimes and respective Knudsen numbers [78].	26
3.2. Temperature and pressure dependency of the thermal conductivity of single heat transfer paths.	29
3.3. Thermal conductivity values of contributing phases of magnesium/magnesium hydride powder bed (Calculated for hydrogen [85].	29
4.1. Types of insulating material of the TPS sensor with operating temperature range and remarks for application.	38
4.2. Elements in sheet silicate (Mica) insulation layer of the TPS sensor.	41
5.1. Nickel and maximal operating temperature of used high temperature steel.	56

List of Tables

6.1. Overview of metal hydride samples of which the effective thermal conductivity was measured in this work.	64
6.2. One cycle of the temperature-controlled program for the synthesis of the nickel activated magnesium hydride.	69
6.3. One cycle of the temperature-controlled program for the synthesis of the magnesium iron hydride	72
6.4. Magnesium powder for ETC measurement investigation.	74
6.5. ETC values of MgH_2 and MgH_2 (4 mass – %Ni) as a function of the de-/hydrogenation cycles.	95
6.6. Temperature, step time and/or temperature rate for the de-/hydrogenation experiment of Mg_2FeH_2	97
6.7. Process steps of one de-/hydrogenation cycle for the long term cycle test of magnesium hydride.	102
6.8. Composition of the nickel activated magnesium hydride sample, determined by Rietveld analysis.	110
6.9. Temperature, step time and/or temperature rate for the de-/hydrogenation experiment of Mg_2FeH_2	117
A.1. Mean value, mean absolute deviation and relative mean deviation of ETC values of MgH_2 (4 mass – % Ni), calculated using different amounts of data points.	126
A.2. Equilibrium pressure of MgH_2 and Mg_2FeH_2	129
A.3. Parameters for the measurement of the ETC of Mg, MgH_2 , MgH_2 (4 mass – % Ni) and Mg_2FeH_2 in this work. Each reading was performed at least three times and the waiting time between each reading was set to 3 to 10 minutes.	130
A.4. Elemental analysis of TPS sensor cover material (Mica) before and after 461 cycles of de-/hydrogenation of nickel activated magnesium hydride.	131
A.5. Sample mass, volume of respective measurement cells, gravimetric density and packing density of the samples.	134
A.6. Elemental distribution of the magnesium iron hydride sample for calculating the packing density. Measurement cell has a volume of 44.37 cm^3 . The packing density was calculated to be approximately 11%.	134

A.7. List of raw material presents the cost of high-temperature metal hydrides. Two low-temperature metal hydrides (LTMH) for hydrogen storage are added for comparison reasons [20].	135
A.8. Coefficients for calculating the real gas factor of the hydrogen under operating conditions of the heat storage application [24].	136
A.9. Estimation of the amount of oxygen in the test rig during the purging process (Chapter 5).	138

List of Abbreviations

CSP	Concentrated Solar Thermal Power Plants
DOE	U.S. Department Of Energy
EDX	Energy-Dispersive X-Ray Spectroscopy
ETC	Effective Thermal Conductivity
HPT	High Pressure Torsion
HTF	High Temperature Fluid
HTMH	High Temperature Metal Hydride
KNO₃	Potassium Nitrate
MeH	Metal Hydride
Mg₂FeH₂	Magnesium Iron Hydride
MgH₂	Magnesium Hydride
NaCl	Sodium Chloride
PCI	Pressure Composition Isotherms
SEM	Scanning Electron Spectroscopy
TES	Thermochemical Energy Storage
TGA	Thermogravimetric Analysis
TPS	Transient Plane Source
XRD	X-Ray Diffraction

1. Introduction

1.1. Motivation - Change in the Energy System

Since the late 20th century the exploration of alternative and renewable energy technologies has become one of the top priorities among researchers in the science community. This is caused due to the fact that the human population faces serious issues as heatwaves, droughts, storms, floods, and a decreased biodiversity which itself causes endangerment of food and drinking water safety, health issues, increased chances for conflicts and war and disaster-induced migrations. That these issues are caused by an anthropogenic climate change are undeniable [1].

On the search to new sources to provide electrical and heat energy to the society the main goal is the reduction of emitted greenhouse gases and carbon dioxide which were confirmed to be the driving force number one for the expected temperature rise of 2–4 °C in the time period of 1990 to 2100 [2].

To stop or at least to reduce the anthropogenic temperature increase and the related global warming with its effects to the environment, the nature and to all living species electric energy must be generated from non-fossil fuels based sources. Most prominent examples are wind, solar, water, and geothermal energy sources [3].

The transition in the energy system is based on three columns: electrical energy generation, energy distribution, and energy storage. Whereas the public discussions and research activities were mainly focused on the generation of electricity by the usage of renewable energy sources the topics of energy distribution and storage were mostly neglected [4]. The energy transition towards non-fossil-fuel-based energy systems is just possible if the electricity provision is stable and fluctuations are covered by electricity, which was generated by carbon-free techniques. Therefore two main challenges among the development of renewable energy power plants are to face: the grid expansion, to deliver the ‘green’ electricity to the consumer and the energy storage, to decouple the energy supply from the energy demand [5,6].

1. Introduction

As mentioned a key issue for the transition to energy system based fully on renewable energy sources is energy storage.

The generation of electricity which is based on wind and solar is volatile because it strongly depends on weather conditions. This results in an unstable and fluctuating provision of electrical energy to the power grid [7]. Storing energy is supporting the operation of a stable power grid and is additionally compensating the high energy load during periods in which the electricity generation by solar and wind is not sufficient enough to cover the demand [8].

There are plenty of approaches for storing energy, as in form of mechanical energy (e.g. pumped-hydropower), energy storage in organic fuels (e.g. biomass), electromagnetic energy storage (e.g. capacitors), electrochemical energy storage (e.g. batteries) and heat energy [9].

Since this work discusses heat storage systems, which is based on magnesium hydride, this chapter provides more information about storing energy in the form of heat. The so-called heat storage can be divided into sensible heat, latent heat, and thermochemical heat. The advantages and disadvantages of each approach are presented in Table 1.1.

Storing energy in form of sensible heat Q as in water, rocks, concrete or salts depends on the mass m of the storing material the specific heat capacity c and the temperature difference ΔT between the heat sink and source [10].

$$Q = m \cdot c \cdot \Delta T \quad (1.1)$$

The advantages of this method are the rather simple installation of the heat storage system and the low operating cost. Disadvantages are the relatively low stored energy density and a required thermal insulation. Furthermore is the energy which is released at a decreasing temperature level. An example for sensible heat storage

Table 1.1.: Advantages and disadvantages of the mentioned heat storage principles.

Heat storage	Sensible heat	Latent heat	Thermochemical heat
Capacity	Weak	Weak	Large
Insulation	required	required	Not required
Working temperatures	Low to high	Low to high	High
Technology	Simple	Simple	Complex

1.1. Motivation - Change in the Energy System

medium can be found in Table 1.2.

The second approach of heat storage is the latent heat thermal energy storage which involves a phase change of the storing material caused by heating. In most cases, the material undergoes a phase change from solid to liquid or liquid to gas. The material is heated thus the temperature increases proportional to the energy which is received until it reaches the melting or vaporization temperature. At this temperature a further energy input is used to perform the phase change of the material, which is called latent heat [12]. Researchers have discussed many different material classes for phase change materials of which a few could be used for high temperature heat storage as e.g. nitrate salts [13,14].

An advantage of this heat storage technique is the constant temperature at which the energy is stored and released. A major drawback of phase change materials for heat storage is the differences between the thermophysical properties of the material in solid and liquid state, as the volume expansion due to the melting of the salt, low heat transfer capability, low energy efficiency and the need of homogeneous temperature distribution in large salt reservoirs [14].

These two above mentioned methods to store heat have two main drawbacks which make the up-scaled application more challenging. The heated material has to be well insulated, especially in case of the sensible heat storage with molten salts, which reach temperatures of up to 900 °C [13].

The most promising to approach for efficient thermal energy storage is the method of thermochemical heat storage. The working principle of this method is based on a

Table 1.2.: Examples of different materials for heat storage applications [10,11]

Material	Gravimetric energy den- sity in kW h kg ⁻¹	Volumetric energy den- sity in kWhm ⁻³	Temperature change ΔT in K	Temperature in °C
Water	0.093	93	80	$T < 100$
NaCl (solid)	0.0708	153	300	$T_{\text{hot}} = 500$
KNO ₃	0.0738	156		$T_{\text{melt}} = 333$
Mg+H ₂ ⇌MgH ₂	0.78	1110		$T_{\text{range}}=350-450$
MgH ₂				

1. Introduction

heat-driven reversible reaction in which in most cases heat is applied to decompose at least a binary material in its components. This is the endothermic reaction in which energy is stored in form of the reaction enthalpy. If energy is needed the reverse reaction provides heat from the reaction enthalpy of the formation of the starting material [10, 15]. Storing energy over a long period (seasonal) by a thermochemical reaction does not require thermal insulation as for sensible or latent heat storage systems. Additionally, the volumetric and gravimetric energy density is a magnitude of order larger in thermochemical heat storage materials, which reduces the amount of storing material and thus the cost of investment, as presented in Table 1.2 [10].

One material class which might meet the goals for heat storage materials are the metal hydrides. The so-called high temperature metal hydrides are working at temperatures above 300 °C [16] and therefore at higher temperatures than most of the molten salts which are used as latent heat storage materials [13].



Most promising examples for energy storage systems, which are based on metal hydrides, could be found in Concentrated Solar Thermal Power Plants (CSP). By adding a storage technology to these power plants a continuous energy provision could be enabled [14, 17–20].

Thermochemical Energy Storage (TES) systems in Germany could be applied at manufacturing system of high temperature industries as the glass blower, chemistry and steel producing industry in which waste heat can be stored [21].

Another big market for this type of energy storing technology is the power to heat approach in which excess power from renewable energy sources as wind power could be used to be stored in times of low demand [21, 22].

To enable a cost-efficient metal hydride based TES system the starting material should be prepared via a simple method and be non-harmful. Therefore a promising approach is to use inexpensive metal powder as magnesium particles or shavings. These can easily be moved into a heat storage vessel thus the installation is considerably manageable and safe. A major drawback is the expected rather low heat transfer capability of powder beds [19, 23]. This is caused by a low thermal conductivity of these beds, which has to be investigated and understood in order to improve the material, design the storage tank and define the operating conditions [17].

1.2. Objective

The low heat transfer in powder beds is one of the key issues, which restricts and slows down the development of heat storage systems, which are based on metal hydrides. Especially in high-temperature heat storage systems, in which the energy is stored at a high density (e.g. Mg_2FeH_2 : $1513 \text{ kWh}_{\text{th}}\text{m}^{-3}$), an in-depth understanding of the heat transfer is required to design, construct and efficiently run the energy storage system. To gain knowledge about the thermophysical properties of the metal hydride beds, the thermal conductivity must be determined, especially under working conditions of a hydrogen pressure of up to 100 bar and a temperature of up to 500°C . Therefore, a method is applied to investigate the thermal conductivity of high-temperature metal hydride powder beds. In this work the TPS method is used because it is applicable under the above-mentioned conditions. The material which are investigated is MgH_2 , nickel catalyzed magnesium hydride and Mg_2FeH_2 . The MgH_2 serves as a model system to test the measurement procedure. The second material is considered to be used for a pilot heat storage tank system of 400 kg material, which is planned to be developed in the next years in cooperation of the *Max-Planck-Institut für Kohlenforschung*, the *Westfälische Hochschule (WHS)*, the *Institut für Energie und Umwelttechnik (IUTA)* and industrial partners. The third material is operating at higher temperatures and is one of the most promising materials for the application at temperatures above 500°C .

This work focuses on following objectives:

- The design and development of measurement set-ups to facilitate thermal conductivity measurements of high-temperature metal hydrides under operating conditions. This means, high-pressure autoclaves have been developed, which withstand a hydrogen pressure of up to 100 bar, at a temperature of up to 550°C , in order to facilitate ETC measurements.
- Designing of a thermal conductivity measurement procedure in order to ensure reliable results, which is especially of great importance at elevated temperatures and gas pressure, at which the investigated metal hydride can be dehydrogenated or hydrogenated.
- Measuring the effective thermal conductivity of magnesium particles, to investigate the influence of temperature, hydrogen gas pressure, and particle size on the thermal conductivity in a packed bed.
- Development of set-up for the synthesis of nickel catalyzed magnesium hy-

1. Introduction

drude and magnesium iron hydride and their preparation in order to execute a subsequent thermal conductivity measurement on these hydrides.

- Investigation of the effective thermal conductivity of magnesium hydride, nickel catalyzed magnesium hydride and magnesium iron hydride powder beds under operating conditions ($T < 550\text{ }^{\circ}\text{C}$, $p(\text{H}_2) < 100\text{ bar}$). The ETC readings are investigated with respect to their state, if hydrogenated or dehydrogenated. Measurement during the hydrogenation process is executed to emphasize the strong dependency of the hydride formation to the heat transfer capability.
- Cycle experiments are performed to investigate the stability of nickel catalyzed magnesium hydride and magnesium iron hydride regarding their hydrogen thermal conductivity, morphology and hydrogen capacity. Thus nickel catalyzed magnesium hydride is exposed to 500 cycles of hydrogenation and dehydrogenation.

2. Fundamentals of Metal Hydrides

This chapter provides information about the fundamentals of metal hydrides for high-temperature heat storage applications. Many metals, metal alloys, and intermetallic compounds can react with hydrogen to metal hydrides. For many metals this reaction is reversible, thus the resultant metal hydrides can decompose again to the starting material and hydrogen gas. The equilibrium state of a metal hydride is defined by an equilibrium pressure curve, which is defined individually for each metal hydride by temperature and hydrogen gas pressure (Figure 2.1).

If the gas pressure and/or temperature of the metal hydride/gas system is not on the equilibrium pressure curve the Metal Hydride (MeH) is either decomposed into its components (dehydrogenation) or the MeH is formed (hydrogenation). During the hydrogenation the heat ΔH_R is released (heat recovery) in an exothermic reaction (Equation 2.1). This reaction can be initiated by decreasing the temperature or increasing the pressure and is presented in Equation 2.1.



To start the endothermic dehydrogenation the pressure can be decreased and/or the temperature increased.

Metals with low electron negativity react with hydrogen into stable metal hydrides which can be decomposed under high temperatures and/or low hydrogen gas pressures. These metals are called A–metals, while most of the electron negative transition metals do not form metal hydrides under technical relevant parameters (B–metals) [24]. Examples are presented in Table 2.1.

By mixing A and B metals, hydride forming intermetallic compounds or alloys can be synthesized, that react at temperatures above 350 °C and gas pressures¹ which

¹A high hydrogen pressure increases the costs of invest and maintenance since it is more difficult to achieve hydrogen impermeability in the MeH pressure vessels especially at elevated temperatures. The necessary hydrogen volume will be reduced, if the pressure is higher, which reduces the material costs for the hydrogen tanks during the time of heat storage.

2. Fundamentals of Metal Hydrides

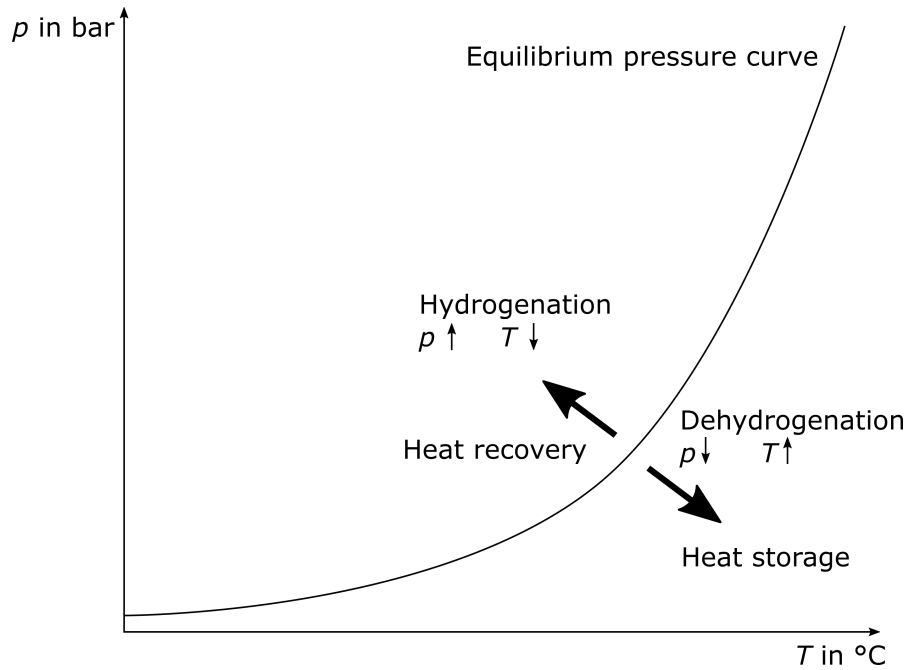


Figure 2.1.: Equilibrium vapor pressure curve of metal hydrides

Table 2.1.: List of metals that are forming metal hydrides (A) and metals which do not form metal hydrides (B).

Elements	
A (hydride forming)	B, Li, Na, K, Cs, Mg, Ca, La, Ti and Zr
B (not hydride forming)	Cu, Ni, Co, Fe, Mn, Cr and Mo

are relevant for heat storage application [10, 16, 20]. Examples for gas pressures and temperatures can be found in Table 2.3. Typically, the metal-hydride-forming compounds can be assigned to the composition: A_2B , AB , AB_2 , and AB_5 . Some examples for metal hydrides can be found in the following table 2.2.

Another type of metal hydrides is called complex metal hydrides, $M_m^{\delta+} [TH_n]^{\delta-}$. This type of hydrides consists of M_m , which is alkaline, alkaline earth or divalent rare-earth metal, and a metal-hydrogen complex $[TH_n]^{\delta-}$, with n hydrogen atoms. An example of complex metal hydrides is Mg_2FeH_2 , in which $[FeH_6]^{\delta-}$ is the metal-hydrogen complex [26].

The formation of metal hydrides from metals and hydrogen gas starts with the dissociation of hydrogen molecules on the surface of the solid metal particles. The hydrogen atoms diffuse into the material and are occupying the interstitial sites in the metal crystal. In this so-called α -phase, the hydrogen atoms are statistically distributed to form a solid solution. If the hydrogen pressure is further increased,

Table 2.2.: Examples of different types of metal hydride forming alloys and intermetallic compounds.

	Example
A	MgH ₂
A ₂ B	Mg ₂ NiH ₄
AB	TiFeH ₁ or TiFeH ₂ [25]
AB ₂	ZrMn ₂ H ₂
AB ₅	LaNi ₅

the concentration of H atoms within the α -phase enhances thus the hydrogen-hydrogen interaction becomes so strong that a new hydrogen-rich phase, the metal hydride phase (β -phase) starts to nucleate and to grow. The supply of more hydrogen gas at this point does not result in an increasing gas pressure, moreover the α and β -phases are growing and a pressure plateau (Figure 2.2) will be formed. This can be explained with the Gibbs phase rule [24],

$$F = N - p + 2 \quad (2.2)$$

in which F is the degree of freedom, N the number of chemical species and p the number of phases. Three phases, the α -phase, the β -phase, and the gas phase are coexisting ($p = 3$). In a binary system, they are two chemical species ($N = 2$) which results in one degree of freedom ($F = 1$) (Equation 2.2). If the temperature is fixed (isothermal conditions), the supply of more hydrogen gas will cause the conversion of the α -phase to the β -phase. After reaching the full formation of the hydride phase, the degrees of freedom increase to two, which is caused by the fact that there are two phases (instead of three) prominent in the system. A further gas supply causes an enhancement of the pressure.

The formation of a metal hydride under hydrogen gas pressure can be explained with the PCI. The PCI of a hydrogen-metal system shows the hydrogen equilibrium pressure as the function of the amount of hydrogen, which is absorbed in the metal², at a fixed temperature. The PCI of an ideal system is presented in Figure 2.2. The length of the pressure plateau gives a hint concerning the reversible hydrogen storage capacity and therefore to the energy storage capacity³.

²The hydrogen content is usually expressed as the ratio of the mass of the hydrogen to mass of the metal (mass - %).

³The energy storage capacity is related to the hydrogen storage capacity, because the reac-

2. Fundamentals of Metal Hydrides

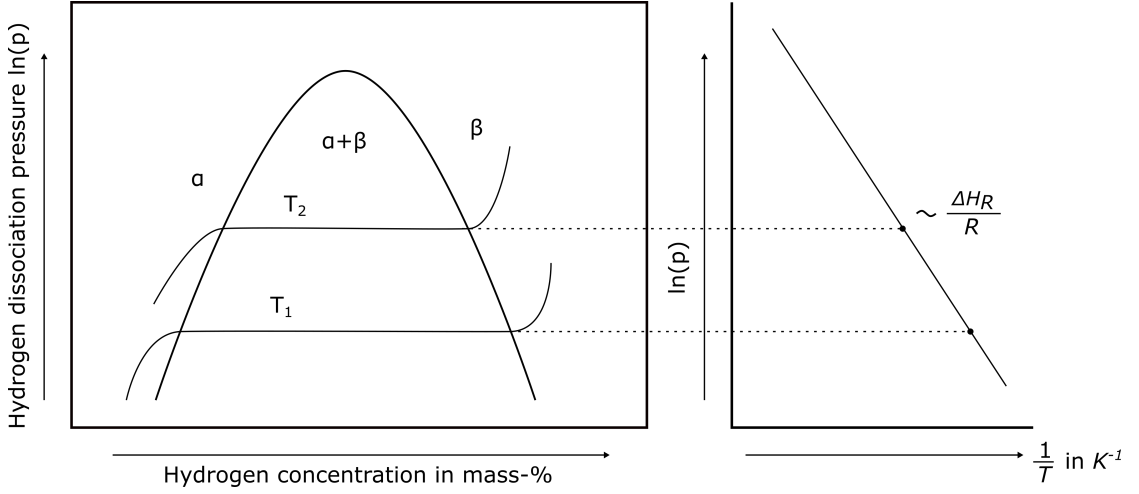


Figure 2.2.: Pressure Composition Isotherm (PCI) of ideal system (left) and the respective van't Hoff plot (right).

The stability of an MeH can be determined by the location of the pressure plateau. Less stable metal hydrides require a lower temperature to reach a certain plateau pressure than more stable. At elevated temperatures the length of this pressure plateau decreases until it vanishes at the critical temperature. In an ideal case the absorption and desorption (PCI) are identical. Every state in the PCI in Figure 2.2 is in equilibrium and can be mathematically described by the van't Hoff equation [27]:

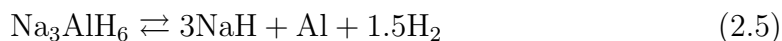
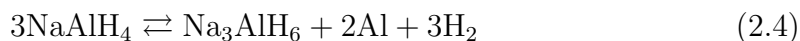
$$\ln(p) = \frac{\Delta S_R}{R} - \frac{\Delta H_R}{RT} \quad (2.3)$$

in which ΔS_R is describing the molar entropy change, ΔH_R the molar reaction enthalpy, R the universal gas constant, and T the absolute temperature. The constructed van't Hoff plot is depicted in the right graph in Figure 2.2. The enthalpy of formation ΔH_R divided by R equals the slope of this plot. The intercept ($1/T = 0$) of this plot equals the entropy of formation ΔS_R divided by R . The entropy change corresponds mainly to H_2 which is changing from molecular hydrogen to dissolved solid hydrogen. Therefore the standard entropy of hydrogen is the same as the entropy of formation, which is approximately $\Delta S_R \approx -130 \text{ J K}^{-1} \text{ mol}^{-1}$ for all metal–hydrogen systems [28].

In a realistic, non-ideal thermodynamic system one will find pressure plateaus with a slope or more than one plateau. A reason for slopes can be found in

tion enthalpy determines the energy storage capability and is indicated per mol hydrogen (Equation 2.1).

the formation of slightly different hydrides, which have slightly different pressure plateaus. These plateaus then sum up to one plateau with a slope. Experiments have shown that the slope of the PCI is mostly a result of an inhomogeneous material distribution, which itself is caused by the preparation of the sample. The slope is usually steeper in complex and multi-component metal hydride systems than in carefully synthesized binary intermetallic compounds [24]. Metal hydrides which react and decompose in more than one step show multiple pressure plateaus in a PCI-plot [27]. A prominent example is the decomposition of the complex transition metal hydride sodium alanate (NaAlH_4) [29].



Another feature of a realistic PCI can be found in an increased plateau pressure during the hydrogen absorption than during the dehydrogenation. This phenomenon results in hysteresis in the PCI-plot. Even though this behavior is studied since 1937 [30], it is still not completely explained in the literature. In general, it can be assumed that the hysteresis is caused by mechanical stress and plastic deformation during the transformation of the α -phase to the β -phase during the hydrogenation which is accompanied by a volume change. (The volume change during the hydrogenation of magnesium is up to 30 % [24]. The volume increase is introduced by a change of lattice distances and thus an increased unit cell volume.

Classification

For technical consideration, metal hydrides for heat storage applications can be distinguished by their operating temperature. This classification is important in order to choose the right metal hydride, which operates at the temperature of the heat source, in the application. Additionally, the temperature at which the heat is stored and subsequently released during the time of demand is important for the efficiency during the heat to power conversion in a heat engine. This efficiency is limited by the Carnot theorem and depends on the temperature difference between the high-temperature heat source and the heat sink. The high temperature on the hot site and thus a possible high temperature difference is beneficial for high conversion efficiency. In general, these hydrides can be divided into low-, medium-

2. Fundamentals of Metal Hydrides

and high-temperature metal hydrides [20].

Low-temperature metal hydrides can be formed at temperatures up to 100 °C. They are interesting for stationary hydrogen and heat storage systems in households [31]. There are hundreds of suitable alloys which form metal hydrides. Examples are LaNi_5 and FeTi which benefit from fast kinetics [20].

For medium and high-temperature metal hydrides different definitions, concerning the operating temperature, can be found in the literature. Buchner et al [16] defined high-temperature metal hydrides to operate at temperatures above 200 °C. More recent publications define high-temperature metal hydrides to operate at a temperature above 500 °C [20]. Increasing the temperature at which the heat is stored favors a later heat-to-power efficiency. Metal hydrides, which are working under elevated temperatures, are interesting especially for concentrated solar thermal power plants (CSP), as parabolic troughs, solar power towers, Fresnel reflectors or parabolic dish systems [32]. Another interesting application for high-temperature metal hydrides can be found in storing waste heat from industrial factories and manufactures like steel and chemical industry. In biomass power plants, cogenerated heat can be stored in metal hydrides. This stored heat can be used to ensure a continuous and on-demand power supply and district heating [33,34]. Because magnesium hydride has an operating temperature of approximately 350 °C to 450 °C, it can count as medium or high-temperature metal hydride, depending on definition. Whereas, magnesium iron hydride, with a maximum operating temperature of 550 °C, is per both definitions a high-temperature metal hydride. Both hydrides are well-investigated materials that were subject to research for the last 70 years [23]. Other materials as calcium hydride (CaH_2), titanium hydride ($\text{TiH}_{0.5-1.7}$) and sodium magnesium fluoride (NaMgH_2F) are under recent investigation and achieve even higher operating temperatures of approximately 1000 °C [19].

In the following, important properties of metal hydrides for heat storage applications will be listed. The targets were defined in the SunShot initiative, which was launched by the U.S. Department Of Energy (DOE) in 2011 [35].

- The DOE target for the volumetric energy density was set to $25 \text{ kWh}_{\text{th}}\text{m}^{-3}$, in order to reduce the size of the heat storage systems and the cost of the materials. Common high-temperature metal hydrides meet and exceed this target e.g. MgH_2 achieves a volumetric energy density of above $600 \text{ kWh}_{\text{th}}\text{m}^{-3}$ [36].
- Metal hydrides must be non-toxic to allow a safe construction and operating

of large thermal energy storage plants based on metal hydrides. Additionally, the impact on the environment and nature, where the heat storage system is located, has to be minimized to raise the acceptability to the public.

- The material for heat storage systems should be inexpensive to meet the SunShot targets for metal hydride-based heat storage systems for CSP applications. This target was set to an overall cost of 15 \$/kWh_{th}, which includes the costs of the MEH, the storage tank, the heat transfer system, and the pressure vessel. In the case of MgH₂ and Mg₂FeH₂, the cost of the MEH was calculated to be 40 % of the overall costs [36, 37].
- Lifetime and cycle stability are crucial factors for running industrial energy storage systems. The storage capacity and the conversion kinetics should be in a reasonable limit to meet the requested energy demand by the consumer.
- The working temperature should be as high as possible in order to have high energy conversion efficiency during the generation of electricity from the stored heat. The SunShot target defines a lower high-temperature limit of 500 °C [37]. The exergetic efficiency was calculated to be in the order of 70 % – 75 % at an operating temperature of 500 °C and at about 95 % at temperatures above 1000 °C [36].
- During the period of heat storage, the released hydrogen gas has to be stored. Storing hydrogen, in large amounts, is a cost-intensive part of storing heat with metal hydrides. Calculations in [38] reveal that more than 66 % of the installation cost (including heat exchanger) of MgH₂ heat storage system, which can run a 200 MW turbine for 7 hours, comes from the hydrogen storage material⁴. Therefore, it is favorable to have a low hydrogen capacity, in combination with a high reaction enthalpy to reduce these costs.
- A crucial point for developing, constructing and operating large scale heat storage systems (> 1000 MW h) for power plants is the heat transfer in and out of the storage material. Since the storing material is composed of metal hydride powder beds⁵, which suffer from low heat transfer capabilities the thermal conductivity of such a bed is an important factor, which absolutely has to be considered. Therefore, it is inevitable to gain a better understanding of the thermal conductivity in metal hydride powder beds. This work will

⁴In this calculation the hydrogen is stored in Ti_{1.2}Mn_{1.8}H_{3.0}, which acts as low temperature metal hydride storage.

⁵To keep the preparation cost of the metal hydrides low thus to meet the SunShot target, the material must be in powder form.

2. Fundamentals of Metal Hydrides

provide some insights into the heat transfer capability of magnesium-based hydrides with the help of thermal conductivity measurements under operating temperatures (up to 520 °C and hydrogen gas pressure up to 100 bar, for magnesium iron hydride).

These are some of the most important properties, which must be considered while choosing the right metal hydride for energy storage systems. A few examples of promising HTMH for metal hydride-based heat storage systems are presented in 2.3, including some important thermodynamic properties. For comparison, a low-temperature metal hydride is added to this table.

Table 2.3.: Overview of high-temperature metal hydrides with key properties: the theoretical hydrogen mass ω_{H_2} , the working temperature Θ_{work} with the respective equilibrium pressure p_{eq} , the dehydrogenation enthalpy ΔH_{Des} and the thermal energy density ρ_{Th} [20]. For comparison the low temperature metal hydride $\text{TiMn}_{1.5}\text{H}_{2.5}$ was added to this table.

System	ω_{H_2} in mass - %	Θ_{work} in °C	p_{eq} in bar	ΔH_{Des} in kJ mol ⁻¹ H ₂	ρ_{Th} in kWh _{th} m ⁻³
MgH ₂ → Mg+H ₂	7.6	400	17	74	962
Mg ₂ FeH ₂ → 2Mg+Fe+3H ₂	5.5	564	150	77	1352
CaH ₂ →Ca+H ₂	4.8	1000	140	208	1949
NaMgH ₃ → NaH+Mg+H ₂	4.0	480	7.9	87	593
TiMn _{1.5} H _{2.5}	1.9	120	140	28	129

2.1. Magnesium hydride

2.1.1. Magnesium as hydrogen and heat storage medium

Magnesium and magnesium-based materials used as hydrogen storage material are subjected to research for 50 years. Because of its abundance, non-toxicity and relatively safe operation conditions, magnesium and the respective magnesium hydrides are prominent candidates for plenty of applications in the energy storage sector [20,23]. Magnesium has a relatively high volumetric (0.11 gH₂cm⁻³) hydrogen capacity [39], compared to storage of liquid hydrogen under cryogenic

temperature of 20 K ($0.071 \text{ gH}_2\text{cm}^{-3}$) [40, 41]. Due to the high reaction enthalpy of 75 kJ mol^{-1} [10] and a high operating temperature of approximately 350°C – 450°C of magnesium hydride, it is a good candidate as high-temperature metal hydride (HTMH) for heat storage application [10]. One of the most important advantages of using magnesium-based metal hydrides is the relatively low cost⁷ of the raw material of $1.93 - 3.65 \text{ \$/kg}$ [42]. This is important since installing an Mg-based heat storage system for a solar thermal power plant would require 1100 tons of magnesium to achieve stored energy of 1000 MW h (Andasol 1, Spain, 1000 MW h) [43]. Additionally to the application of MgH_2 as heat storage medium in thermal batteries for solar thermal power plants, it could be used to store waste heat from high-temperature industrial plants. It was subjected to investigations since the late 80's by Bogdanović et al. [18, 44–47]. Over the last two decades, large progress was made in developing heat storage systems on magnesium-based materials, in which tests were successfully conducted of more than 1000 cycles of hydrogenation and dehydrogenation [45].

2.1.2. Synthesis of magnesium hydride

There are three different approaches to prepare magnesium hydride. The first one is the direct synthesis from metal and hydrogen gas under pressure and at elevated temperatures ($> 280^\circ\text{C}$ [48]) in a reversible reaction, according to the following equation:



The synthesis by this reaction produces relatively inert hydrides which can be handled safely under air [49]. Choosing this reaction path, it is noteworthy that the starting magnesium has slow reaction kinetics, which results in the necessity to introduce catalysts.

The second approach is a homogenous catalyzed route in which magnesium is reacting in organic solvents with small amounts of transition metal catalysts [50]. One example of these is the reaction of magnesium with anthracene in order to form a highly reactive and soluble magnesium-anthracene. In the presence of chromium or titanium catalyst and hydrogen, magnesium hydride is formed. The anthracene is released during this reaction and can initiate a new reaction. This results in the

⁷A list of raw material cost per kWh is attached in Table A.7 in the Appendix.

2. Fundamentals of Metal Hydrides

synthesis of large amounts of magnesium hydride with the usage of small amounts of catalysts [23]. The advantages of this approach are the high kinetic activity and a reduced amount of catalyst, which are required to achieve a high yield of the hydrogenation reaction [43, 45, 50].

A third approach allows preparing magnesium hydride under room temperature and a hydrogen pressure of 2 bar. Reactive ball milling enables the formation of nano-crystalline magnesium hydride powder, with superior absorbing and desorbing kinetics.

During the hydrogenation reaction, the hexagonal magnesium transforms into rutile-type tetragonal magnesium hydride, which has a mixed ionic-covalent chemical bond. This reaction is accompanied by a volumetric increase of 20 % – 30 %, which is induced by reconstruction of the lattice. Subsequently, the density changes from $\rho(\text{Mg})=1.74 \text{ gcm}^{-3}$ to $\rho(\text{MgH}_2)=1.45 \text{ gcm}^{-3}$ [23, 51–53].

2.1.3. Kinetics

A problematic issue of pure magnesium hydride using as heat storage material is its weak kinetics during the absorption and desorption process of hydrogen. The formation and dissociation of magnesium hydride is a hetero-phase transformation and consists of several reaction steps, as transport of the hydrogen to the surface, dissociation and chemisorption of the H_2 molecules on the surface, migration of the hydrogen atom from the surface into the bulk, diffusion in bulk and the formation and growth of the metal hydride phase. Factors that cause the low kinetics during the absorption are the physisorption and dissociation of the hydrogen molecules on the particle surface, and the diffusion of the hydrogen through already formed magnesium hydride layer. This process is further limited by the natural magnesium oxide (or hydroxide) layer⁸, which normally covers magnesium particles. It was found that the hydrogen diffusion in grain boundaries and on the surface is much higher than in the bulk [16, 54]. The diffusion of the hydrogen atoms through the hydride layer is the rate-limiting step during the hydrogen desorption [54].

To achieve a reasonable reaction rate for the hydrogenation of magnesium, temperatures above 400 °C and a hydrogen pressure of 70 bar are required [23, 54]. For the dehydrogenation of magnesium hydride, the reaction temperature has to be > 400 °C [23].

⁸Magnesium particles are covered by natural magnesium oxide (hydroxide) layer, which reduces hydrogen diffusion into the particle [54].

To enhance the de-/hydrogenation kinetics, the dissociation and recombination of the hydrogen and the diffusion of hydrogen through the already formed magnesium hydride have to be improved. By increasing the number of grain boundaries in the magnesium particles, pathways are provided, in which the diffusion rate and thus the mobility of the hydrogen atoms is increased [54]. Adding catalysts to the magnesium enhances the rate of dissociation and recombination of hydrogen molecules at the surface of the particles, which has been strongly discussed and investigated in the scientific community [23, 54–57].

2.1.4. Catalytic activation by introduction of additives

In literature it is described, that transition metals as Ti, V, Mn, Fe, and Ni reduce the activation energy of the absorption and desorption of hydrogen and thus enhance the kinetics of the hydrogenation and dehydrogenation of magnesium hydride [55]. Similar behavior could be found for metal oxides [58] and metal halides [59], which have been added as catalysts. Introducing additives can enhance the kinetics at different stages of the reaction between magnesium and hydrogen. It can accelerate the dissociation of hydrogen molecules on the surface, it can form intermediate phases and thus grain boundaries in which hydrogen atoms diffuse faster than in bulk [16, 59] and it might prevent the magnesium to agglomerate or even enables the formation of nanostructures [60]. The agglomeration of magnesium is a crucial issue because it reduces the number of surfaces and interfaces in a packed bed of magnesium particles, which might lower the active sites on which hydrogen molecules are dissociated. Furthermore, it decreases the number of pathways for the hydrogen atoms and thus reduces the respective diffusion rate. Agglomeration causes a loss in hydrogen capacity and is thus responsible for the cycle instability of magnesium-based hydrides [19].

Three methods to introduce catalytic additives to magnesium hydride are presented in literature:

Bogdanović et al. presented a wet chemical process in which nickel particles were well and finely distributed over the magnesium particles. They achieved a very reactive and stable nickel-activated magnesium hydride with 2 mass – % nickel content [45–47].

The second approach, in which the additives are introduced as a powder (~ 5 mass – %) is a simpler and operational less complex one. In most cases, the

2. Fundamentals of Metal Hydrides

additives (transition metals, oxides or halides) are added, as powders, to magnesium hydride powder with a subsequent stirring, to improve the kinetics [54, 59]. Another less common approach is the usage of magnesium powder and transition metal powder as starting agents. The powder mixture is exposed to hydrogen pressure and temperature to initiate the hydrogenation.

The third approach is reactive ball milling, in which small amounts (a few mass – %) of catalyst powder (transition metals, metal oxides or halides) are added to magnesium hydride. The particle bed is exposed to ball milling and thus a mechanical treatment, in order to obtain nanostructured magnesium hydride [61]. The result of this method is the reduction of the grain size in the magnesium hydride, thus to take advantage of the fast hydrogen diffusion along the grain boundaries. Additionally, the catalysts are finely distributed over the magnesium particles. The product is nanostructured magnesium hydride, which benefits from lower desorption temperatures and high hydrogen capacity, as non-ball milled magnesium hydride [50, 62].

In literature and the metal hydrogen community, it is well known that magnesium hydride, which has experienced many hydrogenation-/dehydrogenation cycles suffer from slow reaction kinetics and loss in hydrogen capacity [50]. This might be caused by redistribution of the catalysts [57] and coarsening of the grains, especially if nanostructured magnesium hydride is cycled [63]. In literature, there are plenty of publications that describe possibilities to overcome slow kinetics. A few publications in the literature describe the introduction of Nb_2O_5 to enhance the hydrogen sorption in order to enhance the reaction kinetics at temperatures around 300 °C [58, 64].

2.1.5. Catalytic activation by downsizing

Another approach, which was addressed more in research during the last decade, is nanosizing and preparing nanostructures of magnesium hydride. The main improvement of reducing the size of the magnesium hydride structure is increasing the surface to volume ratio and therefore the number of active sites as edge and corner atoms, which are kinetically more active than bulk atoms [65]. There are different nano-structuring techniques described in the literature to improve the kinetics of magnesium hydride compounds e.g. High Pressure Torsion (HPT) [66] and reactive ball milling [67]. Experiments showed that nanocrystalline magnesium of 30 - 50 nm particle size is able to absorb hydrogen at 300 °C and 10 bar

hydrogen to achieve a hydrogen mass content of 6% after 120 min. Magnesium particles of 1 μm size do not absorb hydrogen under these conditions [68].

2.2. Magnesium iron hydride

To overcome the lack of cycle stability of pure magnesium-magnesium hydride heat storage systems, the usage of magnesium iron hydride Mg_2FeH_2 is under consideration for years [20]. The high degree of cycle stability is caused by the fact, that magnesium and iron do not form any alloys or intermetallic compounds, thus no sintering occurs, which would reduce reaction kinetics and the hydrogen capacity. This hydride can operate as heat storage material, at temperatures of 450 °C to 550 °C and thus exceeds the temperature range of magnesium hydride by at least 100 K [20, 23, 69]. Increased operating temperature is beneficial for heat-to-power efficiency (cf. Chapter 2) during the recovery of the stored energy. It operates at lower hydrogen pressure and at higher temperatures as magnesium hydride, as presented in Figure 6.1 and Table A.2, which is beneficial for the construction of heat storage tanks. In theory, Mg_2FeH_2 is capable of storing 5.5 mass – % of hydrogen, which results in 0.61 kW h kg⁻¹ of stored heat capacity. It is a ternary complex hydride, which is a green solid with a cubic crystal structure [70]. It reacts under air and water heavily exothermic.

2.2.1. Formation of magnesium iron hydride

The reaction towards magnesium iron hydride takes place in a process, in which at first magnesium hydride is formed. This magnesium hydride then reacts with iron and hydrogen to magnesium iron hydride. The mechanism on a molecular level is still unclear. The hydrogenation releases 77 kJ mol⁻¹ hydrogen [69].



The preparation of magnesium iron hydride is usually performed by mixing magnesium and iron powder to a stoichiometric mixture. This powder is exposed to a temperature of more than 450 °C and hydrogen pressures of 20 – 120 bar [10]. The formation could already occur at lower temperatures (e.g. 350 °C), but it is kinetically constrained by slow solid-solid diffusion processes [71]. Because of its

2. Fundamentals of Metal Hydrides

Table 2.4.: Hydrogen content and energy densities for magnesium hydride and magnesium iron hydride [10, 69].

	MgH ₂	Mg ₂ FeH ₂
Hydrogen content (theo.)	7.66 mass – %	5.47 mass – %
Reaction enthalpy	75 kJ mol ⁻¹	77 kJ mol ⁻¹
Gravimetric energy density	0.78 kW h kg ⁻¹	0.55 kW h kg ⁻¹
Volumetric energy density	1110 kWhm ⁻³	1513 kWhm ⁻³

simplicity of the preparation, the unarmful operating conditions and low-priced starting material, this is a convenient material for heat storage in up-scaled applications.

Other approaches are using reactive ball milling and/ or magnesium hydride as a starting agent to synthesize magnesium iron hydride [69]. These approaches lead to the formation of Mg₂FeH₂ which has fast kinetics and good stability. But metal hydrides which were prepared by these methods are rather for scientific purposes, because of the mostly sophisticated preparation of small amounts.

In literature, it was already presented that magnesium iron hydride has a theoretical hydrogen storage capacity of 5.47 mass – % of which 5.2 – 5.0 mass – % was retained after 550 – 600 cycles [69].

For comparison, the energy densities of magnesium hydride and magnesium iron hydride are presented in Table 2.4. The gravimetric energy density of magnesium hydride is higher than in magnesium iron hydride, whereas the volumetric energy density is higher in magnesium iron hydride.

3. Fundamentals of heat transfer in powder - gas systems

3.1. Heat transfer in non-reacting material

Applying magnesium-based metal hydrides as a heat storage material for high-temperature energy applications in up-scaled facilities, some problems and issues have to be considered, as e.g. the hydrogen diffusion in the metal hydrides during the de-/hydrogenation reaction. Another crucial issue is the heat transfer in a packed bed of metal hydride particles under a hydrogen atmosphere. This issue is of importance for the performance of a heat storage tank, because the hydrogenation is a strongly exothermic reaction, as shown in Chapter 2. In order to optimize the design and the operation of heat storage tanks the heat transfer in those packed beds have to be understood in full extend, especially under operating conditions (hydrogen pressure and temperature, Chapter 2). The magnesium-based hydrides are provided as particle beds, under gas atmosphere, to the energy storage application. Therefore the mechanism of the heat transfer, the thermal conductivity, in powder beds under gas atmosphere will be discussed in this Chapter.

Regarding the VDI Heat Atlas [72], the effective thermal conductivity ETC in a stagnant multiphase, as a packed bed under gas atmosphere, is a function of the thermal conductivity of the solid (the dispersed phase), the thermal conductivity of the gas (the continuous phase) and the packing density. The latter is defined by the ratio between the dispersed phase and the continuous phase. These are the so-called primary parameters.

Additionally, there are the secondary parameters, which may have as well influence on the effective thermal conductivity in a packed bed. These are mainly; the particle shape, the size distribution of the particles, mechanical properties of the particles, thermo-dynamical properties of the gas, the temperature of the packed bed and the gas pressure. Primary parameters are suggested to have a bigger

3. Fundamentals of heat transfer in powder - gas systems

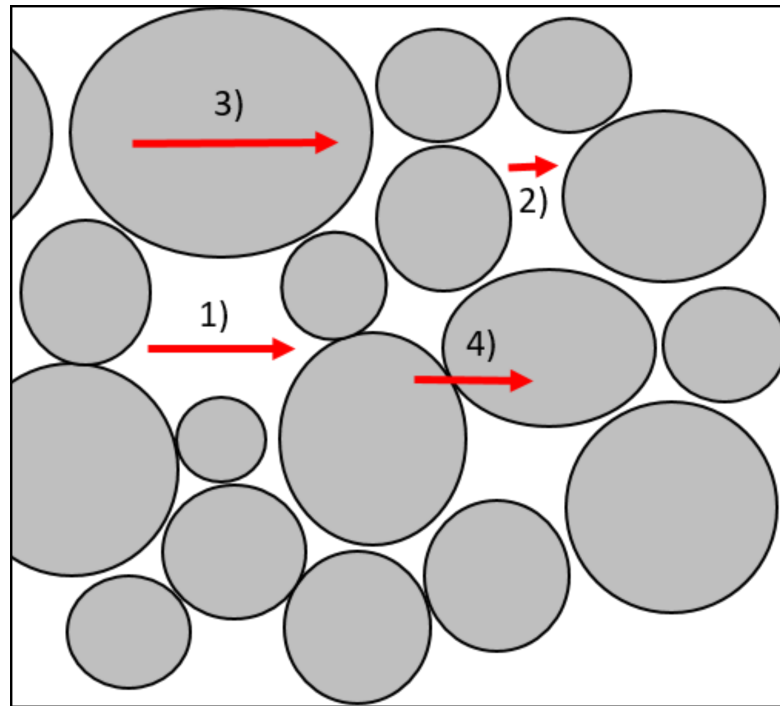


Figure 3.1.: Heat transfer mechanism in powder - gas system [72, 75].

impact on the effective thermal conductivity than secondary parameters [72, 73].

Discussing the heat transfer in a powder bed of metal hydrides requires some simplification in order to avoid complicating the heat transfer mechanism with negligible heat transfer routes. Following assumptions were made:

- Radiation can be neglected in the equilibrium state of the metal hydride powder bed since there is no big temperature difference, expected to be in such a particle bed. A large temperature difference would be required for heat transfer via radiation in a measurable amount. Radiation would contribute significantly to the overall heat transfer if the sample temperature is high and gas pressure is low thus heat transfer via conduction is low [72, 74].
- Convection can be neglected in the most practical cases because the voids must be in the range of some centimeters to have an impact on the heat transfer [73]. The size of the voids is considered to be in the same range as the particle diameter, thus in the order of a few microns to a maximum of 297 μm (Table 6.1). Therefore, no convection will contribute to any significance to the overall heat transfer in the packed bed [74].

There are several routes on which heat is transferred in solid-gas compositions, as depicted in Figure 3.1. It presents the heat transfer in large gas voids (1), in

3.1. Heat transfer in non-reacting material

small gas voids (2), in solid particles (3) and from particle to particle (4). To gain a better understanding of the heat transfer in a powder-gas system each of the above-mentioned heat routes will be discussed separately.

3. Fundamentals of heat transfer in powder - gas systems

3.1.1. Thermal conductivity of gases

The heat transfer in the hydrogen gas in this work can be described with the help of the ideal gas law. The physical meaning of this assumption is, that gas molecules are considered to be sphere-like objects, which exchange kinetic energy via collision. No other interactions occur among them.

The thermal conductivity κ of an ideal gas can be calculated with [76]:

$$\kappa = \frac{1}{3} \cdot \lambda \cdot \langle \nu \rangle \cdot C_V \cdot \frac{n}{V} \quad (3.1)$$

For calculating κ , the specific heat C_V of the gas, the number of molecules n in the fixed reservoir V (concentration), the mean free path λ and mean velocity $\langle \nu \rangle$ of the molecules has to be considered. The mean velocity $\langle \nu \rangle$ in this equation is simplified to one dimension and can be expressed as [76]:

$$\langle \nu \rangle = \sqrt{\frac{8k_B T}{\pi m}} \quad (3.2)$$

The velocity of the gas molecules depends on the temperature T , the Boltzmann constant k_B and the mass of a molecule m . The mean free path λ of a molecule can be described with [76]:

$$\lambda = \frac{k_B T}{\sqrt{2} \sigma p} \quad (3.3)$$

The collision cross section¹ of the molecules is described with σ and the gas pressure p .

To prove the validity of the ideal gas law for discussing the thermal conductivity of the hydrogen gas the compressibility factor or real gas factor Z will be determined in the following. The real gas factor describes the deviation of the behavior of a real gas from the ideal gas and is defined as the ratio of the molar volume of the real gas V_m and the molar volume of the ideal gas V_m^0 .

$$Z = \frac{V_m}{V_m^0} \quad (3.4)$$

¹The cross section area of hydrogen molecules is 0.27 nm^2

3.1. Heat transfer in non-reacting material

Because V_m^0 can be expressed with:

$$V_m^0 = \frac{RT}{p} \quad (3.5)$$

the Z value can be described with:

$$Z = \frac{V_m p}{RT} \quad (3.6)$$

Z can be calculated from the pressure p , the molar volume V_m , the temperature T and the gas constant R . Z is increasing with increasing pressure and decreasing temperature. Calculations have shown that the deviation from the ideal gas behavior is 6 % in the worst case (25 °C and 100 bar). The calculations were performed according to equation A.6 and A.7 in the Appendix from [24, 77].

3.1.2. Contribution of the ideal gas in a packed bed to the thermal conductivity

The thermal conductivity of the gas is linked to the motion of the gas molecules because the energy is transferred via the collision between the molecules. In a dilute ideal gas, which is unconfined in space, the thermal conductivity does not experience a pressure dependency, according to the kinetic gas theory² [72]. But it is only valid for gas in an infinite volume with no outer boundaries, which limit the movement of the molecules. In the case of metal hydride powder beds, this assumption is not entirely valid, because the gas is confined in an open pore system. If the mean free path λ of the molecules is much smaller than the representative physical length scale L , which equals the void (e.g. pore) size, the pressure independence is still valid. But if the pressure is decreasing, the mean free path increases. This causes a reduced number of collisions among the molecules, thus the energy, which is transported is declining. This results in the lowering of the thermal conductivity, introduced by reduced gas pressure.

$$Kn = \frac{\lambda}{L} \quad (3.7)$$

²The mean free path is decreasing with increasing pressure p (cf. Equation 3.2). The thermal conductivity κ would rise with an increased pressure, because the mol number n of hydrogen is increasing with an enhanced gas pressure (cf. equation 3.1). Equations 3.1 and 3.2 are counteracting the pressure dependency.

3. Fundamentals of heat transfer in powder - gas systems

Table 3.1.: Flow regimes and respective Knudsen numbers [78].

Regime	Knudsen number	Respective pressure ³ ($L = 1 \mu\text{m}$, $T = 298 \text{ K}$)
Continuums regime	$0 < Kn < 10^{-2}$	$-\infty - 40 \text{ bar}$
Transition regime	$10^{-2} < Kn < 10$	$40 \text{ bar} - 0.4 \text{ bar}$
Free molecular regime	$10 < Kn < \infty$	$0.4 \text{ bar} - \infty$

The ratio between λ and L is expressed by the Knudsen number Kn and indirectly expresses the pressure dependency of the thermal conductivity in the gas. Therefore, the motion of the gas and its pressure dependency can be separated into three regimes, expressed by the Knudsen number as presented in Table 3.1.

In continuums regime ($> 40 \text{ bar}$) the voids (pores) are filled with gas molecules, the interaction/collisions between gas molecules are exceeding gas–boundary collisions because the mean free path of the molecules is much lower than the pore size. In this regime, the thermal conductivity of the gas is independent of the gas pressure because an increased pressure would decrease the mean free path but would enhance the number of molecules (Equation 3.1 and 3.3).

In the free molecular regime, the mean free path is much larger than the pore size thus the interaction/collision between the gas molecules and the solid interfaces are exceeding the molecule–molecule interactions. If a gas molecule interacts with the surface of a particle with elastic collision, no energy is transferred. The ratio of impacts in which energy is transferred (inelastic collisions) to elastic collisions is described by the accommodation factor. The accommodation factor depends on a lot of properties as the molar mass of the molecule, the gas/solid temperature and the surface properties of the particle (e.g. roughness and crystallinity) [73,74]. The accommodation factor is a number between 0 and 1. A high accommodation factor implies a good energy transfer across the gas-solid interface. In this regime, the thermal conductivity of the gas is pressure independent. In this work, experiments will not be executed at the pressures of the free molecular regime.

In the transition regime, in which the mean free path of the molecules and the

3

The respective gas pressure is calculated with assumption of a void size of $1 \mu\text{m}$, a temperature of 298 K and a collision cross section of the hydrogen $\sigma = 0.27 \text{ nm}^2$.

3.1. Heat transfer in non-reacting material

average pores are of comparable size, the number of the molecule–molecule collisions and the number of the molecule–surface collisions is in the same order of magnitude. If the number of molecule–molecule collision is increasing the thermal conductivity increases as well. The number of collisions can be increased by reducing the mean free path of the molecules, which is a consequence of increasing gas pressure. The increasing thermal conductivity by rising gas pressure is commonly called Smoluchowski effect [73]. The reduced thermal conductivity κ_r of the gas in a powder bed can be described by [74]:

$$\kappa_r = \frac{\kappa_{\text{gas}}}{1 + 2\beta Kn} \quad (3.8)$$

It can be estimated with the thermal conductivity κ_{gas} of the diluted and unconfined gas, the Knudsen number Kn . The dimensionless factor β quantifies the efficiency of the energy transfer between the gas molecules and the solid surface. It depends on the type of gas and the material [79] and can be calculated with the following equation:

$$\beta = \frac{2(1 + M_R)^2 - 2.4M_R}{2.4M_R} \quad (3.9)$$

M_R is the ratio of the molar mass of the gas M_g and the molar mass of the solid M_S :

$$M_R = \frac{M_S}{M_g} \quad (3.10)$$

3.1.3. Thermal conductivity of solids

The heat transfer in solids can be described by their thermal conductivity and has its origin in the movement of electrons or phonons as energy carriers. The heat transfer mechanism is strongly related to the state of the metal hydride, whether it is in hydrogenated (non–metallic: electrical insulating) or in dehydrogenated (metallic: conducting) state [80].

In the metallic, dehydrogenated state of the metal hydride, the heat is transferred by phonons and free electrons, as it is common in conducting materials. Lattice vibrations and free electrons can contribute to the energy (heat) transport. The thermal conductivity of an electrically conductive solid is related to its electrical conductivity, regarding the Wiedemann-Franz law [81]. Thus the heat transfer

3. Fundamentals of heat transfer in powder - gas systems

capability is enhanced by the free electrons.

If the metal hydride is in the hydrogenated state it is electrically insulating, because it does not have free electrons, which could contribute to the charge transport. Since the energy (heat) cannot be carried by electrons, the heat transfer mainly can be described with the group velocity of phonons, which are basically the lattice vibrations. This is the displacement of an atom from its equilibrium position. Due to the fact that atoms are connected to each other in condensed matter, this displacement propagates with a wavelength Λ through the bulk. In this case, the thermal conductivity can be derived in first approximation from the kinetic theory of gases [81]. The heat transfer depends on the mean free path of the phonons which can be related to the number of defects, grain boundaries, and other phonons.

3.1.4. Contribution of the solid particles in a packed bed to the thermal conductivity

Considering the path-way of heat transfer in the solid phase of a powder bed, parameters as the particle shape, the average size and the size distribution of the powder arrangement might have a big impact. These parameters determine mainly the overall and specific contact area between the particles. A high contact area between the particles reduces thermal resistances and therefore leads to an enhanced heat transfer in the solid phase [82].

3.1.5. Temperature and gas pressure dependency of the heat transfer mechanism

Since this work is about the heat transfer of high-temperature metal hydrides under elevated gas pressures and temperatures the influence and dependency of every single above-mentioned mechanism is given in Table 3.2. The thermal conductivity in the solids does not change with the pressure and there is almost no influence on the heat conductivity of unconfined gas. In the transition regime of a confined gas, the thermal conductivity increases with increasing gas pressure and can be described by the Smoluchowski effect. The heat transfer capability of metallic solid is decreasing with rising temperature, whereas the heat transfer in non-metallic (hydrogenated) materials is rising with the temperature. For confined hydrogen

3.1. Heat transfer in non-reacting material

Table 3.2.: Temperature and pressure dependency of the thermal conductivity of single heat transfer paths.

Heat transport in	Temperature dependency	Pressure dependency
Unconfined hydrogen	$0.171 \left(\frac{K}{273.15}\right)^{0.69}$ [83]	Very small increasing with enhanced pressure
Hydrogen in powder bed	Proportional to $T^{\frac{1}{2}}$	Continuums regime: small dependency Transition regime: Thermal conductivity increases with increasing pressure (Smoluchowski effect)
Solid: metallic	Decreases with temperature [84]	No dependency
Solid: non-metallic	Increases with temperature [81]	No dependency

Table 3.3.: Thermal conductivity values of contributing phases of magnesium/ magnesium hydride powder bed (Calculated for hydrogen [85]).

Material	κ in $\text{W m}^{-1} \text{K}^{-1}$	κ in $\text{W m}^{-1} \text{K}^{-1}$
	at 300 K and 1 bar	at 600 K and 1 bar
Mg	156^5 [86]	145 (573 K) [87]
H ₂	0.185 [85]	0.318 [85]
MgH ₂	?	?

gas it increases with the square root of the temperature [83].

Table 3.3 presents an overview of the thermal conductivities of magnesium, hydrogen and magnesium hydride, at a room temperature (298 K) and at an elevated temperature of 600 K. As clearly visible, the thermal conductivity of solid crystalline magnesium is higher than $150 \text{ W m}^{-1} \text{K}^{-1}$, whereas hydrogen gas with $0.185 \text{ W m}^{-1} \text{K}^{-1}$ has a much lower heat transfer capability via conduction. For pure bulk magnesium hydride, there are been no values available in the literature⁴.

⁴To the knowledge of the author, there are no values of bulk MgH₂ thermal conductivity published. (June 13, 2019)

⁵The thermal conductivity depends on the temperature and microstructure.

3.2. Heat transfer in high temperature metal hydrides under operating conditions

Until now, the thermal conductivity of a non-reacting powder was discussed. Metal hydride powder experience changes in their spatial arrangement due to volume expansion and contraction during hydrogenation and dehydrogenation, respectively. An expansion of the metal hydride particles initiates a change of the void size and in porosity (void fraction). Additionally, a growth of the solid particles in a confined volume leads to a change in the contact area between the particles and its contact force (plastic deformation) of ductile solids [51, 82, 83].

Particles, which are in a confined volume, might experience a mechanical pressure during expansion. This pressure might cause deformation at the contact area of the particles and thus increase the cross-section area between those particles (Hertzian contact stress) [82, 83].

This increased contact area reduces the heat resistance between these particles and benefices the intra-particle thermal conductivity. Simulation and modeling approaches of the heat transfer between solid bodies have shown that the thermal conductivity strongly depends on the contact area [88].

A second issue is the sintering of metallic particles under temperatures, which are above the sintering temperature. This starts roughly at $\frac{2}{3}$ of the bulk melting temperature. Therefore the sintering temperature of magnesium is 342 °C. It was shown that metallic magnesium powder experiences sintering at elevated temperatures of 400 °C [43], and after a few cycles of hydrogenation and dehydrogenation

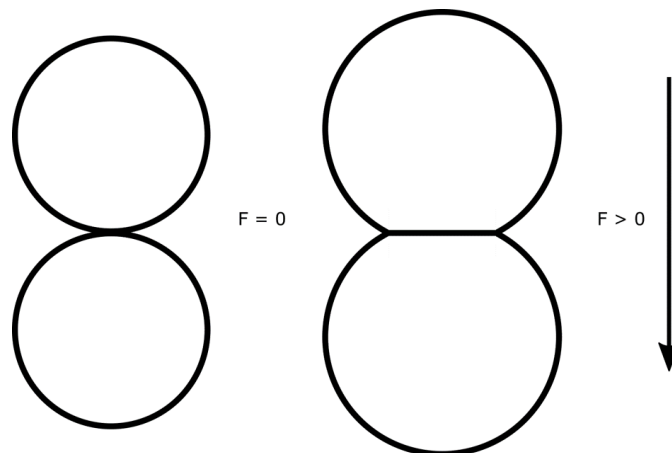


Figure 3.2.: Hertzian contact stress of particles caused by an external force F and thus an increased contact area between these particles.

3.3. Methods to determine thermal conductivity

it forms a stable interconnected network [44, 89]. This changes the heat transfer paths fundamentally and results in higher thermal conductivity.

3.3. Methods to determine thermal conductivity

Measuring the thermal conductivity of packed beds can be performed by either steady-state or transient methods. An example of a steady-state method is the comparative method in which the test material is placed between two reference materials. Thermocouples are inserted along the assembly. Heat is applied on one side of the sample. After a stable (steady-state) thermal gradient is present, the temperature profile can be used to calculate the thermal conductivity of the test material [90, 91]. The second approach is the transient method of determining thermal conductivity. The advantage of a transient method over a steady-state method is a relatively short measurement time because it is not necessary to wait for thermal equilibrium, to determine the thermal conductivity of the sample [92]. Additionally, it is possible with most of the transient methods to measure the thermal diffusivity, which allows the calculation of the specific heat of the sample, without using a calorimeter [93, 94].

There are different transient methods to determine the thermal conductivity of materials, as the Laser Flash method, the 3ω -method and the Transient Plane Source TPS method. Each of them has its advantages and limitations, which must be considered while choosing the best suited for the respective material of interest.

The Laser flash method utilizes a light source, as Laser or a flashlamp to heat one side of a disc sample in order to detect the time-dependent temperature rise on the other side with an IR-detector. This technique is limited to thin bulk samples with a smooth surface. Additionally, the laser flash method operates only in ambient conditions, which makes measurements under hydrogen pressure of up to 100 bar and temperatures of up to 520 °C impossible to perform. Another transient method is the 3ω -method, in which four heaters are attached to the surface of the test material. The heaters are heated periodically, in which four heaters are attached to the surface of the test material. The heaters are heated periodically, which causes an oscillation of the temperature. By evaluating the frequency of this oscillation, the thermal diffusivity and thermal conductivity can be calculated. The usage of this method for the determination of the thermal conductivity of high-temperature metal hydrides is not possible, because it requires

3. Fundamentals of heat transfer in powder - gas systems

a smooth surface at which the heaters can be attached. This can not be realized in packed beds of metal hydrides.

The transient plane source method, developed by the Hot Disk Company, can be applied to measure the thermal conductivity of high-temperature metal hydride powder beds under operating conditions. It enables the determination of the thermal conductivity, thermal diffusivity and (volumetric) specific heat of the sample material in a single measurement. The principles of this measurement will be introduced in Chapter 4.1.1.

3.4. Literature survey of theoretical and practical work concerning the thermal conductivity in metal hydride powder beds

An overview of work on heat transfer in metal hydride powder beds is briefly discussed in this chapter. At first, some theoretical approaches will be mentioned and then some of the experimental work.

3.4.1. Modelling of thermal conductivity in porous media

Researchers are trying to calculate and simulate the heat transfer in porous media for more than 100 years [72]. The theoretical approaches to solve the problem of thermal conductivity in porous media can be divided into three types.

The first model is based on the solution of the Laplace equation for heat conduction, which can be solved by analytical computation of the temperature field. The second method is a combination of resistances, based on the ohmic resistance model, which are in series, in parallel, and in combination. It is a quick but enormous simplified and less precise approach. The third method is based on a unit cell model in which parallel isotherms or parallel lines of the heat flux are assumed. It is a compromise of the first model, which is complicated but accurate and the second model, which is a simple but relatively unprecise model [72]. One of the most promising models is named after its inventors; Zehner/Bauer/Schlünder. The third model is considered for practical usage.

Even though a lot of parameters and detailed features of a packed bed are discussed in these models, the prediction of the thermal conductivity in packed beds still

3.4. Literature survey

leads to an error of 30 % [72]. It offers a possibility to get a rough approximation of the heat transfer in metal hydride powder beds under operating conditions.

In 2012 Fisher et al. [82] published a work based on a multiphysics modeling approach of heat conduction in $\text{Ti}_{1.1}\text{CrMn}$ powder bed in which the changing of particle shape distribution, size distribution, packing structure and their influence on the effective thermal conductivity were considered. The accuracy of this model was verified by experimental determination of the effective thermal conductivity at different packing densities. This model seems to allow a relatively precise prediction of the thermal conductivity of low-temperature metal hydrides but it does not include sintering effects and other major structural changes. Therefore, this modeling approach is mainly limited to low-temperature metal hydrides.

The theoretical prediction of the heat transfer for high-temperature metal hydrides is more challenging due to a larger variety of changing secondary parameters (as particle-size, -shape, -composition, -surface, etc.). For the simulation of the heat transfer in high-temperature metal hydride powder, as magnesium hydride, there are some parameters, which have to be considered. The material is mostly a binary composition of magnesium and magnesium hydride, due to non-complete conversion. The volume of the particle increases during the hydrogenation and shrink during the dehydrogenation. This is accompanied by fracturing and refining of the particles, caused by mechanical stress. Coarsening and sintering of particles might be caused by elevated temperatures of $> 400\text{ }^\circ\text{C}$. Oxide contamination and formation of a magnesium oxide phase on particle surfaces and thus a change of the surface morphology will cause a change in the thermal properties of the material. This results in the variation of the accommodation factor. The accommodation factor is a numerical value, which considers the incomplete exchange of energy during the collision of a gas molecule and the surface of a particle. It depends on the molecular structure of the surface, whether crystalline or amorphous, on the roughness of the surface, and if any other absorbing layers are covering the particle surface [95]. The accommodation factor of hydrogen was determined to be 0.36 at room temperature [96].

3.4.2. Experimental work on thermal conductivity measurements of metal hydrides as heat storage material

Since simulations are still not fully satisfying in delivering accurate values of the effective thermal conductivity in high-temperature metal hydrides, a few experimental investigations were presented in literature over the past few decades.

Ono et al. showed that the thermal conductivity of fully hydrogenated magnesium hydride increases with increasing hydrogen gas pressure. They measured an ETC of up to $1.3 \text{ W m}^{-1} \text{ K}^{-1}$ at $200 \text{ }^\circ\text{C}$ and 40 bar hydrogen. At this temperature, no sintering of the particles occurs, which would result in compaction and densification [95].

Kapischke and Hapke [52] developed a reactor set-up, equipped with 5 thermocouples, for an indirect determination of the thermal conductivity of a magnesium hydride powder bed under operating conditions, including the effect of volume expansion of the magnesium due to hydrogenation [97]. In this work, the assumptions were made, that the temperature is the same all over the material, that there are no inhomogeneities and that the thermal conductivity is constant over a temperature range of 20 K [52]. Under these assumptions, they determined an effective thermal conductivity of approximately $4 \text{ W m}^{-1} \text{ K}^{-1}$ at $400 \text{ }^\circ\text{C}$ and 19.4 bar hydrogen in the fully hydrogenated state of the magnesium hydride. The absolute error of a single measurement was calculated to be $\pm 1.4 \text{ W m}^{-1} \text{ K}^{-1}$ and the mean error of 10 measurements was $\pm 0.4 \text{ W m}^{-1} \text{ K}^{-1}$. Four years later, a second method by Kapischke et al. [83] was presented in which the same set-up was used with an oscillating heating source. The temperatures in the sample were recorded at different distances to the heating sources. With the temperature increase and the delay time between the heating and the measurement, the effective thermal conductivities were estimated. This method describes indirectly the heat transfer in a cylindrical tube, filled with magnesium hydride, at temperatures of 250, 320, 350 and $380 \text{ }^\circ\text{C}$ under hydrogen pressures of 0.4, 2.8, 5.9 and 11.5 bar, respectively. The maximum relative error was calculated to be 12%. Both publications show different results of the ETC as a function of the hydrogen content in the magnesium hydride. With the first measurement set-up in [52], the ETC decreases with increasing hydrogen content. In contrast to that, the results in [83] show that the ETC reaches a maximum after approximately 2.5 mass-% of hydrogen has been absorbed in the magnesium. This leads to the conclusion that the presented values

3.4. Literature survey

strongly depend on the measurement set-up and the experimental method.

The effective thermal conductivity is an extrinsic parameter that strongly depends on the gas pressure, temperature and preparation conditions of the investigated material. Microstructure, annealing conditions, porosity, and particle distribution define the thermal conductivity in a metal hydride beds [98].

4. Characterization Methods of Metal Hydrides

As mentioned above, in this work the Transient Plane Source method is chosen to determine the effective thermal conductivity of the metal hydride powder beds, which are presented in Table 6.1 (Chapter 6).

4.1. Thermal Conductivity measurement

4.1.1. Transient-Plane-Source-Method

To determine the effective thermal conductivity of the metal hydride powder beds under hydrogen atmosphere the TPS method was used. The Transient Plane Source method (TPS) is an absolute and transient approach for determining the thermal diffusivity, the thermal conductivity and the volumetric specific heat of bulk materials, liquids and more complex systems as powder beds under different gas atmospheres, pressures, and temperatures [99]. It is a transient method because a heat pulse is applied to the test material, whereupon the temperature increase is recorded. The measurement period is mostly in the range of a few seconds [100].

The TPS method uses a thin nickel disk as both a plane heat source and a temperature sensor. During the measurement, an electrical current is applied by a constant voltage source through the resistive element R of the sensor, via the two contact pads, which are closer to the sensor head (Figure 4.1). Because of a distinct electrical resistivity in the double spiral head of the sensor, it will be heated up. This temperature change depends on the thermal properties of the surrounding test material and raises anti-proportional with the thermal conductivity of the testing material. The temperature increase in the sensor causes a raised electrical resistance R in the sensor, which will be measured by a change of voltage $U1$. By

4. Characterization Methods of Metal Hydrides

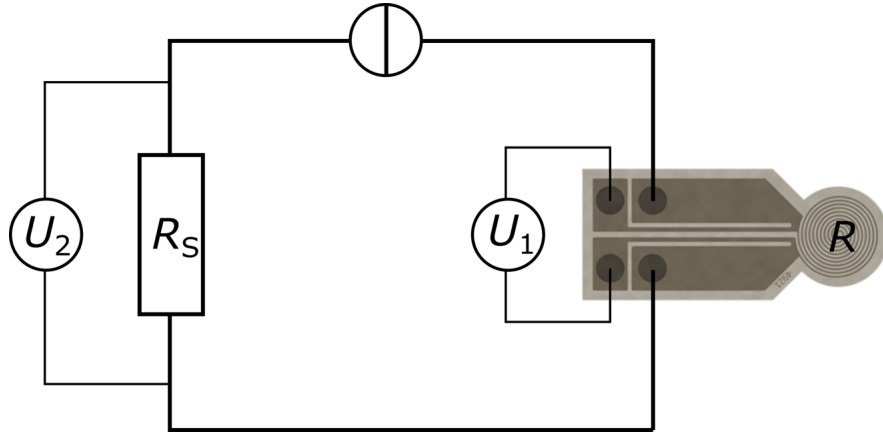


Figure 4.1.: Simplified circuit layout which connects the sensor for measuring the thermal conductivity with the TPS method.

comparing the voltage U_1 and U_2 and using the principle of a Wheatstone bridge the change of electrical resistivity R can be determined precisely.

The sensor, which was applied in this measurement method, is presented on the right side in Figure 4.1. It consists of 4 electrical contact pads, depicted by the four dark grey cycles in the left part of the sensor. On the right side of this sensor, one can see a double spiral, which forms the sensor head. The probing material of the sensor is a nickel strip of $10\ \mu\text{m}$ thickness, which is covered on both sides by an insulating layer. Depending on the desired temperature range, in which the measurements will be executed and if some special requirements, e.g. corrosion resistivity is needed, three different types of electrically insulating layer materials are offered by *Hot Disk AB* [94], which are presented in Table 4.1.

In this work a Kapton covered sensor with a radius $r = 3.189\ \text{mm}$ and a thickness $d_{\text{sensor}} = 50\ \mu\text{m}$, was used for the investigation of the thermal conductivity of the

Table 4.1.: Types of insulating material of the TPS sensor with operating temperature range and remarks for application.

Type of insulation	Temperature range	Remarks for application
Kapton (Polyimide)	$-243\ ^\circ\text{C} - 300\ ^\circ\text{C}$	Reusable
Mica (sheet silicate)	$< 1000\ ^\circ\text{C}$	Considered as consumable (delaminates easily)
Teflon (PTFE)	$-196\ ^\circ\text{C} - 250\ ^\circ\text{C}$	Chemically inert (for corrosive, sticky, reactive and acidic samples)

4.1. Thermal Conductivity measurement

magnesium powder, as described in Chapter 6.2. A sensor with a Kapton sealing was used, because it does not delaminate as quick as a sensor with other insulation materials, thus it lasts longer and can be reused for other experiments [94]. For measuring the ETC of the magnesium-based hydrides, the Mica covered sensor was applied. The radius of the sensor is $r = 3.189 \text{ mm}$ and the thickness $t_{\text{sensor}} = 211 \text{ }\mu\text{m}$. The Mica sensor was used because the operating temperature of the investigated metal hydrides is exceeding the operating temperature of Kapton.

The sensor is connected to the TPS 2500 S (Hot Disk Thermal Constants Analyser), which supplies the sensor with power for the measurement and records the temperature change in the sensor.

The measurement of the thermal conductivity with the TPS method is performed by the measurement of the electrical resistance of the sensor and its change due to a temperature change. The *Hot Disk Thermal Constants Analyser (v. 7.2.10)* software calculates the thermal conductivity. In the following, the calculation procedure will be described.

The resistance of the sensor R_T is described as a function of an initial resistance of the sensor prior to the measurement R_0 , the temperature coefficient of the resistivity α_{TCR} , and the determined temperature change ΔT as shown in equation:

$$R_T = R_0[1 + \alpha_{\text{TCR}}\Delta T(t)] \quad (4.1)$$

The temperature change $\Delta T(t)$ (presented in the left graph of Figure 4.2) is described by following equation.

$$\Delta T(t) = \Delta T_i(t) + \Delta T_s(t) \quad (4.2)$$

The total temperature change in the sensor is a sum of the temperature change at the surface of the sample $\Delta T_s(t)$ and the temperature change of the insulating (Kapton, Mica or Teflon) layers $\Delta T_i(t)$. The temperature increase in the insulating layer will always be constant after a very short time and can be estimated by:

$$\Delta t_i = \frac{\delta^2}{\alpha_i} \quad (4.3)$$

To estimate the time Δt_i the thickness of the layer δ and the thermal diffusivity of the insulating material α_i is required. The sensor thickness and thus the insulating layer are very thin. Each single insulating layer is in a range of 7 –

4. Characterization Methods of Metal Hydrides

100 μm^1 . Therefore, the temperature stabilization time in the insulating layer can be considered to be very short, in comparison to the overall measurement time.

Assuming that the probe consists of concentric and equally spaced ring sources, it can be considered to be a circle. With this assumption, the temperature change $\Delta T_S(t)$ can be expressed by the thermal conductivity κ of the sample and a dimensionless specific time function $D(\tau)$ [93].

$$\Delta T_S(t) = \frac{P_0}{\pi^{\frac{3}{2}} r \kappa} D(\tau) \quad (4.4)$$

In this function, P_0 is the output power of the sensor and r is the radius of the double spiral sensor head. The function $D(\tau)$ is a time function of the variable τ , which can be described by:

$$\tau = \frac{\sqrt{t \alpha_{\text{sample}}}}{r} \quad (4.5)$$

In this time function, the variable t expresses the actual measurement time and α_{sample} the thermal diffusivity of the sample. This equation has to be extended by the term t_c , which expresses the time correction to compensates software and hardware delays. This time correction is needed, because the full output power of the sensor may not coincide with the time $t = 0$. Therefore, the τ is replaced in equation 4.3 by the corrected value τ_c^2 .

$$\tau_c = \frac{\sqrt{(t - t_c) \alpha_{\text{sample}}}}{r} \quad (4.6)$$

The calculation of the thermo-physical properties (α and κ) is initiated by iteration steps in which the time correction t_c and the thermal diffusivity α , as optimization variables, are changed until a linear relationship between $\Delta T_S(t)$ and $D(\tau)$ is obtained, as shown in right graph in Figure 4.2. Thus the time correction t_c and the thermal diffusivity α are determined. The relation of the slope of this linear function gives the thermal conductivity κ .

By applying the following equation:

$$C_V = \frac{\kappa}{\alpha_{\text{sample}}} \quad (4.7)$$

¹A Mica insulation layer is thicker than Kapton insulation layer, therefore it is recommended to use Kapton covered sensors, if possible. Because of a thinner insulation, Kapton sealed sensors yield more accurate results [94].

²The time correction is normally less than 0.5 % of the total measurement time.

4.1. Thermal Conductivity measurement

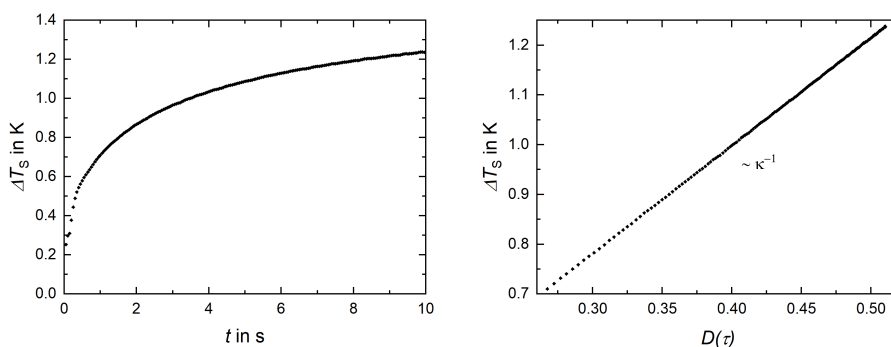


Figure 4.2.: Temperature increase of the sensor with the measurement time (left) and Temperature increase as function of the time function $D(\tau)$. (Values recorded to plot these graphs were recorded during the ETC measurement of dehydrogenated MgH_2 at 1 bar hydrogen and 400°C .)

the volumetric heat capacity C_V of the powder gas system can be determine [93].

4.1.2. Measurement procedure

In this chapter, the experimental approach for measuring the effective thermal conductivity of a powder bed under a gas atmosphere will be described. Having a well-defined and controlled procedure for determining the ETC is helping to achieve the utmost reliable results which are possible.

At first, the size of the sensor has to be considered. The radius of the sensor should be chosen to be considerably larger than the voids in the powder bed and thus the particle size [101]. This is important because the sample should be considered to be homogeneous. As mentioned above, a sensor with a radius of 3.189 mm was chosen.

As insulating layer for the sensor material serves Mica, which is a sheet silicate of the following composition: $\text{X}_2\text{Y}_{4-6}\text{Z}_8\text{O}_{20}(\text{OH}, \text{F})_4$. The contained elements are presented in Table 4.2 [102].

Table 4.2.: Elements in sheet silicate (Mica) insulation layer of the TPS sensor.

	Common elements	Less common elements
X	K, Na or Ca	Ba, Rb or Cs
Y	Al, Mg or Fe	Mn, CR, Ti, Li ect.
Z	Si or Al	Fe^{3+} or Ti

4. Characterization Methods of Metal Hydrides

The composition of the Mica covered sensor enables working temperatures of up to 800 °C. Whereas, the polyimide covered sensor (Kapton) withstands temperatures up to 300 °C. The advantage of using the Kapton sensor lies in the durability and thus the reusability of the sensor, whereas Mica-covered sensors might delaminate quicker, thus there are not reusable.

Another crucial point which makes the usage of a protecting layer absolutely required is the electrical insulation of the nickel to the sample material. Without electrical insulation, the applied current could pass through the sample and voltage readings and thus the determination of the electrical resistance in the sensor head would suffer from errors and failures.

The sensor has to be embedded in the center of the powder bed, as depicted in Figure 4.3. It is favorable to place it in the center of the sample to locate it as far as possible from outer boundaries. As a rule of thumb, it is necessary to ensure that the possible probing depth is exceeding the radius of the sensor [93]. This is necessary to avoid any influence or disturbance from external factors during measurements.

After the sample material and a suited sensor are placed in the measurement set-up, the determination of the thermal conductivity can be initiated. For this method, it is necessary to guarantee a thermal equilibrium in the material and the set-up to avoid any disturbance during the measurement. Therefore, it is important to stabilize the system before starting any measurement. After attaching the measurement cell to the gas supply system, the hydrogen purging step, according

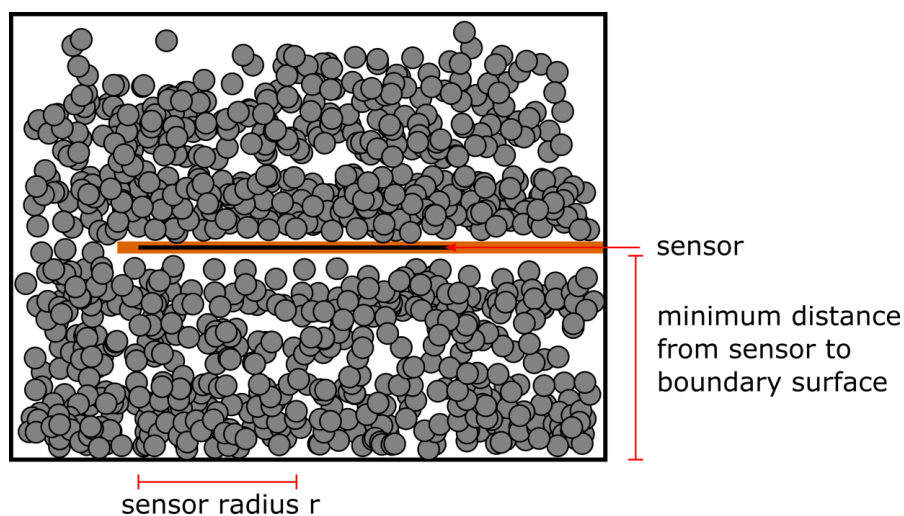


Figure 4.3.: Profile of the sensor which is embedded in sample powder.

4.1. Thermal Conductivity measurement

to Chapter 5, has to be performed³. After this, the desired temperature must be adjusted. Once the desired temperature is reached, the pressure can be set by opening the valve for the gas inlet or outlet (see Figure 5.1). After the pressure is stabilized a short waiting time is mostly necessary in order to overcome thermal fluctuations, which are caused by expansion or compression of the gas. This strongly depends on the chosen rate for a pressure change. At the point when the pressure and the temperature are in equilibrium, the first measurement can be executed.

There are some parameters that are important to be fed into the *Hot Disk Thermal Constants Analyser* (v. 7.2.10) software. At first, the sample temperature must be entered because the software includes a dataset of the temperature coefficients of electrical resistivity of the nickel sensor material, otherwise, the later conversion from electrical resistance in the sensor to the temperature change (see Equation 3.9) will not be correct.

The second important parameter is the time of the transient reading during the measurement procedure. The measurement time t is directly linked to the probing depth Δ_p and the thermal diffusivity α .

$$\Delta_p = 2\sqrt{\alpha_{\text{sample}}t} \quad (4.8)$$

The probing depth in the sample shall not exceed the double of the shortest distance between the sensor and any outer boundary, as shown in Figure 4.3. The constant 2 for defining the required probing depth, was determined by [101]. It ensures that there is no influence of any external sample boundaries on the temperature of the sensor. Just heat propagation waves are considered that could not move more than double than the minimum distance between the sensor and the surface of the out boundary. This means, samples with a high thermal diffusivity α_{sample} need to be measured in shorter time than thermal insulating samples.

The third parameter for setting the measurement is the output power of the sensor during transient reading. The increase of the sensor temperature correlates linearly with the output power. As a rule of thumb, measuring thermal insulating materials requires around 50 mW output power, without damaging the sensor by overheating. High conducting sample material can handle a higher output power,

³In case of metal hydrides, which have to be handled under inert gas, the test rig has to be purged with hydrogen after attaching, but before opening the valve to measurement cell. This is important, otherwise the hydride could oxidize.

4. Characterization Methods of Metal Hydrides

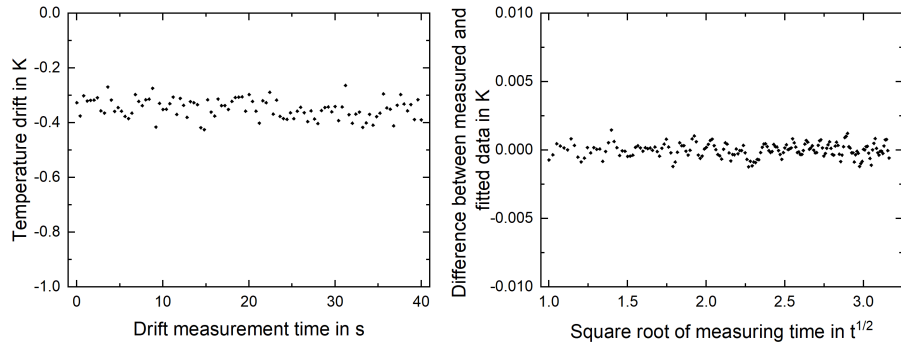


Figure 4.4.: Temperature drift measurement with the sensor prior to the transient reading has started is presented in the left plot. The right graph shows a residual plot of the transient reading. It presents the temperature difference between measured and fitted data. The fitted data are determined during the calculation step (see Chapter 4.1.1). (Values recorded to plot these graphs were recorded during the ETC measurement of dehydrogenated MgH_2 at 1 bar hydrogen)

without a risk of damaging the sensor. Additionally, it is important, that the sensor size matters while choosing the output power. A small sensor needs a small output power and a large sensor allows a higher heating power. It is recommended to measure the thermal conductivity with a temperature increase of 2-5 K [94].

After all the parameters have been set in order to enable a satisfying thermal conductivity measurement, the determination of the thermo-physical properties can be started. The measurement procedure consists of three parts. The first step is the temperature drift measurement, which is important because any temperature drift during the measurement should be avoided to achieve the best possible results. It is highly recommended to perform it prior to each transient reading, to guarantee a stable sample temperature. The temperature drift is recorded for forty seconds and shall give evidence whether a thermal equilibrium is reached. Figure 4.4 presents randomly distributed data points around a horizontal line, which gives evidence for thermal stability prior to the transient reading is started. It is possible to compensate the temperature drift during the subsequent evaluation step, but it rather is recommended to repeat such experiments [101].

The second part is the transient reading, in which an electrical current is applied to the sensor in order to stimulate a little thermal unbalance to determine the response of the sample, as shown in Figure 4.2 and explained in Chapter 4.1.1.

Finally, the measured temperature increase is used for evaluation to calculate the thermal conductivity, as presented in Chapter 4.1.1. During the transient measurement time t , 200 equidistant readings of the electrical resistance of the

4.2. Structural and morphological characterization

sensor are recorded (see (Figure 4.2)). For the calculation of the thermophysical properties, at least 100 data points must be chosen to guarantee a trustworthy calculation. By cutting off the first approximately 20 data points, any influence of the sensor's insulation and the interface to the powder bed can be skipped. If necessary, data points that were recorded at the end of the measurement must be removed to avoid any influence of the outer boundary of the sample bed.

Some criteria help to achieve and verify reliable and trustworthy results. As mentioned above, the temperature increase during the transient reading should be within 2-5 K⁴. If the output power of the sensor is too little, the temperature increase might be overruled by thermal fluctuations in the sample. If, on the other hand, the heating power is too high, the sensor could be damaged by local overheating within the sensor.

Since the thermal diffusivity and thus the thermal conductivity is determined by a fitting procedure in which a linear function between the temperature increase and the dimensionless time-dependent function $D(\tau)$ is obtained (see chapter 4.1.1), the fitting mean deviation is used as a parameter, to verify to the accuracy of the measurement. The right plot in Figure 4.4 presents the difference between measured and fitted data points. A homogeneous distribution in the range of a few hundred μ K for data points along a horizontal line as shown here verifies trustworthy results.

For each ETC value at least three readings were carried out to consider the mean value of these single measured values. Between every single measurement, there is a waiting time of at least three minutes to guarantee the stability of the measurement.

4.2. Structural and morphological characterization

For the analysis of the morphological and structural properties of the magnesium hydride MgH_2 , the nickel activated magnesium hydride MgH_2 - Ni and the magnesium iron hydride Mg_2FeH_2 , X-Ray Diffraction (XRD) and Scanning Electron Spectroscopy (SEM) were performed.

XRD analysis was performed in a Powder Diffraction System by STOE with a molybdenum source (0.7093 Å) and operated in transmission mode. The sample

⁴For measuring the ETC of MgH_2 powdered beds in this work the output power is set in the range of 50 mW to 200 mW. Measurement time is in the range of 2 - 10 s.

4. Characterization Methods of Metal Hydrides

preparation was carried out in a glove box under an argon atmosphere to avoid any contamination and oxidation. The powder sample materials were placed in glass capillaries with a diameter of 0.5 mm. The glass capillary was sealed with vacuum grease before transferring it to air atmosphere. For permanent sealing, the top part of the glass capillary, in which no powder is present, was molten by usage of a flame torch.

For the analysis of the crystalline phases in the samples, respective XRD patterns were analyzed by Rietveld refinement. The results are presented with an accuracy of ± 1 mass – %.

SEM micrographs for overview purposes were taken in the TM3030, a tabletop electron microscope by Hitachi. For the sample preparation, the powder had to be exposed to air. This did not cause any troubles since the investigated material appeared to be inactive under air atmosphere.

For a detailed investigation of the nickel activated magnesium hydride powder, a scanning electron microscope SU3500 by Hitachi is used. Images of the samples are taken at 1000 x magnification to obtain an overview of the particles and its morphological properties. Energy-Dispersive X-Ray Spectroscopy (EDX) was applied to perform elemental analysis of the samples at the SU3500, equipped with a Si(Li) Pentafet Plus EDX-detector.

4.3. Chemical, compositional and thermo-gravimetric investigation

One of the most important analytical methods when working on metal hydrides is the Thermogravimetric Analysis (TGA). The thermogravimetric measurement of the metal hydrides was performed by using the TGA/DSC Star System from Mettler Toledo. In this method, a few milligrams of the metal hydride are placed in 40 μ l aluminum crucibles. This preparation takes place under argon atmosphere to avoid any oxidation which would falsify the results. The crucibles are closed with a cap and mechanically sealed. Right before placing the crucible in the TGA measurement system, a small hole is made into the cap, thus the released hydrogen, from the metal hydride, can escape from the crucible. By heating the sample and reaching the decomposition temperature of the respective metal hydride, the respective weight loss is measured by a precision balance [103]. The heating rate

4.3. *Chemical, compositional and thermo-gravimetical investigation*

was set to 10 K/min in the temperature range of 30 °C to 500 °C under an argon flow of 50 ml/min.

The above mentioned high resolution scanning electron microscopes are each equipped with an EDX sensor, which allows a quantitative analysis of the elemental composition⁵. Using both techniques for the sample of the nickel activated magnesium hydride consequences in the advantage that results can be compared and verified.

⁵The detection of hydrogen is not possible with EDX.

5. Development of the Measurement Autoclaves and Design of the Experiments

Aim of this work was the investigation of the effective thermal conductivity (ETC) of the materials under hydrogen gas pressure (up to 100 bar) and at elevated temperatures (up to 550 °C), to simulate the operating conditions. The materials of interest were present in powder form, which is the most promising approach for an up-scaled application. In order to perform ETC measurements, TPS sensors (Chapter 4.1.1) were used. To facilitate the ETC measurements, TPS sensors were attached in internally developed measurement autoclaves. In order to carry out the experiments, the powder material was placed in the measurement autoclave, embedding the TPS sensor. The measurements were performed at selected parameters (gas pressure and sample temperature).

Three different high-pressure vessels have been developed in order to enable thermal conductivity measurements of high-temperature metal hydrides, as MgH_2 and Mg_2FeH_2 . The first measurement vessel is constructed to withstand temperatures up to 100 °C and hydrogen gas pressure of up to 120 bar and is presented in Figure 5.3 in Chapter 5.2. The 2nd and 3rd high-pressure autoclaves were developed for experiments at temperatures of up to 550 °C and gas pressure of 100 bar. Pictures of the 2nd generation and 3rd generation measurement autoclaves are presented in Figure 5.5 in Chapter 5.3 and Figure 5.7 and 5.10 in Chapter 5.4, respectively.

The measurement autoclaves were attached to a test rig, in order to provide a gas connection, via valve V5. (Figure 5.1). In this figure two parts are recognizable; the grey part is located in the safety box. The white part is located outside of this box. The TPS sensor in the measurement autoclave is connected to the *TPS 2500S Thermal Constant Analyzer*, for data acquisition. The constant TPS system is connected to a computer, outside the safety box, in order to record the data.

5. Autoclaves Development and Experiment Design

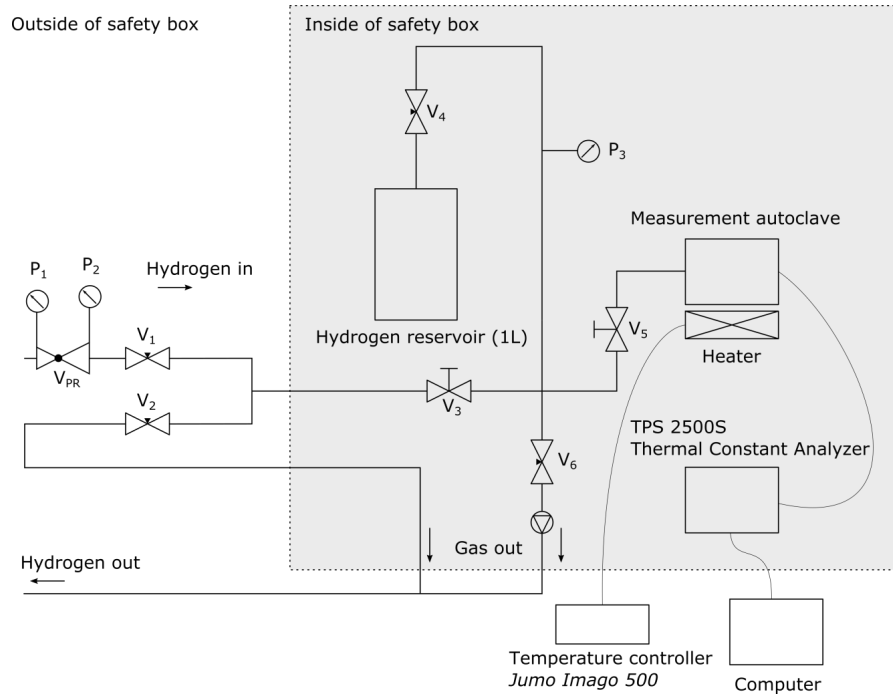


Figure 5.1.: Simplified flow sheet of test rig.

The measurement autoclave is equipped with a furnace¹ to heat the sample. The temperature is controlled with the *Jumo Imago 500*, with the help of two K-type thermocouples, which are reading the temperature of the furnace and the sample.. In principle, there is pressure regulator V_{PR} ² and two needle valves V_1 and V_2 are located outside of the box as well, which allows regulating the gas pressure inside of the test rig and the measurement autoclaves. The gas pressure is measured by a pressure transducer P_3 and is displayed and recorded by the *Jumo Imago 500*, which is located outside of the box. With the help of V_{PR} , V_1 , V_2 , and P_3 the pressure can be controlled and regulated in the test rig and the measurement autoclave. In order to guarantee an oxygen-free atmosphere for the ETC measurements, a gas purging program has to be executed after attaching the measurement autoclave to the test rig. Before opening the valve V_5 the residual gas in the test rig is removed by usage of a vacuum pump which is connected through the valve V_6 . After the gas is removed and the gas pressure is kept below 1×10^{-2} mbar for a couple of minutes the valve V_6 is closed and hydrogen gas is introduced to the rig via V_{PR} and V_1 (V_2 is normally closed and V_3 normally opened) until a

¹The first generation measurement autoclave is equipped with a resistive heater, the second and third generation autoclave with IR heater.

²The two pressure transducers P_1 and P_2 , which are attached to V_{PR} , are there to read the gas pressure in the gas supply system and the reduced pressure in the test rig, respectively. It is supposed to support the pressure control.

stable pressure of 5-10 bar is achieved. This gas is subsequently released through the valve V_2 in order to ensure atmospheric pressure in the test rig before opening valve V_6 again for the second gas removal step. These process steps are repeated two more times before V_5 can be opened³. This whole procedure of gas exchange will be again repeated 3 more times to remove residual argon gas from the measurement autoclave which has been introduced to it during the sample preparation in the glovebox (see Chapter 6). For adding gas to the test rig during the experiments, V_1 will be opened and the pressure will be regulated by V_{PR} and S_3 . If the pressure has to be reduced in the measurement autoclave the valve V_2 will be used for gas release.

An additional feature of this test rig is a hydrogen gas reservoir with a volume of 1000 cm³. It is connected through valve V_4 and serves as a hydrogen gas reservoir during the dehydrogenation step, in which the hydrogen is released from the metal hydrides. It enables long term hydrogenation and dehydrogenation cycle tests (Chapter 6.8). To avoid day and night temperature fluctuations of the stored hydrogen gas, this reservoir is equipped with a resistive heater to keep the gas at a constant temperature of 30 °C.

The gas outlets are connected to the gas exhaust of the safety box which leads the used hydrogen to the roof of the box where the hydrogen can vanish to the air.

5.1. Safety aspects

The biggest challenge is to design, construct and finally to run these high-pressure vessels, in which the extremely volatile hydrogen gas is not leaking through any sealing and connections. This is necessary for hazard reasons. At 4–75 vol – % of hydrogen in air, the gas composition is burnable. Above 18 vol – % it is explosive and at temperatures of 500–585 °C self-igniting [104].

In order to enable to work in a safe environment, the experiments had been performed in a safety box in the high-pressure facility in the Max-Planck-Institut für Kohlenforschung (Figure 5.2).

This box allows that high temperature and high gas pressure experiments can be realized, without putting the experimenter into a hazardous situation. The test rig and the *TPS 2500S Thermal Constants Analyzers* by *Hot Disk AB* can be seen

³A approximation of the residual amount of oxygen after the purging is presented in the Appendix A 13.

5. Autoclaves Development and Experiment Design

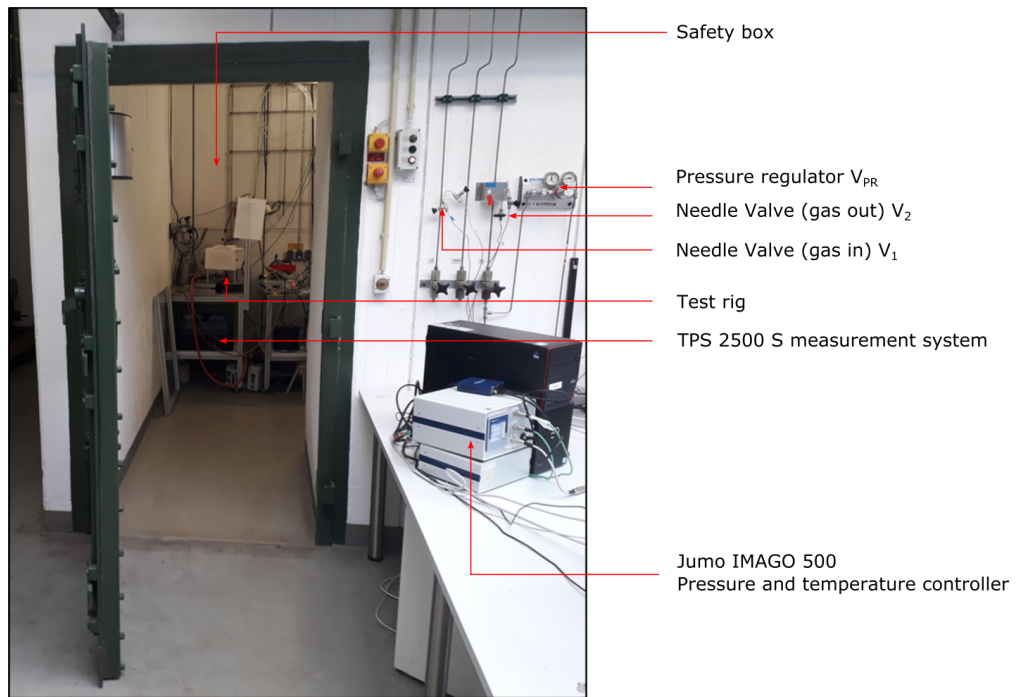


Figure 5.2.: Safety box, which is located in the high-pressure lab of the Max-Planck-Institut für Kohlenforschung.

inside the box. For pressure and temperature control, a *Jumo Imago 500* is placed outside of the safety box. The pressure regulator and valves are attached to the wall and connect the test grid with the hydrogen gas source of this facility.

5.2. Development of the 1. generation measurement autoclave

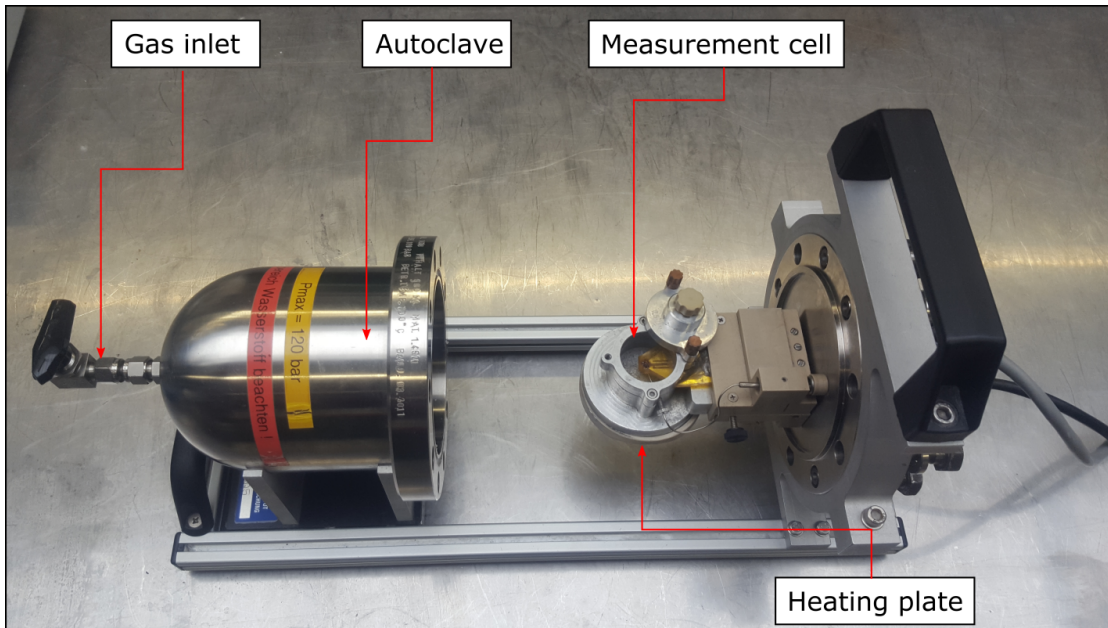


Figure 5.3.: Measurement autoclave of 1st Generation.

5.2. Development of the 1. generation measurement autoclave

The first-generation measurement autoclave is displayed in Figure 5.3. It is designed for gas pressures up to 120 bar and temperatures of up to 100 °C. It is made of 1.4571 steel, an austenitic alloy to withstand relatively high gas pressures (see Table 5.1). Even though the construction steel withstands much higher temperatures, the operating temperature is limited by the PEEK in the measurement cell. It mainly consists of two parts, the high-pressure autoclave with the attached gas inlet and the measurement cell on a plate heater (center of Figure 5.3) (see also Figure 5.4). The measurement cell is made of an aluminum alloy and is detachable to enable easier loading of powder material and cleaning process, as presented in Figure 5.4. This measurement cell is placed on a heating plate which enables heating of the sample to temperatures of up to 100 °C. The sample temperature is recorded by K-type thermocouple which is located in the measurement cell (see Figure 5.4).

The Kapton-covered sensor is fixed in the center of the measurement cell and electrically connected via copper wires in the PEEK frame. Four electrically insulated copper contacts were connected through a feedthrough to cable connections outside the pressure autoclave. The measurement cell can be disassembled which allows

5. Autoclaves Development and Experiment Design

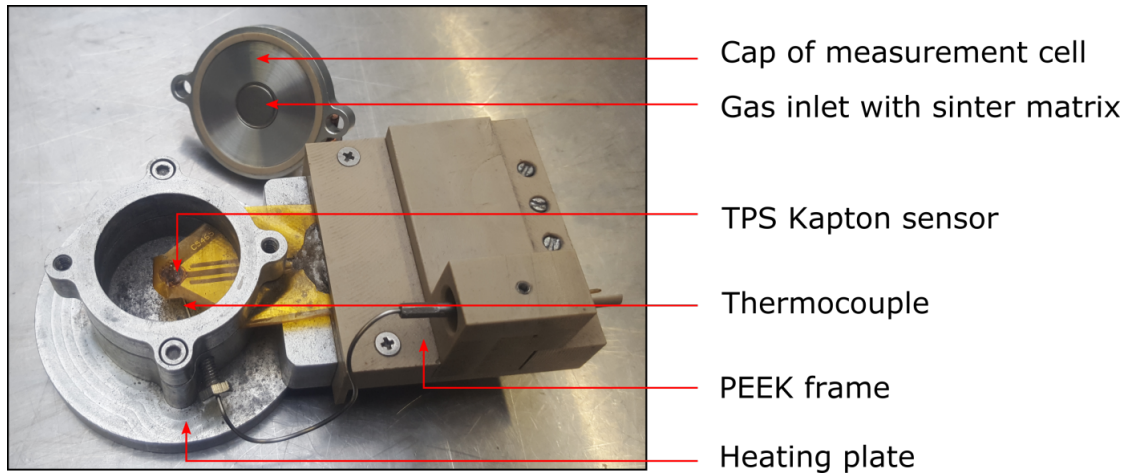


Figure 5.4.: Removable measurement cell of the 1st generation measurement autoclave with main parts: the TP sensor, the thermocouple for temperature control, the heating plate and the cap, including gas inlet and sinter matrix.

a proper cleaning of it. A sinter matrix in the cap of the measurement cell is installed to prevent powder material to penetrate the test rig due to vacuum during the gas exchange step (Figure 5.4). Further, it shall inhibit any pressure surge to the material if gas pressure changes accidentally too dramatically.

There are two issues that have to be considered while using this autoclave, which will be addressed hereafter.

The first issue is concerning the weight and the size of the autoclave as presented in Figure 5.3. The handling of this 980 cm³ autoclave is difficult, especially if the material has to be transferred into the measurement cell (Figure 5.4) under an inert atmosphere in a glovebox. For this process the autoclave has to be moved into the glovebox, which can be challenging for the experimenter.

The second issue is the large gas volume (980 cm³) of this autoclave and the location of the heater under the measurement cell. The place of the heater induces a temperature gradient from the hot lower part to the colder top part. The temperature cannot be homogeneously distributed. Since the measurement cell is located in rather large free gas volume, heating of the measurement cell will introduce heating of the surrounding gas. This will cause forced gas convection and therefore a steady temperature fluctuation in the autoclave. Additionally, the wall of the autoclave is, because of the mostly colder ambient temperature, a heat sink that has to be thermally insulated from the outside in order to avoid too large heat losses to the surrounding atmosphere. The heat loss strongly depends on the gas pressure inside of the autoclave. At high gas pressure of 100 bar, the heat loss

5.3. Development of the 2. generation measurement autoclave

is large, e.g. the temperature of the heating plate has to be as high as 180 °C, to achieve a resulting sample temperature of 100 °C. At lower pressures the heat loss is less pronounced.

To conclude: The first generation measurement autoclave enables the ETC measurements of powder beds under temperatures of up to 100 °C and gas pressures of up to 100 bar. The large volume can cause some temperature stability issues especially when running experiments under elevated temperatures and gas pressure. This causes long waiting time until a thermal equilibrium in the sample, the measurement cell and in the measurement autoclave is reached.

5.3. Development of the 2. generation measurement autoclave

The above mentioned high-pressure set-up is useful for thermal conductivity measurements at temperatures of up to 100 °C. It was used to measure the thermal conductivity of magnesium powder and of low-temperature metal hydrides (e.g. NaAlH₄), which react at temperatures below 100 °C. In this Chapter the design and the development of the high temperature (< 500 °C) and high pressure (< 100 bar) autoclave will be introduced. A picture of the measurement autoclave of the 2nd Generation is shown in Figure 5.5 (top). On the left side the gas and thermocouple connection is attached to the pressure autoclave. The sensor connection can be seen on the right side. The blue color of the steel is caused by the experienced temperature (annealing) of above 500 °C.

The material which was used for the construction of the 2nd generation measurement autoclave is 1.4980 steel. It is a steel alloy as 1.4571, which was used for the 1st generation measurement autoclave but with increased nickel content. As presented in Table 5.1. High nickel content in a steel alloy increases the toughness of the alloy, even at elevated temperatures [105, 106]. The jackscrews (M8) are made from the same steel to ensure that a mismatch caused by different thermal expansion can be avoided or at least minimized.

The high-pressure autoclave is in cylindrical shape (see c in Figure 5.5) and it is capped by two flanges on both sides (see a and f in Figure 5.5). Sealings made from gold wires are placed between the pressure autoclave and the flanges to ensure that no hydrogen leaks to the surrounding atmosphere and no other gases

5. Autoclaves Development and Experiment Design

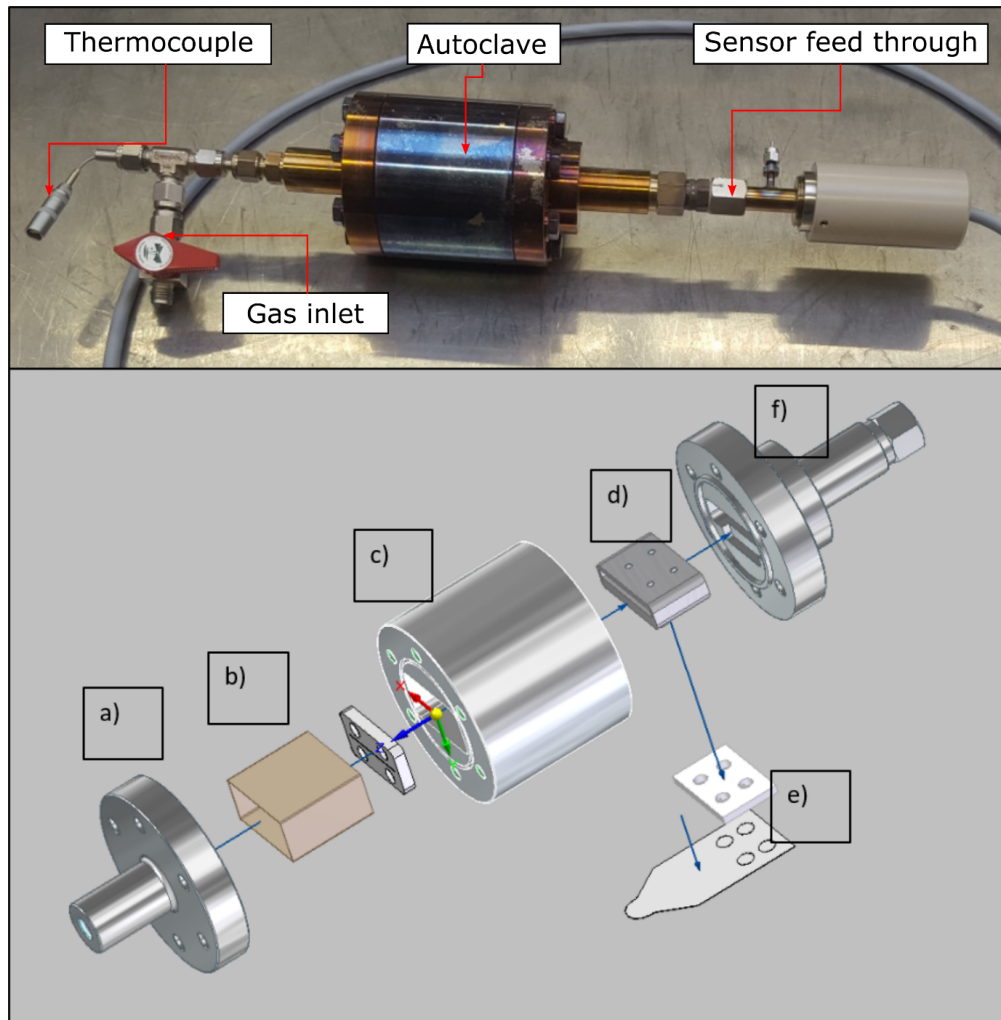


Figure 5.5.: Picture of measurement autoclave (2nd Generation) (top) and technical sketch (bottom). The main parts are the flanges a) and f), the high body of the pressure autoclave c), the inlet for the sample b), the sensor e) and its metallic holder.

Table 5.1.: Nickel and maximal operating temperature of used high temperature steel.

Material - number	Nickel content	Maximum operating temperature
1.4571	1.9 [107]	550 °C
1.4980	24.0 – 27.0 % [106]	700 °C
1.4767	0.0 – 0.3 % [108]	1200 °C

5.3. Development of the 2. generation measurement autoclave

contaminate the metal hydride in the measurement cell. The flange on the left (a in Figure 5.5) is for the gas connection and the thermocouple for measuring the sample temperature. A sheet made of 1.4767 steel is placed in front of the gas inlet, which is necessary to avoid any possible pressure surge in the measurement cell and to avoid that fine loose metal hydride particles can be released from the measurement autoclave.

The sample material is placed in an inlet (b in Figure 5.5), made from 1.4767 steel, to separate it locally from the high-pressure autoclave (c Figure 5.5), which is made from 1.4980 steel. This is necessary to prevent contact between the magnesium hydride and the autoclave material. It is important because nickel would leach from the autoclave steel into the material under the harsh conditions, under which the experiments are executed. As consequence, the nickel might be incorporated in the magnesium, which might change the properties of the sample material.

The main challenge for the construction of this autoclave is the electrical connection of the sensor. It is necessary to realize an electrical contact of four leads from inside of the measurement autoclave to the outside which must be hydrogen gas-tight, even at elevated temperatures and gas pressures.

Therefore, the very unique feature of the measurement autoclave can be seen on the right side in Figure 5.5. It is the electrical connection from the Mica-coated sensor (see Chapter 4.1.1), which is embedded inside of the high-pressure and high-temperature measurement cell, to ambient pressure and temperature, outside the set-up. Therefore, a metallic sensor holder (d in Figure 5.5) is installed which connects the sensor with four gold leads to the flange (f in Figure 5.5). A ceramic insert ensures electrical insulation of the wires and the connection to the sensor (e in Figure 5.5). The gold wires are insulated with ceramic parts, which lead to a high-pressure feed through by Spectite[®]. The main part of this feedthrough is a piece of magnesium silicate (Lava) with four cable routes for the gold wires (see Figure A.3). During the tightening, this piece of Lava is crushed into fine powder and compacted to ensure a hydrogen-pressure-tight connection. This feedthrough cannot be opened again and it is not reusable. The four electrical contacts are connected to a cable that connects the sensor finally to the measurement device.

The measurement autoclave is placed in a furnace consisting of four infrared heaters with each of them having an output power of 250 W (see Figure 5.6). The autoclave is thermally insulated by a casing made from calcium silicate boards,

5. Autoclaves Development and Experiment Design

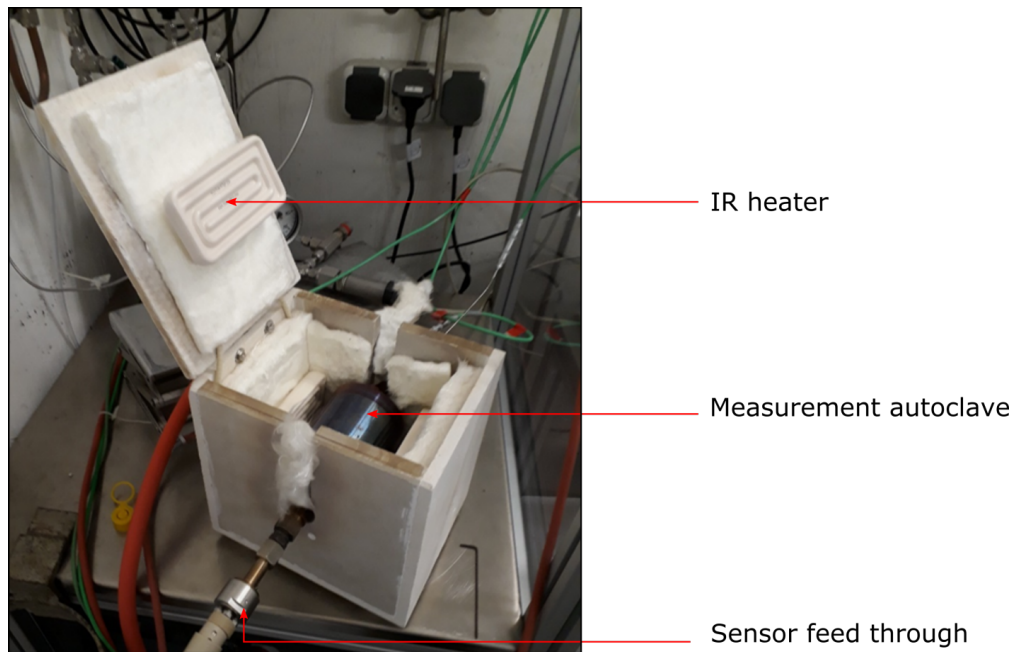


Figure 5.6.: 2nd Generation measurement autoclave, placed in the infra-red furnace.

called Monolux^{®4}, to reduce influences by temperature fluctuation in the environment and general heat loss to the surrounding. Any fluctuation in the furnace chamber, might not be inhibited, but has not been measured.

5.4. Development of the 3. generation measurement autoclave

The measurement cell described in Chapter 5.3 enables measurement of the thermal conductivity of high temperature and high-pressure metal hydrides as magnesium hydride. There were two issues that had to be improved. Thus a third measurement autoclave has been developed to overcome some drawbacks from the 2nd Generation measurement cell. The first of the drawbacks is the fact that the sensor cannot be exchanged without breaking the feedthrough. The whole sensor connection has to be replaced when the sensor is broken, inclusive of the gold wires, as the sensor can easily delaminate after removing powder metal hydride. Therefore, the sensor holder (Figure 5.7) is attached to the flange (f) which allows that the sensor can be easily exchanged just after disassembling the pressure vessel from the flange (f).

⁴Material contains of: 49 % SiO₂, 48 % CaO and 1.2 % Fe₂O₃.

5.4. Development of the 3. generation measurement autoclave

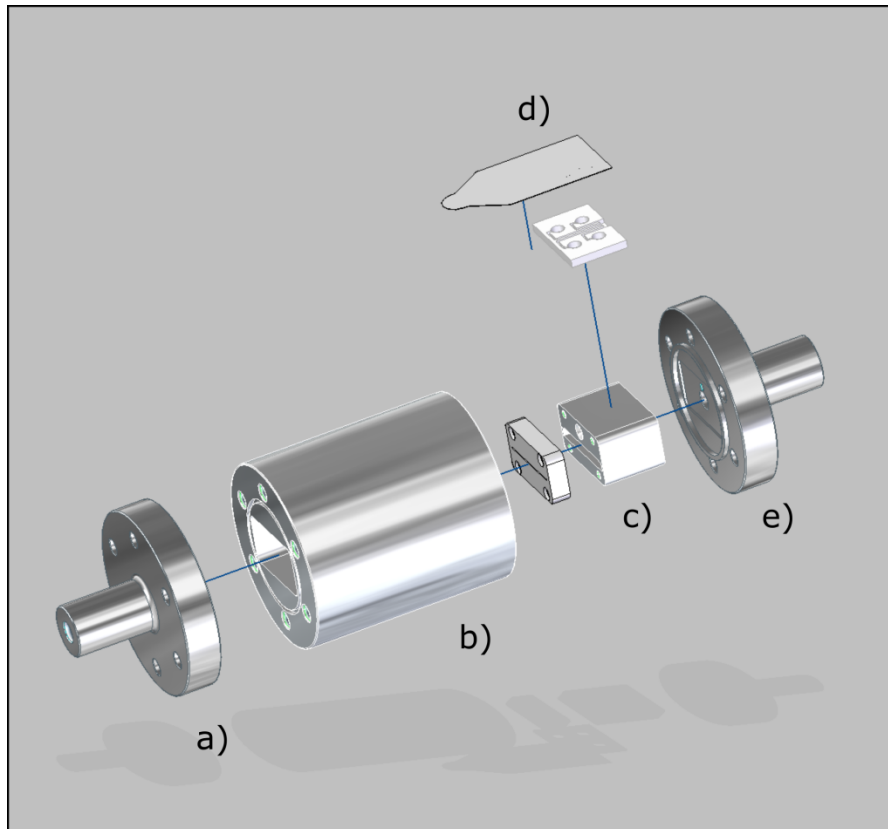


Figure 5.7.: Technical sketch of 3rd Generation measurement autoclave. The main parts are the flanges a) and e), the body of the high pressure autoclave b), the sensor d) and its holder c).

The construction and assembling of the 3rd generation measurement autoclave are identical to the measurement autoclaves of the 2nd generation, except for the improved sensor connection and an increased sample volume of 44.37 cm³ (compared to 30.24 cm³, Table A.5). It has the main parts as the two flanges (a and e in Figure 5.7), which close the body of the measurement autoclave (b in Figure 5.7) from both sides and an inlet for the test material.

Detailed sketches of both measurement autoclaves are presented in Figure 5.8, in which the main parts of the measurement autoclaves are named in the legend. The above-mentioned main difference of both autoclaves is the sensor holder, which is illustrated by point 5) in Figure 5.8. In the 2nd generation measurement autoclave it is part of the body of the high-pressure vessel 2) and electrically attached to the flange 6). For removing the sensor, the sensor holder can not be removed from the pressure vessel thus the electrical connection, which leads through the flange 6), has to be disassembled. The electrical connection has to be renewed for replacing the sensor. In the 3rd generation measurement autoclave, the sensor holder 5) is

5. Autoclaves Development and Experiment Design

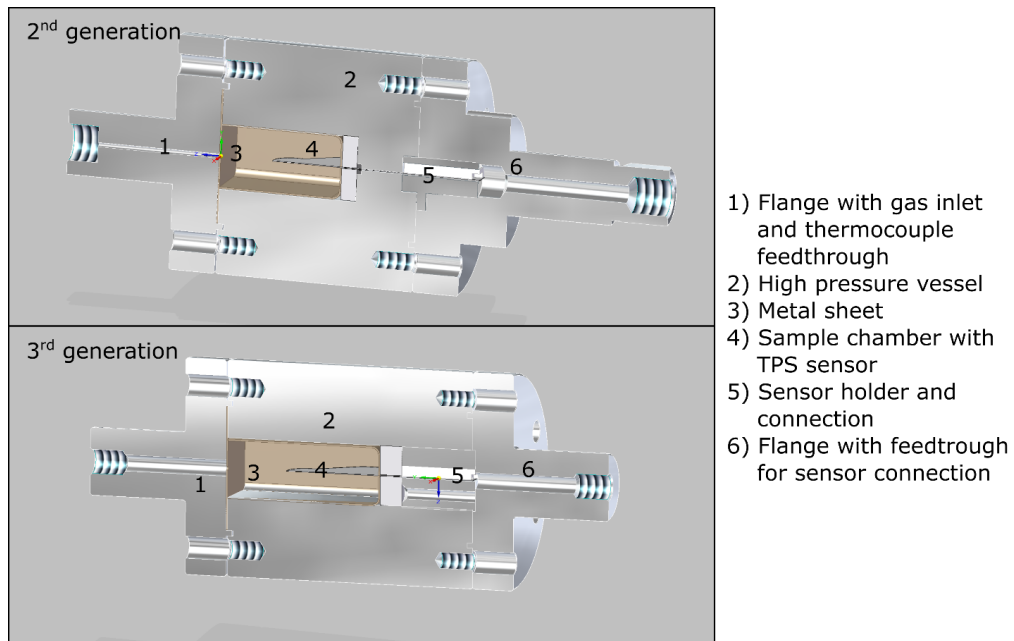


Figure 5.8.: Schematic sketch of the measurement autoclave of the 2nd and 3rd generation.

attached to the flange 6). For changing the sensor, the flange 6), inclusive of the sensor holder, can be separated from the pressure vessel 2) in order to remove the sensor from the sensor holder 5) without destroying the electrical connection in 6).

The second improvement is considering the positioning of the measurement autoclave and the layout of the furnace. The 2nd Generation autoclave is placed horizontally in a furnace, as shown in the left picture of Figure 5.9, which might lead to an uneven packing of the powder sample on the top and on the bottom of the sensor. This might be the case, especially during the time when the metal hydride is dehydrogenated and the particles contracted. It is possible that some voids might be formed in areas under the sensor (see (c) in Figure 5.9) and that the powder on the top side of the sensor experiences a densification (see (a) in Figure 5.9) and thus a higher contact pressure to the sensor than the powder below the sensor, which might have a less dense packing and thus a worse thermal contact. This might have an influence on the measured result.

The 3rd Generation measurement autoclave is positioned vertically in order to have identical packing on both sides of the sensor (see Figure 5.9 (right) and Figure 5.10) to ensure an identical thermal contact between the sensor and metal hydride powder on both sides. The gas inlet is attached on the bottom part and the sensor feedthrough can be found on the top side of the furnace.

5.4. Development of the 3. generation measurement autoclave

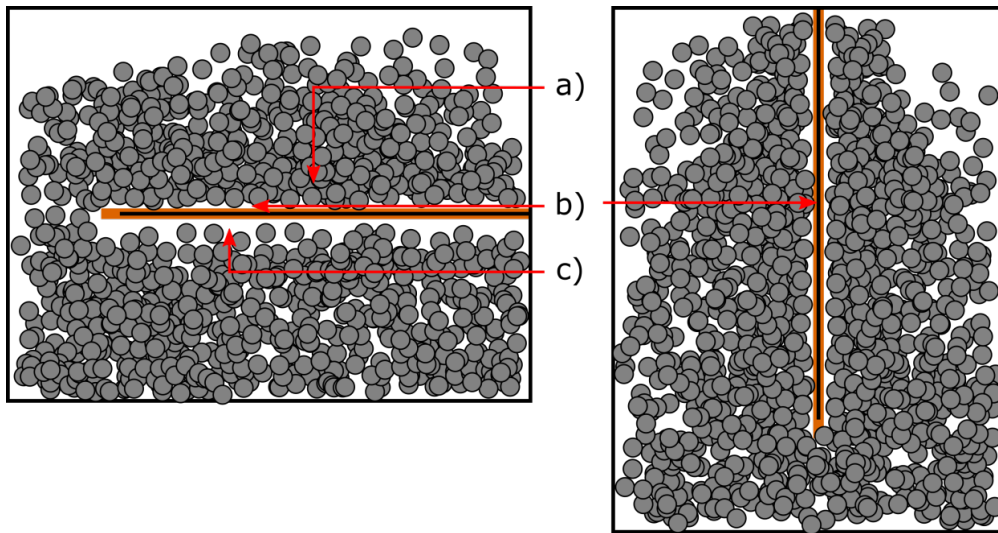


Figure 5.9.: Illustration of metal hydride particle distribution around the sensor (b) in the 2nd Generation measurement autoclave (left) and 3rd Generation measurement autoclave. Horizontal positioning (in the left) of the sensor can cause densified areas above the sensor (a) and less dense areas below the sensor (c).

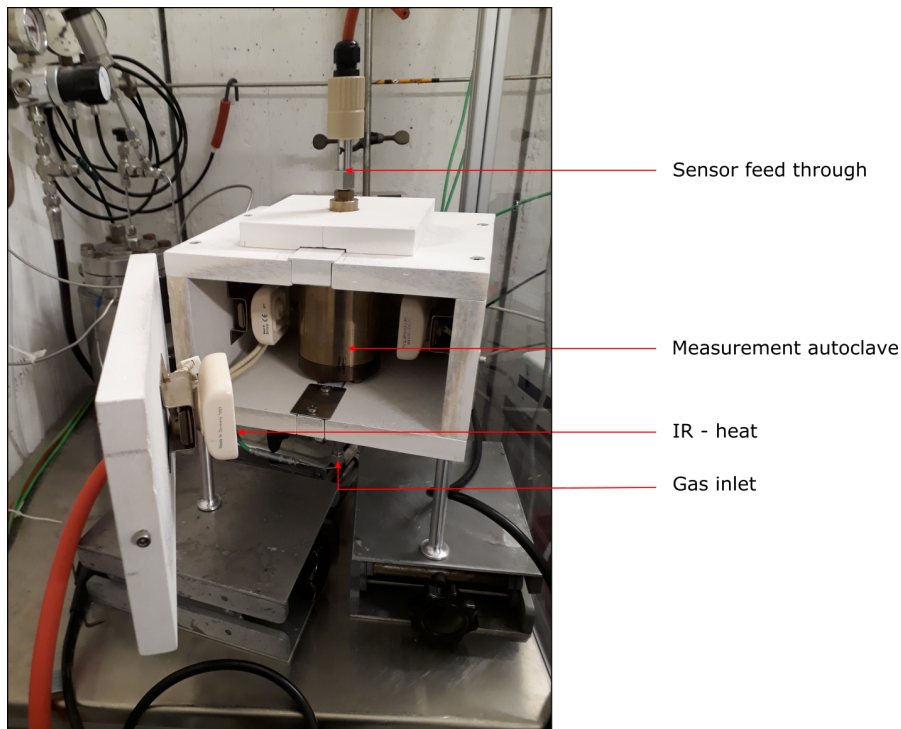


Figure 5.10.: 3rd Generation measurement autoclave in IR-heater furnace.

6. Results and Discussion

Table 6.1 gives an overview of the samples in which results of the thermal conductivity measurements are presented in this work. It shortly mentions the temperature and gas pressure range under which these investigations were performed.

The magnesium was purchased either from *Sigma Aldrich* and has a particle size of $< 297 \mu\text{m}$ or from *Alfa Aeser* with a particle size of $< 45 \mu\text{m}$. Both materials were used for ETC measurements, to investigate the influence of the particle size and the packing density on the heat transfer in packed beds. The magnesium powder of smaller particle size was additionally used for the synthesis of the nickel catalyzed magnesium hydride. During the measurement, the gas pressure range was 1-100 bar because this is the operating pressure range of common high-temperature metal hydrides. The temperature range of 25-100 °C was defined by the maximum operating temperature of the first-generation measurement autoclave of 100 °C.

The thermal conductivity of magnesium hydride (MgH_2), received from *Sigma Aldrich*, was investigated because it is well-understood metal hydride, which has the potential to be used in up-scaled applications in the near future. It serves as a model system, which is simpler than the other investigated metal hydrides because it has no catalysts added.

The nickel-activated magnesium hydride (MgH_2 4 mass – % Ni) was prepared by mixing of magnesium powder ($< 45 \mu\text{m}$) and nickel powder ($< 1 \mu\text{m}$) under air with subsequent heating under hydrogen atmosphere. This material is a potential candidate for up-scaled energy storage systems at temperatures of up to 400-420 °C.

Magnesium iron hydride (Mg_2FeH_2) was prepared by mixing and stirring of magnesium powder and iron powder ($< 45 \mu\text{m}$) with subsequent hydrogenation and dehydrogenation reactions at temperatures of 470 and 550 °C. The pressure range is between 91 and 101 bar for the hydrogenation and dehydrogenation reactions, respectively. This high-temperature metal hydride is promising energy storage material for applications at temperatures of up to 550 °C.

6. Results and Discussion

Table 6.1.: Overview of metal hydride samples of which the effective thermal conductivity was measured in this work.

		Maximal particle size and purity of starting material	Measurements conditions	
			temperature	pressure
Mg powder	as purchased	< 297 μm (99 %) < 45 μm (99.8 %)	25 °C-100 °C	1-100 bar
MgH ₂	as purchased	< 45 μm (99.8 %)	25 °C-410 °C	1-25 bar
MgH ₂ (4 mass – %Ni)	Prepared (51 cycles)	< 45 μm (Mg)(99.8 %) < 1 μm (Ni)(99.8 %)	25 °C-400 °C	1-25 bar
Mg ₂ FeH ₂	Prepared (21 cycles)	< 45 μm (Mg)(99.8 %) < 45 μm (Fe)(97 %)	25 °C-520 °C	1-100 bar

6.1. Synthesis of nickel activated MgH₂ and Mg₂FeH₆

This Chapter provides information about the synthesis of the nickel activated magnesium hydride (chapter 6.4 and 6.8.1) and the magnesium iron hydride, which were used in the experiments of the thermal conductivity measurements (chapter 6.5 and 6.8.1).

6.1.1. Set-up and preparation of the synthesis

The preparation of MgH₂ (4 mass – %) and Mg₂FeH₂ was performed by mixing of metal powders under air, before each of these mixtures was transferred into an autoclave. The charging of the autoclaves with a mixture of magnesium and the additives proceeds under air since the material shall represent realistic preparation conditions that will be used in up-scaled applications. To determine the precise weight of the precursor material a scale (*SI 234, Denver Instruments*, accuracy: 0.1 mg) was used. Furthermore, a precise mass determination of the activating agent content (nickel content) could be guaranteed. The 36 ml autoclave is made of 1.4980 steel (alloy 286) and withstands elevated gas pressures up to 250 bar at temperatures up to 700 °C (see Table 5.1). The assembled autoclave is authorized to operate at temperatures of up to 550 °C. The metal powder is not in direct contact to the autoclave, it is placed in a construction steel (1.0029) inlet, which does not contain nickel. This is important since investigations at our institute

6.1. Synthesis of nickel activated MgH_2 and Mg_2FeH_6

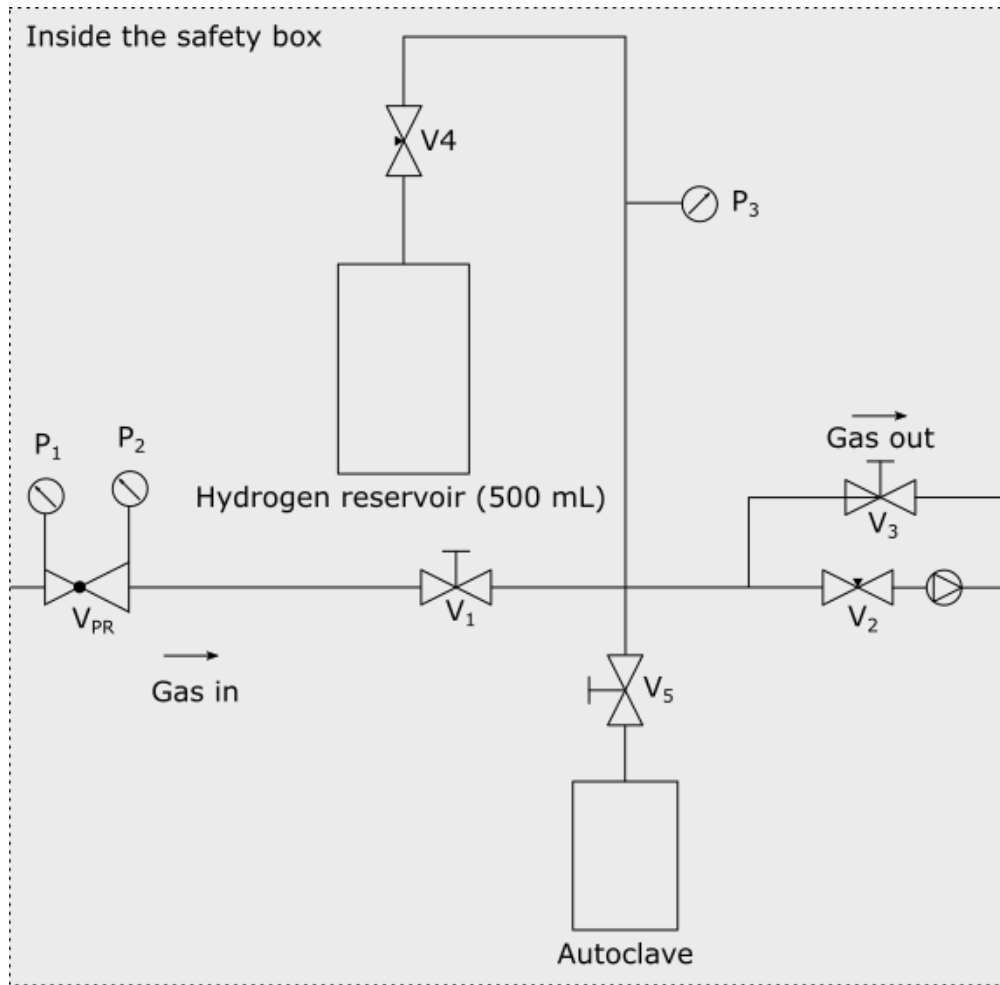


Figure 6.1.: Test rig for the synthesis of the magnesium-based metal hydrides, in this work.

showed that nickel from the wall of the vessel is leached out into the magnesium at high temperatures. This was already part of the investigations by Schlichte et al. [109]. Leached nickel increases the nickel content and changes the thermodynamic properties of the product and the autoclave steel experience corrosion. Once the inlet with metal powder was placed in the autoclave, the vessel was closed with a flange and six M6 screws made from 1.4980 steel. All parts of the autoclave, the vessel, the flange, and the screws are made of the same material to avoid problems due to different heat expansion coefficients of different alloys caused by elevated temperatures during the synthesis. The autoclave was placed in a furnace and connected to the synthesis test rig (see Figure 6.1) which is located in a safety pressure cabinet in the high-pressure lab of the Max-Planck-Institute für Kohlenforschung.

After the autoclave was connected through the opened valve V_5 to the test rig,

6. Results and Discussion

hydrogen gas was introduced to test rig via the gas inlet valve V_1 and the pressure reducer V_{PR}^1 until a pressure of 5–10 bar was achieved, which was recorded by the pressure transducer P_3 . Subsequently, the hydrogen gas was released by opening V_3 to reach atmospheric pressure (V_{PR} and V_1 are closed). V_3 has closed again and a rotary pump was reducing the gas pressure in the test grid to approximately 1×10^{-2} mbar, while V_2 was opened. After closing V_2 , this purging procedure had been repeated two times. Subsequently, to these steps, the autoclave is heated to approximately 250 °C and V_2 was opened in order to bake out the sample under vacuum condition for 2 hours. The last step was performed in order to remove residual adsorbed gas molecules from the metal powder.

6.1.2. Equilibrium pressure curve for the formation of MgH_2 and Mg_2FeH_6

After the test rig and the autoclave were purged the synthesis could be started by the first hydrogenation. This first hydrogenation of the metal powder mixtures was initiated by increasing the hydrogen pressure above the equilibrium pressure curve of respective metal hydride (Figure 6.2) for 24 hours. The process parameter for the synthesis of the nickel activated MgH_2 and Mg_2FeH_2 are presented in chapters 6.1.2 and 6.1.3, respectively.

Figure 6.2 displays the equilibrium pressure curve for the formation of Mg_2FeH_2 and MgH_2 (4 mass – % Ni) as a function of the temperature. Even though nickel activated magnesium hydride has been synthesized, from the thermodynamic perspective it is considered as pure magnesium hydride. This assumption is vindicated because 4 mass – % of nickel has been added to the magnesium, therefore it is presumed that it acts as catalyst. For defining the synthesis parameters during the synthesis the temperature-specific plateau pressures of magnesium hydride and magnesium iron hydride, determined by using the Van't Hoff plot (see Chapter 2) from [110], was applied to plot the equilibrium pressure curves as function of the temperature in Figure 6.2. A metal hydride is formed when the hydrogen pressure p_{H_2} is exceeding the respective equilibrium pressure p_{eq} . If the hydrogen pressure is lower than the equilibrium pressure, the metal hydride decomposes into the respective metal and hydrogen.

Experiments in our institute showed that the reaction towards the binary mag-

¹The manometer P_1 and P_2 are installed to read the hydrogen pressure in the gas supply network and the gas pressure which is in the test rig, respectively.

6.1. Synthesis of nickel activated MgH_2 and Mg_2FeH_6

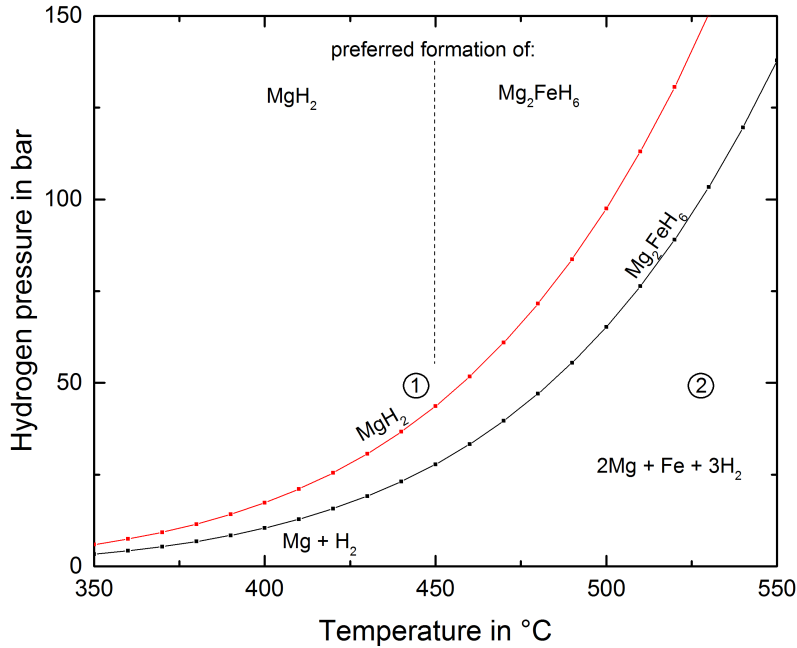


Figure 6.2.: Equilibrium pressure curve of MgH_2 (red curve) and Mg_2FeH_6 (black curve).

nesium hydride² occurs at temperatures above 350 °C. Ternary magnesium iron hydride is preferred to be formed at temperatures above 450 °C.

6.1.3. Calculation of hydrogen mass content in metal hydrides

For the calculation of the absorbed hydrogen in the metal hydrides, the pressure differences after dehydrogenation and hydrogenation are compared. Using the ideal gas law (see the following equation), the mass content of the hydrogen in the magnesium hydride is calculated.

$$\Delta n = \frac{\Delta p V}{RT} \quad (6.1)$$

T is the gas temperature, R the ideal gas constant, V the estimated volume of the overall closed system (including the gas lines) and p the determined pressure difference. In this equation, n represents the amount of hydrogen in mol, which is released during the dehydrogenation reaction. The temperature of 313.15 K in the

²Assumption: The amount of nickel is small in the sample and thus acts as a catalyst which does not change the thermodynamic properties of the magnesium hydride.

6. Results and Discussion

hydrogen reservoir is considered for this equation since most of the gas is located in it. The volume V of the test rig (including the hydrogen reservoir and the measurement autoclave) is 594 ml and the ideal gas constant is $8.314 \text{ J mol}^{-1} \text{ K}^{-1}$. For this estimation, no compressibility factor for non-ideal gases is considered (see Chapter 3.1).

Once the amount of released hydrogen is calculated, the mass content of hydrogen in the metal hydride $m\%$ can be calculated by using the two following equations:

$$m_{\text{H}} = n \cdot M \quad (6.2)$$

and

$$m\% = \frac{m_{\text{H}}}{m_{\text{MeH}}} \quad (6.3)$$

The molar mass of hydrogen is represented with M , the mass of hydrogen with m_{H} and the mass of the metal hydride with m_{MeH} .

6.1.4. Synthesis of nickel activated MgH_2

The synthesis was performed by mixing 9.16 g (0.38 mol) magnesium powder of $< 45 \mu\text{m}$ particle size (*Alfa Aesar*) with 0.38 g (0.005 mol) nickel powder (*Sigma-Aldrich* now *Merck*) of particle size of $< 1 \mu\text{m}$ and a purity of 99.8% (see Table 6.1). This results in a mass fraction of 3.9 mass – % nickel in the magnesium nickel powder mixture, which is close to the value which is given in the literature [46]. The powder mixture was then inserted in an autoclave, as described in chapter 6.1.1. After closing and sealing the autoclave and connecting it with the gas reservoir the system was evacuated and purged with hydrogen for three times (see Figure 6.1 and Chapter 6.1.1).

At first, the magnesium nickel powder was exposed to $355 \text{ }^\circ\text{C}$ at 27 bar of hydrogen for 24 hours to initiate the first hydrogenation of the magnesium powder. After that, a temperature program was started, which is presented in Table 6.2. This temperature-controlled program consists of four steps. In the first two steps, the magnesium hydride is dehydrogenated by the increase of the temperature from $355 \text{ }^\circ\text{C}$ to $420 \text{ }^\circ\text{C}$ with a heating rate of 5 K/min . The temperature is kept constant at $420 \text{ }^\circ\text{C}$ for 2 hours to guarantee a full decomposition of the magnesium hydride. In the third step, the hydrogenation is initiated by a reduction of the temperature

6.1. Synthesis of nickel activated MgH_2 and Mg_2FeH_6

Table 6.2.: One cycle of the temperature-controlled program for the synthesis of the nickel activated magnesium hydride.

step number		Temperature in °C	Time in h:min:sec	Temperature ramp in K/ min
1	Dehydrogenation	350–420	00:14:00	5
2	Dehydrogenation	420	02:00:00	-
3	Hydrogenation	420–350	00:14:00	5
4	Hydrogenation	350	02:00:00	-

to 350 °C, with a cooling rate of 5 K/ min. The temperature is kept constant at 350 °C for 2 hours to ensure full hydrogenation of the material. These four steps were repeated for 50 times, beginning with the dehydrogenation step, in order to accomplish 51 cycles of H_2 discharging and charging.

The gas pressure has been recorded during the synthesis, which allows calculating the absorbed hydrogen content in the nickel activated magnesium hydride, as mentioned above. The left plot in Figure 6.3 shows the hydrogen pressure in the autoclave as a function of the synthesis time. With the help of the pressure recordings the absorbed hydrogen content in the magnesium hydride can be estimated, subsequently. The results of the determined hydrogen amount in the sample during the first 51 cycles are presented in the right plot of Figure 6.3.

As depicted in the left plot of Figure 6.3, the gas pressure decreases in the autoclave vessel during the first hydrogenation. This is caused by the uptake of the hydrogen atoms during this step. The reaching of a stable gas pressure of 12 bar after

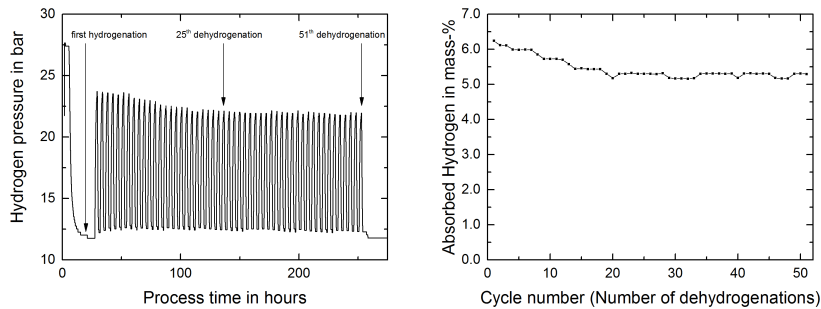


Figure 6.3.: Hydrogen pressure of nickel activated magnesium hydride during the synthesis via 51 cycles of de-/hydrogenation (left) and the calculated hydrogen mass fraction in the nickel activated magnesium hydride as a function of the cycle number in (right).

6. Results and Discussion

24 hours, which is approximately 6.7 bar higher than the equilibrium pressure, indicates the complete hydrogenation of the magnesium powder.

The second feature, observable in the left plot, is the decreasing gas pressure, which is released during the dehydrogenation steps. A reduction in pressure equals a reduced mass fraction in the magnesium hydride, which is released after dehydrogenation. This phenomenon is attributed to particle sintering of the magnesium particles during the dehydrogenation steps. Especially, nickel acts as an activator for the sintering of the magnesium particles [18, 46]. A hydrogen leakage, as possible source for a reducing hydrogen pressure, can be excluded, because the gas pressure after each hydrogenation step is at about 12.5 bar over the 51 cycles (right plot in Figure 6.3). This indicates an absence of any leakages in the system.

After running the synthesis for 257 hours, the autoclave was cooled down with the material inside, being in the hydrogenated state. The removed magnesium hydride has a light grayish appearance (cf. Figure 53 in the appendix), it is a mostly fine dispersed powder with some compacted pieces in the middle part of approximately a few millimeters in size. X-ray powder diffraction shows that the obtained powder is mostly magnesium hydride (approx. 92.5 mass – %), but also residual magnesium powder (< 1.0 mass – %), magnesium oxide (approx. 3.5 mass – %) and magnesium nickel hydride (approx. 3.0 mass – %) could be found. The detected magnesium oxide comes from the starting material because magnesium and nickel particles were handled under ambient air. Metallic magnesium, which is found in the X-ray pattern, can be explained by the fact that some magnesium is not converted into magnesium hydride. This incomplete conversion is caused by hindered diffusion of the hydrogen atoms through already formed magnesium hydride layers, within the hydrogenation step of 2 hours [18].

Even though the nickel has its function as a catalyst for the formation of magnesium hydride, it was incorporated itself into the metal hydride Mg_2NiH_4 . Therefore, no signal of nickel, but of magnesium nickel hydride can be found in the pattern. This can be explained by the formation of an intermetallic compound of nickel and magnesium during the dehydrogenation phase [10]. Thermogravimetric analysis shows a mass loss of approximately 5.77 mass – % at 380 °C, which is in the range of 5 to 6 mass – % hydrogen in nickel activated magnesium hydride, as presented in the literature [45]. The theoretical hydrogen mass fraction is 7.66 mass – % in magnesium hydride.

6.1. Synthesis of nickel activated MgH_2 and Mg_2FeH_6

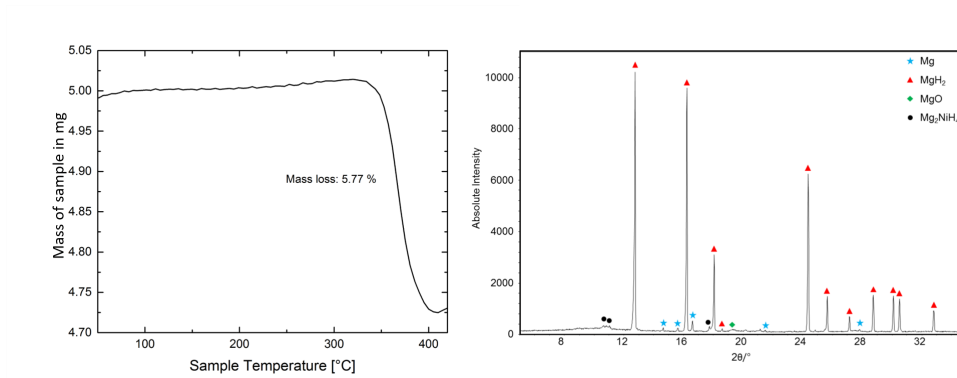


Figure 6.4.: Thermogravimetric analysis (left) and X-Ray pattern (right) of synthesized nickel activated magnesium hydride.

6.1.5. Synthesis of Mg_2FeH_6

For the synthesis of the material, 6.52 g (0.268 mol) magnesium powder ($< 45 \mu\text{m}$ particle size) and 7.48 g (0.134 mol) iron powder ($< 45 \mu\text{m}$ particle size) were mixed. This process was carried out under ambient atmosphere, in order to simulate an up-scaled process in which the educts will be possibly prepared under air atmosphere. The process parameters were chosen, to meet the upper application limitation of Mg_2FeH_2 as high-temperature heat storage material.

According to Figure 6.2, the sample powder mixture was exposed to 470°C at 95 bar of hydrogen for 24 hours in order to run the first hydrogenation of the magnesium iron powder. Subsequently, a temperature program was started, which is presented in Table 6.3. It consists of four steps. Firstly, the magnesium iron hydride is dehydrogenated by the increase of the temperature from 470°C to 550°C with a heating rate of 5 K/min. Dehydrogenation pressure is 101 bar. The temperature is kept constant at 550°C for 3 hours to release the entire hydrogen from the material. The third step is the hydrogenation which is initiated by reducing the temperature to 470°C , with a cooling rate of 5 K/min. At the last step, the temperature is kept constant at 470°C for 3 hours in order to fully hydrogenate the sample. The resulting gas pressure was 91 bar. These four steps were repeated for 20 times, beginning with the dehydrogenation step, in order to accomplish 21 cycles of H_2 discharging and charging.

6. Results and Discussion

Table 6.3.: One cycle of the temperature-controlled program for the synthesis of the magnesium iron hydride

step number		Temperature in °C	Time in h:min:sec	Temperature ramp in K/ min
1	Dehydrogenation	470–550	00:16:00	5
2	Dehydrogenation	550	03:00:00	-
3	Hydrogenation	550-470	00:16:00	5
4	Hydrogenation	470	03:00:00	-

In Figure 6.5, magnesium hydride is shown which was prepared by 21 cycles of dehydrogenation and hydrogenation in an autoclave. With the obtained pressure difference of 10 bar and the sample mass of 14.47 g³, the hydrogen uptake in the material could be estimated to be 3.3 mass – %. The theoretical mass fraction of hydrogen in Mg₂FeH₂ is 5.4 mass – %. In order to understand the reason for the difference between the theoretical value and the obtained hydrogen content, the sample material was removed from the autoclave under argon atmosphere to avoid ignition and contamination. The product was a fine green powder in which no compacted parts were observable. The material was investigated by thermogravimetric analysis and X-ray diffraction.

The thermogravimetric analysis shows a mass loss of 3.9% at a temperature window between 260 °C and 330 °C. The hydrogen content is a little bit larger compared to the hydrogen mass fraction determined by the pressure difference during the synthesis. This might be caused by the fact that the entire sample bed is not hydrogenated as the TGA sample powder. Some parts could be inactive. A reason for the relatively low hydrogen content of the product (3.8 mass – % to 5.4 mass – % in theory) is the low number of dehydrogenation and hydrogenation cycles of 20. An additional reason lies in the preparation of the metal mixture under air. This might have caused further contamination with oxygen, which was investigated by X-ray diffraction.

³The sample mass is calculated from the starting material mass of magnesium and iron and the hydrogen content, which was determined by the pressure difference during the synthesis.

6.1. Synthesis of nickel activated MgH_2 and Mg_2FeH_6



Figure 6.5.: Magnesium iron hydride as synthesized from the autoclave (left) and the filled measurement cell 3rd Generation (right).

The XRD pattern, right in Figure 6.6, shows clear reflexes of magnesium iron hydride but still, signals of magnesium hydride are visible. The formation of material composition of magnesium iron hydride and magnesium hydride by a thermal process under hydrogen atmosphere is already described in literature by Bogdanovic et al. [69]. Even though there is a stoichiometric mixture of magnesium and iron powder, there are enough local spots in which is an excess of magnesium. In these areas there is the formation of MgH_2 possible but no second reaction to Mg_2FeH_6 (Equation 2.8). This might be explained by the formation of magnesium islands in the sample during the mixing. It is well known in literature that thermal process leads to the formation of MgH_2 – Mg_2FeH_6 mixtures [71].

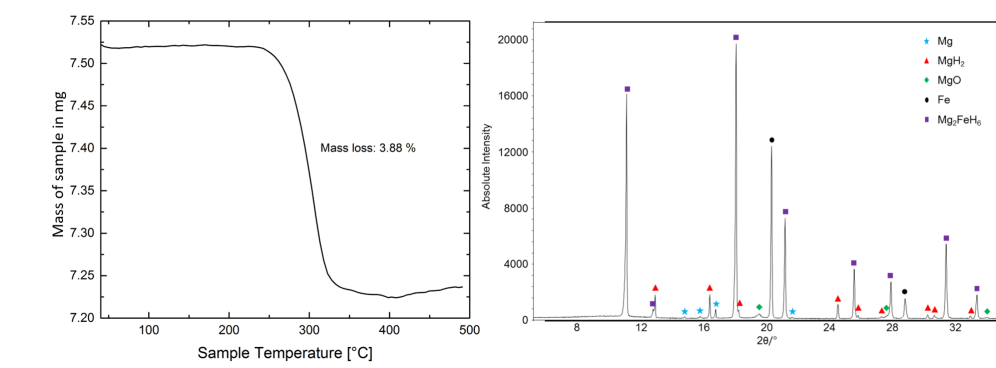


Figure 6.6.: Thermogravimetric analysis (left) and XRD pattern (right) of magnesium iron hydride.

6. Results and Discussion

Rietveld analysis shows that the product is a compound of 64 mass – % Mg_2FeH_2 , 10 mass – % MgH_2 , 9 mass – % MgO , 16 mass – % Fe and 1 mass – % Mg . Considering the results of the Rietveld analysis the hydrogen content is 4.28 mass – %. This is in good agreement with the result of the thermogravimetric analysis of 3.9 mass – % (cf. left plot of Figure 6.6).

6.2. ETC measurement of magnesium powder

This chapter describes the results of the effective thermal conductivity measurement of magnesium particles under a hydrogen atmosphere at gas pressure between 1 and 100 bar and temperatures from 25 to 100 °C. For these measurements, the 1st generation measurement cell was used (see Chapter 5.2). These results help to explain and to understand how the ETC of relatively metal powders under a gas atmosphere behaves with changing sample temperature and changing hydrogen gas pressure.

The material was used as bought from the supplier and has a purity of at least 99.0%, as depicted in Table 6.4. For defining the particle size, the so-called mesh size is given by the supplier. This material was filled in the 1st generation measurement cell under ambient conditions. After connecting the autoclave with the gas supply system, it was purged with hydrogen and evacuated for at least three times in order to remove most of the residual oxygen and water molecules.

6.2.1. ETC as a function of the packed bed's packing density

In the first measurements, the influence of the packing density φ in the packed bed on the effective thermal conductivity was investigated. Therefore, magnesium particles of a size $< 297 \mu\text{m}$ (sample A) have been chosen to perform these investigations. The packing density is the volume of the solid content divided by the

Table 6.4.: Magnesium powder for ETC measurement investigation.

	Supplier	Mesh	Particle size	Purity
A	Sigma Aldrich	50	$< 297 \mu\text{m}$	$> 99.0 \%$
B	Alfa Aesar	325	$< 45 \mu\text{m}$	$> 99.8 \%$

6.2. ETC measurement of magnesium powder

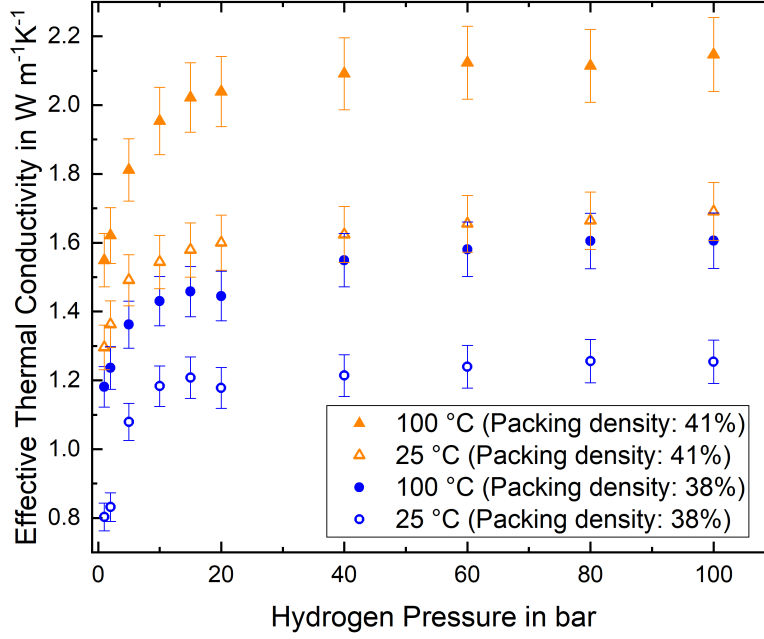


Figure 6.7.: Effective thermal conductivity of magnesium powder of mesh 50 with different packing densities, different gas pressure and at two different temperatures.

overall volume of the measurement cell and can be expressed by:

$$\Phi = \frac{V_{\text{Mg}}}{V_{\text{cell}}} = \frac{m_{\text{Mg}}}{\rho_{\text{Mg}} V_{\text{cell}}} \quad (6.4)$$

V_{cell} presents the free volume in the measurement cell (17.04 cm^3) and ρ_{Mg} is the density of magnesium (1.74 g cm^{-3})⁴. Two different packing densities of 38 % and 41 % were realized by compressing $m_{\text{Mg}} = 11.21 \text{ g}$ (0.46 mol) and 12.03 g (0.49 mol), respectively, of magnesium powder A in the measurement cell. The theoretical maximum is 74 % in the closed-packing of equal spheres [80].

In Figure 6.7 the ETC of magnesium powder is displayed as a function of the applied hydrogen pressure of 1 to 100 bar, at 25 °C and 100 °C for two different packing density fractions, as mentioned above.

The ETC increases with increasing temperature from approximately $1.2 \text{ W m}^{-1} \text{ K}^{-1}$ at 25 °C to $1.6 \text{ W m}^{-1} \text{ K}^{-1}$ at 100 °C, at 100 bar and a packing density of 38 %. A similar behavior shows the ETC of the sample with the packing density of

⁴The magnesium oxide layer of the particles and other impurities are neglected for this calculation.

6. Results and Discussion

41 % which increases from $1.7 \text{ W m}^{-1} \text{ K}^{-1}$ to $2.1 \text{ W m}^{-1} \text{ K}^{-1}$.

The second feature is the strong pressure dependency of the ETC in the pressure range of 1 to 20 bar, in which the measured values increase by 30 to 50 %. This is caused by the Smoluchowski effect and has been described in Chapter 3. At a gas pressure above 20 bar, the ETC is almost independent of the hydrogen pressure.

The packing density has a big impact on the effective thermal conductivity. By comparing the ETC values at $25 \text{ }^\circ\text{C}$ and a gas pressure of 1 bar hydrogen, a higher packing density of 41 % (compared to 38 %) leads to a raised ETC. It increases from $0.8 \text{ W m}^{-1} \text{ K}^{-1}$ to $1.1 \text{ W m}^{-1} \text{ K}^{-1}$. The same trend can be observed at other temperatures and gas pressures. The explanation is that the thermal conductivity in magnesium is three magnitudes of order higher than in hydrogen gas (see Table 3.3, in Chapter 3). A larger amount of solid phase in the volume leads to an increased heat transfer capability by conduction.

6.2.2. ETC as a function of the particle size

In this chapter, the dependency of the particle size of the magnesium particles on the ETC will be discussed. Figure 6.8 presents the measured ETC values of magnesium particles of different particle sizes and with the same packing density of 41 %. The results are plotted logarithmically to make a comparison to this dependency more visible.

In Figure 6.8, there is a clear difference to observe when comparing the ETC values from magnesium powder with different particle sizes but the same packing density of 41 %. Smaller particles (black marks in Figure 6.8) have a stronger dependency on the applied gas pressure than the larger particles. At pressures below 5 bar, the ETC of the sample with the bigger particles is higher. The thermal conductivity of the finer particles becomes larger at pressures above 5 bar.

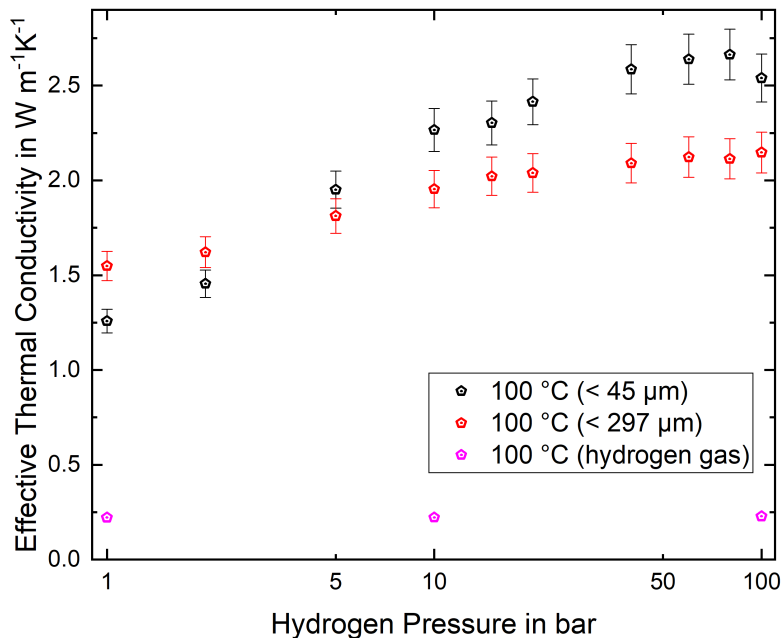


Figure 6.8.: Effective thermal conductivity of magnesium powder of different particle sizes with a packing density of 41 % at 100 °C. For comparison, the thermal conductivity values of hydrogen are presented by the purple marks.

6.2.3. Model for the heat transfer in a packed bed

This chapter provides a microscopic description of the particle size and gas pressure dependency on the thermal conductivity of the magnesium particle bed, which was investigated in the previous part. An explanation for a better thermal conductivity in a packed bed of large particles ($< 297\ \mu\text{m}$) than in a packed bed of small particles ($< 45\ \mu\text{m}$), near a bar gas pressure, can be the following: The heat is mainly transported in the solid phase of a packed bed, thus in the particles and between these particles, at the particle-particle contact areas. The difference between large and small particles is that within the same distance in a packed bed of small particles the number of interfaces is much larger than in a packed bed of large particles. Interfaces are bad thermal conductors and thus act as thermal resistances. Therefore, the effective thermal conductivity, near the atmospheric gas pressure, is higher in a packed bed of large particles than of small particles.

One possible explanation for the changing pressure dependency on the ETC with changing particle size in a packed bed can be given by discussing the contact point of two particles. For this explanation, the gas volume around the contact point of two particles is considered. The thermal conductivity in the gas volume around the solid-solid contact is gas pressure-dependent [111]. This model is combined is presented in Figure 6.9, which is adapted and modified from [112].

In this model, it is assumed that heat transfer by radiation and convection can be neglected. Furthermore, the particles are considered to be spheres which are in single-point contact, as depicted in Figure 6.9.

Figure 6.9 shows a schematic drawing of the contact of two spherical particles and the main heat conduction paths, as the conduction through the interface of the particles Q_S , the heat conduction through the gas in large voids Q_g and the heat conduction in the gas volume (green area in Figure 6.9) around the contact point of the particles Q_{Kn} . The heat conduction Q_S stays constant under the condition that no pressure is increasing the direct contact area between particle 1 and particle 2 (no Hertzian pressure is occurring). The thermal conductivity of the gas in the large voids is independent of the gas pressure, as described in chapter 3.1.5 and [112].

The thermal conductivity in the volume around the contact point of the particles shows a pressure dependency. It can be described with the Smoluchowski effect, which describes the reduced thermal conductivity of gas, because the distance D between the particles (Figure 6.9) is in the same order of magnitude as the mean

6.2. ETC measurement of magnesium powder

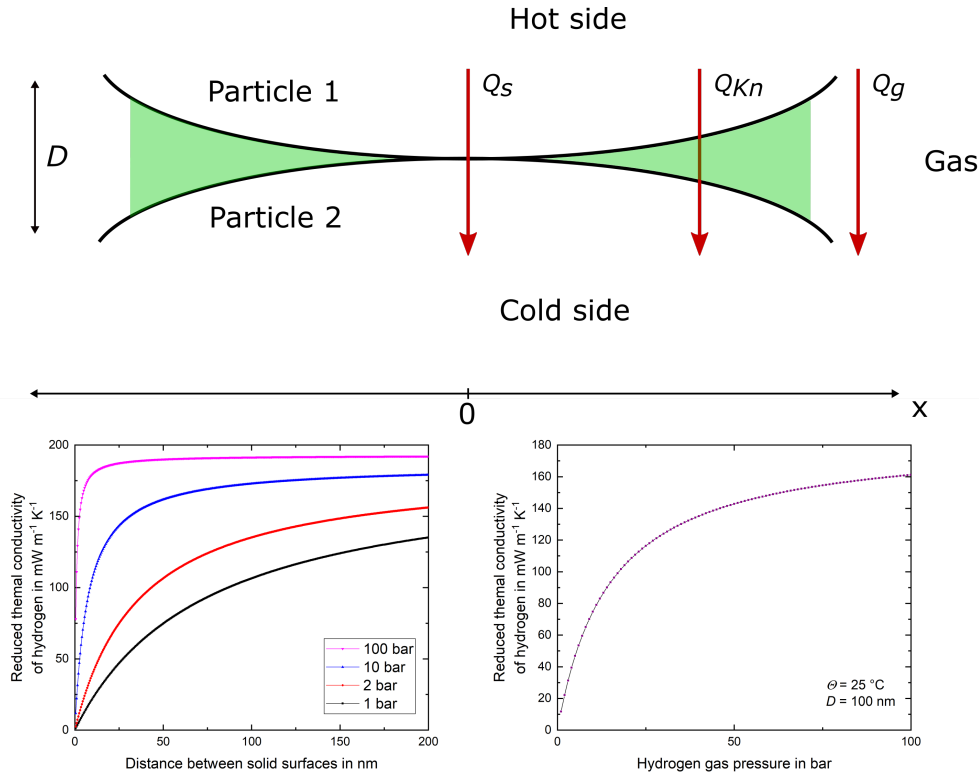


Figure 6.9.: Schematic drawing of the contact area between two spherical particles. The main heat conduction paths are the heat conduction via the contact area of the two involved particles Q_s , the heat conduction through the gas in large voids Q_g and a gas pressure-sensitive region between the particles Q_{Kn} . On the left bottom, the calculated reduced thermal conductivity of hydrogen gas is presented as a function of the distance D between two solid surfaces, at 25°C and different gas pressures. On the right bottom the reduced thermal conductivity of hydrogen gas in a void of 100 nm distance as a function of the gas pressure.

free path of the molecules λ , which itself is pressure dependent.

In the left bottom of Figure 6.9, the reduced thermal conductivity of hydrogen at 25°C is presented as a function of the distance D between the surfaces of two particles. These values were calculated with equations (3.8),(3.9) and (3.10), for the temperature of 25°C and gas pressures of 1,2,10 and 100 bar. As depicted in the left graph of Figure 6.9, the thermal conductivity increases with an increasing distance between the surfaces of the particles. At elevated gas pressures the thermal conductivity increase is stronger pronounced than at lower pressure. In the right graph of Figure 6.9, the calculated reduced thermal conductivity of hydrogen gas is presented as function of the gas pressure, at a surface-surface distance D of 100 nm and a gas temperature Θ of 25°C . Non-Linear enhancement of the thermal conductivity with increased gas pressure is observable in Figure 6.9.

6. Results and Discussion

Since a lot of these particle-particle contacts are present in a powder bed, the heat transfer by conduction in such a particle bed is influenced by the gas pressure. In a packed bed of small particles ($< 45\ \mu\text{m}$) the amount of these junctions is a lot bigger than in a packed bed of larger particles ($< 297\ \mu\text{m}$). Therefore, the powder bed of small particles (black marks in Figure 6.8) experience a stronger pronounced enhancement of the ETC with increasing gas pressure than the powder bed of larger particles (red marks in Figure 6.8).

These outcomes might help to understand the results of the measurement of the effective thermal conductivity in metal hydrides which were subjected to dehydrogenation and hydrogenation reactions, which are accompanied by particle size changes. Additionally, this information is important for the results in the long-term test, which is described in Chapter 6.8.

6.3. ETC measurement of Magnesium hydride

In this chapter, the investigation of the thermal conductivity of magnesium hydride under operating conditions is described. Magnesium hydride (MgH_2) was provided by Sigma Aldrich and shows a chemical purity of 99.8% and a particle size of $< 45\ \mu\text{m}$ (Mesh 325). 9.82 g (0.37 mol) of the metal hydride was loosely filled into the autoclave of the 2nd generation measurement set-up (see Chapter 5.3). It is necessary to use the newly developed measurement cell because it can be operated under the harsh temperatures which are required to dehydrogenate the magnesium hydride and afterward to hydrogenate the dehydrogenated magnesium hydride powder. Considering the volume of the measurement cell of $30.2\ \text{cm}^3$ and the density of MgH_2 of $1.45\ \text{gcm}^{-3}$ [113], a packing density of 22.4% was achieved. The magnesium hydride was analyzed by TGA and XRD prior to the ETC measurements. The thermogravimetric analysis shows a mass loss of 7.0% (see Figure 6.10) above $400\ ^\circ\text{C}$ which is close to the theoretical value of 7.6% and in good agreement with literature [114]. The X-ray diffraction pattern on the right in Figure 6.10 shows clear reflexes for magnesium hydride. Furthermore, reflexes for magnesium and magnesium hydroxide can be found, which are caused by fabrication and storage⁵. A reflex for magnesium indicates a non-complete conversion to magnesium hydride. And the hydroxide might have been caused by the hydrogenation of the natural magnesium oxide layer on the magnesium

⁵Even though the material was just handled in gloveboxes, it was stored for a long time in the chemical container in chemical storage cabinet.

6.3. ETC measurement of Magnesium hydride

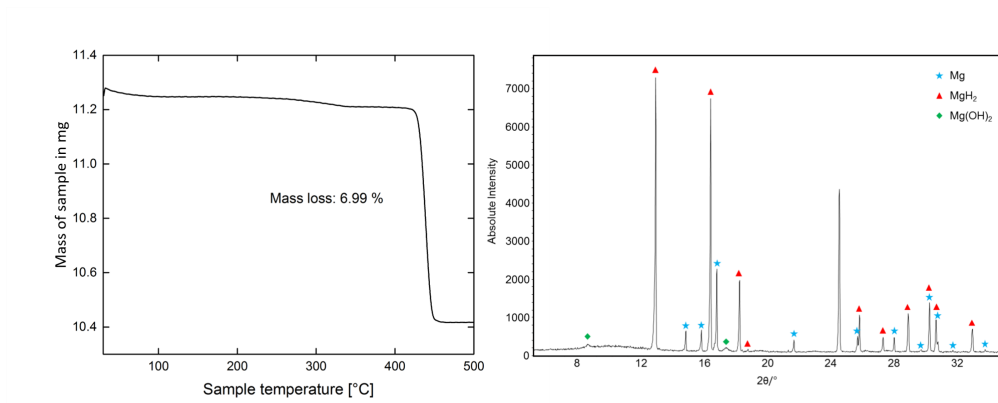


Figure 6.10.: Thermogravimetric analysis of MgH_2 prior ETC measurements, showing the characteristic mass loss above 400°C (left). X-ray pattern of the same material, which shows reflexes for MgH_2 , Mg and $\text{Mg}(\text{OH})_2$ (right).

particles.

The measurement cell and the sample were transferred into a glove box in order to prepare the sample under an inert atmosphere. The MgH_2 was placed in the measurement cell, which was closed with a flange under argon atmosphere of the glovebox. After placing the measurement cell in the furnace as shown in Figure 5.6, the gas inlet was connected to the test grid. The purging procedure was run, as already described in chapter 6.1.1.

6.3.1. Measurement of the ETC at a temperature of up to 300°C

ETC measurements of MgH_2 packed beds under a hydrogen atmosphere up to 25 bar was executed as described in chapter 4.1.2, firstly in the temperature range of 25°C to 300°C . In this range, the hydrogenation/dehydrogenation reactions of magnesium hydride/ -magnesium systems are thermodynamically unfavorable or kinetically hindered (see Chapter 2).

Figure 6.11 presents values, marked with full points, show the effective thermal conductivity of magnesium hydride under a hydrogen gas atmosphere at 25, 100, 200, and 300°C ⁶. The measured ETC of the magnesium hydride under hydrogen gas shows a strong dependency on the applied hydrogen gas pressure, to see in Figure 6.11. The ETC value at 25°C increases from approximately $0.64\text{ W m}^{-1}\text{ K}^{-1}$ at 1 bar to $0.80\text{ W m}^{-1}\text{ K}^{-1}$ at 25 bar. The ETC value at 300°C changes from

⁶Measurement parameters can be found in Table A.3 in A 7.

6. Results and Discussion

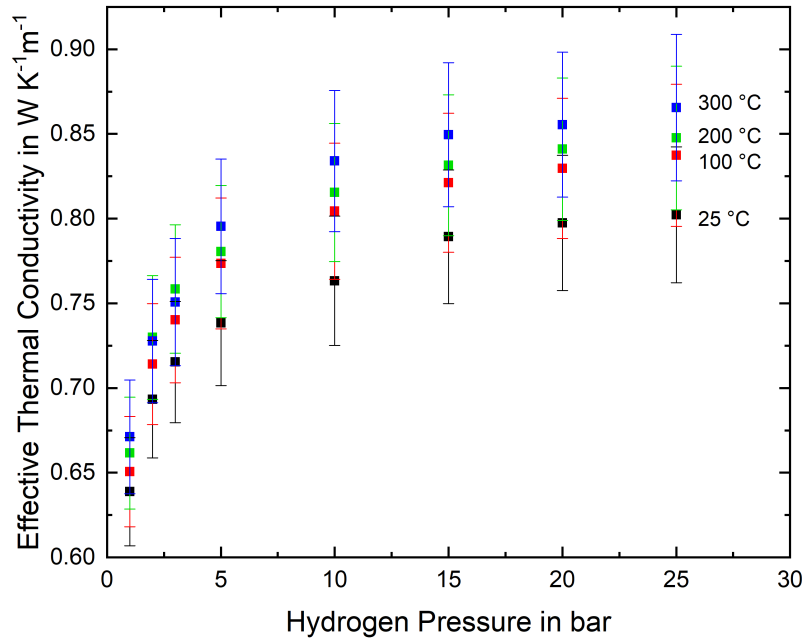


Figure 6.11.: Effective thermal conductivity of magnesium hydride under hydrogen gas pressure at sample temperatures between 25 °C and 300 °C.

0.67 W m⁻¹ K⁻¹ at 1 bar to 0.86 W m⁻¹ K⁻¹ at 25 bar. Especially in the pressure range up to 10 bar the pressure dependency is well pronounced.

The temperature dependency is less strong pronounced than the pressure dependency. The ETC values at 1 bar hydrogen gas pressure increased from 0.64 W m⁻¹ K⁻¹ at 25 °C to 0.67 W m⁻¹ K⁻¹ at 300 °C sample temperature. At 25 bar the ETC raises from 0.80 W m⁻¹ K⁻¹ to 0.87 W m⁻¹ K⁻¹, at a temperature of 25 °C to 300 °C.

The ETC does not increase linearly with a raised temperature. The difference between the ETC values at 25 °C and 100 °C are larger than the differences between the ETC values at 200 °C and 300 °C.

As discussed in chapter 6.2, the increasing ETC values with raising hydrogen pressure originates in the contribution of the gas molecules in the voids of the packed beds. It is mention worth, that the ETC of a gas-filled packed bed increases much stronger than the thermal conductivity of pure hydrogen gas with increasing gas pressure. The pressure dependency on the ETC in a packed is introduced by the gas molecules as the temperature dependency on the ETC in such a packed bed can be derived from the gas molecules in the voids. In Table 3.2 (chapter 3.1.5) it is shown that the temperature dependency of a gas thermal conductivity, which

6.3. ETC measurement of Magnesium hydride

is located in voids, increases non-linearly. Therefore it can be concluded, that the enhanced ETC with increased temperature, as shown in Figure 6.11 originates in the increased thermal conductivity of the gas phase.

6.3.2. Temperature coefficient of electrical resistivity (TCR) of the nickel sensor

As mentioned in the previous chapter, the sensor consists of a thin nickel foil that forms the double spiral. Nickel is an outstanding metal as sensor material which is applicable over a wide temperature range of -243.15°C to close to the melting point of nickel at 1451.85°C [101]. Another advantage of nickel is its high-temperature coefficient of resistivity (TCR), which describes how the electrical resistivity changes with changing temperature. This enables a precise determination of temperature changes in the sensor material, nickel.

There is one exception in which the sensor cannot be used. Nickel undergoes a transition of being ferromagnetic becoming paramagnetic at approximately 360°C , the so-called Curie point. At this temperature and in the temperature window around this point, the electrical resistivity of the nickel does not change linearly with increasing temperature (see the left plot in Figure 6.12). Own measurements show that the TCR values have a local maximum at about 380°C (see the right plot in Figure 6.12) and that the temperature range of 300°C to 400°C stands out with notable non-linear changes in TCR. This is, unfortunately, the window of operating temperature for magnesium hydride. The TCR data points (presented in red) were determined by measuring the electrical resistance of the sensor in 5 K steps in the range of 300°C to 420°C . Around the Curie point, in the range from 338°C to 382°C , the steps were reduced to 2 K. By deriving the resistance values over the temperature by point deviation, a new and more precise TCR could be determined (see following equation).

$$TCR = \frac{1}{R} \cdot \frac{dR}{dT} \quad (6.5)$$

The measured resistance is presented by R and the corresponding temperature by T .

By applying the new TCR values for the measurement of the effective thermal conductivity of magnesium hydride under working conditions, which means at

6. Results and Discussion

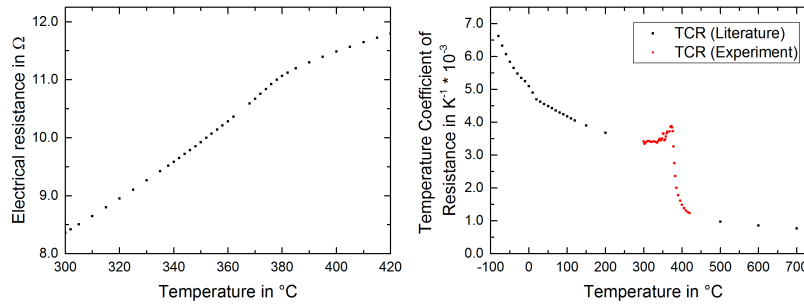


Figure 6.12.: The left graph presents the electrical resistance of the nickel sensor, plotted as the function of the temperature, which was recorded as the sensor was embedded in the magnesium hydride powder bed. The right graph shows the TCR of nickel as function of the temperature. The black dots are the literature values, given by *Hot Disk AB* and the red.

temperatures between 300°C and 400°C , the influence of the right choice of the TCR are observable. Figure 6.13 presents the ETC values measured with the literature and with the newly determined TCR values. The decrease of ETC until a temperature of around 370°C results from the increase of the original TCR values around this temperature. By adjusting the TCR this behavior can be avoided.

In general, it can be said that it is possible to measure the thermal conductivity in the range of 300°C to 400°C with the nickel sensor by applying the new TCR values. Determined results must be considered carefully. However, it is recommended to avoid measuring around the Marie-Curie temperature. Measurements were executed as well in this temperature window, but it was avoided to present results, in this work, which are determined at temperatures too close to the Curie point. As presented in Figure 6.13, the measured ETC value experience a jump at a temperature of 380°C .

6.3. ETC measurement of Magnesium hydride

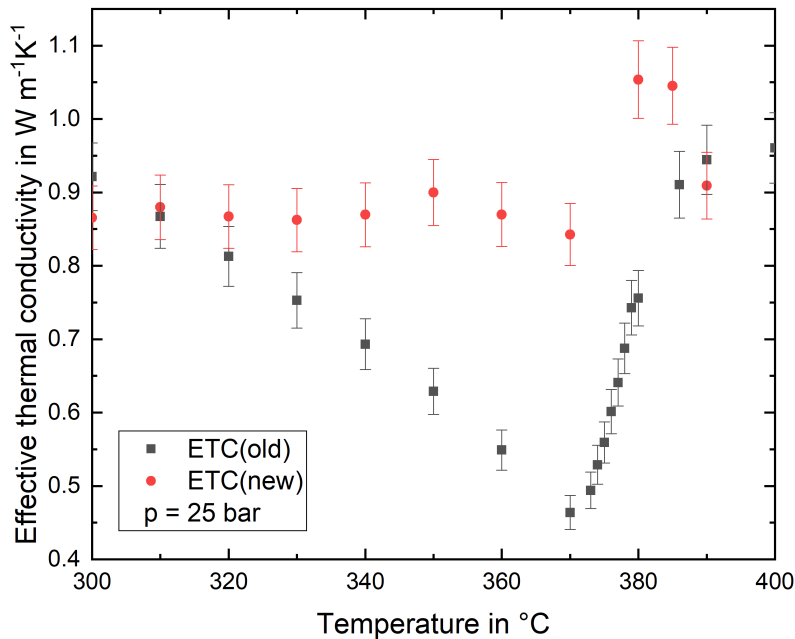


Figure 6.13.: Effective thermal conductivity of magnesium hydride under 25 bar hydrogen determined with the TCR values from literature (black dots) and the newly determined values (red dots), in the temperature range of 300 °C to 400 °C.

6.3.3. Measurement of the ETC at a temperature above 300 °C

After running experiments to investigate the thermal ETC of magnesium hydride below the operating temperatures and the determination of the TCR values of the nickel sensor for the temperature window of 300 to 400 °C, experiments were executed to determine the thermal conductivity under operating conditions. Therefore measurements were performed above 300 °C.

Figure 6.14 presents the ETC values which were taken at temperatures of 300, 390, and 410 °C⁷. The MgH₂ is in hydrogenated or in dehydrogenated state, respectively according to the equilibrium pressure curve in Figure 6.2. Considering the phase change at the Curie temperature of nickel, which is used as sensor material as described in the previous chapter, the measurements taken at 390 °C and 410 °C were considered for discussion. It is necessary to have on the one hand a large temperature difference to the Curie point to avoid an enlarged error, caused by this phase change. On the other hand, the temperature window should not exceed the maximum working temperature of magnesium hydride, which is limited to

⁷Measurement parameters can be found in the Appendix.

6. Results and Discussion

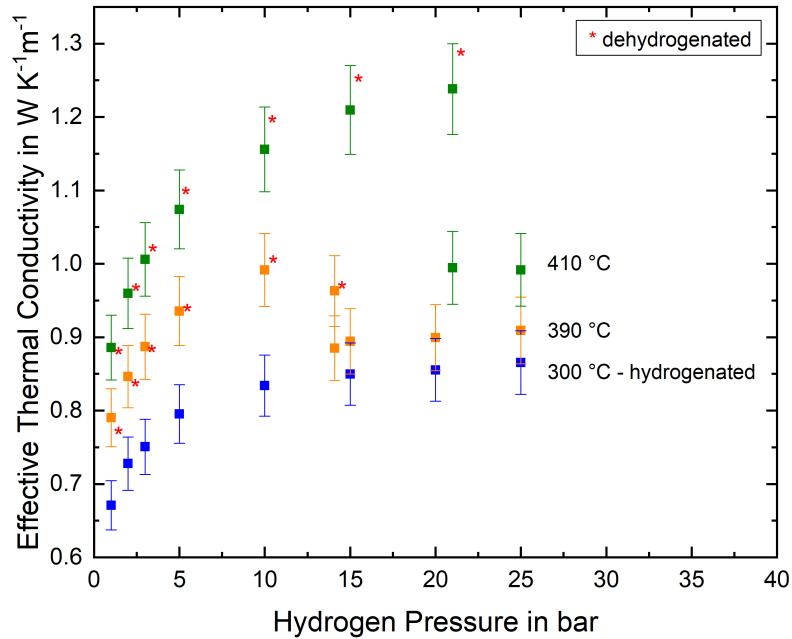


Figure 6.14.: Effective thermal conductivity of magnesium hydride under operating conditions.

a temperature of up to 450 °C⁸ [23]. The equilibrium pressure curve in Figure 6.2 depicts the conditions under which the hydrogenation of magnesium and the dehydrogenation reaction of MgH₂ occur. For magnesium hydride at 390 °C, the material decomposes at hydrogen gas pressures below 14.1 bar and at 410 °C below 21.1 bar. The ETC values are presented in Figure 6.14 as a function for the applied hydrogen gas pressure, in the range of 1 bar to 25 bar, for the temperatures of 300, 390, and 410 °C.

The blue marks are presenting the ETC values of the magnesium hydride at 300 °C and the yellow and green marks are presenting the ETC values of the MgH₂ packed beds at 390 °C and 410 °C, respectively. Since MgH₂ may appear in hydrogenated state or in dehydrogenated state, red stars presenting ETC values of fully dehydrogenated magnesium hydride. The marks without the red stars are showing ETC values of hydrogenated magnesium hydride.

The ETC increases from 0.79 W m⁻¹ K⁻¹ to 0.88 W m⁻¹ K⁻¹ by changing the temperature from 390 °C to 410 °C, at 1 bar hydrogen pressure. At 10 bar and between

⁸Furthermore, the maximum temperature in application is limited by the commonly used High Temperature Fluid (HTF), which are transporting the heat in and out the storage tank. The most common HTF's decompose above 420 °C.

6.3. ETC measurement of Magnesium hydride

the temperatures of 390 °C and 410 °C, this temperature dependency is even more pronounced.

As already mentioned in the previous chapter, the effective thermal conductivity at 300 °C changes with increasing hydrogen gas pressure at 25 bar, compared to the ETC at ambient pressure. The ETC of dehydrogenated MgH₂ at 390 °C and 410 °C increases with increasing gas pressure in the pressure range of 1 to 14.1 and 1 to 21.1 bar. The slightly decreased ETC value at 390 °C and at 14.1 bar compared to the ETC value at 10 bar might be caused by a partly hydrogenation of the material.

The most prominent feature in Figure 6.14, is the drastically decreased ETC of the hydrogenated MgH₂, compared to the values of the dehydrogenated magnesium hydride, at temperatures of 390 °C and 410 °C. At a temperature of 390 °C and 410 °C, two ETC values were recorded at a gas pressure of 14.1 and 21.1 bar, respectively. The difference of the ETC at a sample temperature of 390 °C and 14.1 bar is 0.08 W m⁻¹ K⁻¹ and at a sample temperature of 410 °C and 21.1 bar 0.025 W m⁻¹ K⁻¹.

The comparably high ETC values of the dehydrogenated material at 390 °C and 410 °C result from the fact that the material is in dehydrogenated state, which means that the heat transfer in the solid part of the solid-gas-system can be referred to lattice vibrations (phonons) and to the electron transport, as it is the case for metals [99]. The distinct pressure dependency on the ETC values can be attributed to the fact that dehydrogenated particles are approximately 30 % smaller in volume than hydrogenated particles [53]. As shown in chapter 6.2.2, with the assumption of an equally reduced void size, the pressure dependency becomes stronger pronounced for the overall heat transfer in packed beds of smaller particles.

Having a look at the ETC values which were obtained in the hydrogenated state e.g. at 25 bar hydrogen the measured values reach 0.85 W m⁻¹ K⁻¹, 0.88 W m⁻¹ K⁻¹, and 0.97 W m⁻¹ K⁻¹ at 300, 390, and 410 °C, respectively (see Figure 6.14). They show a similar trend regarding the temperature dependency as the ETC values of the dehydrogenated material but less pronounced. Furthermore, there is no distinct difference in the effective thermal conductivity to the applied gas pressure of 20 and 25 bar. This is caused, as mentioned in Chapter 3, by the pressure independent thermal conductivity of the gas, that is present in the continuum regime.

6. Results and Discussion

Until now there is the dependency of effective thermal conductivity of a magnesium hydride powered bed on the applied gas pressure, the bed temperature and the state, if hydrogenated or dehydrogenated.

6.3.4. The dependency of ETC on the cycle number

In order to investigate the impact of the cycle number on the ETC of the magnesium hydride packed bed, ETC measurements were performed after consecutive de-/hydrogenation reactions in the measurement cell. The thermal conductivity values of the packed bed at temperatures of 390 and 410 °C, and between 1 and 25 bar pressure are presented in Figure 6.15. The ETC values were recorded after 11 and 27 cycles at a temperature of 390 °C and after 10 and 28 cycles at a temperature of 410 °C, respectively. The marks with a red star are showing ETC values of dehydrogenated material.

As depicted in Figure 6.15 the effective thermal conductivity of the magnesium hydride is not independent of the number of de-/hydrogenation cycles. The ETC

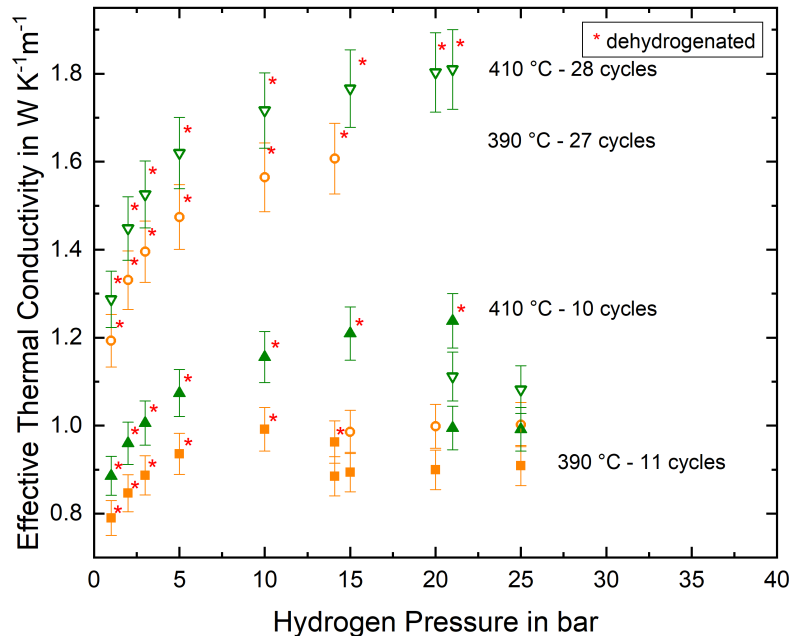


Figure 6.15.: Effective thermal conductivity of magnesium hydride at 390 °C and 410 °C as a function of the applied hydrogen pressure at different charging/discharging cycle numbers.

6.3. ETC measurement of Magnesium hydride

of MgH_2 at 410°C , which was cycled for 10 times is lower than the ETC of the same MgH_2 which experienced 28 cycles. The same trend is shown at 390°C and cycle numbers of 11 and 27. The measured ETC values are increased with enhanced cycle number. The charging and discharging cycles were performed by pressure changes during ETC measurements at temperatures above 350°C and below 410°C .

The determined ETC values at ambient hydrogen pressure rise from $0.8 \text{ W m}^{-1} \text{ K}^{-1}$ to $1.2 \text{ W m}^{-1} \text{ K}^{-1}$ and $0.9 \text{ W m}^{-1} \text{ K}^{-1}$ to $1.3 \text{ W m}^{-1} \text{ K}^{-1}$, for 390°C and 410°C , respectively. The increased values at ambient pressure and 390 and 410°C of the effective thermal conductivity can be explained by a probable new arrangement of the material [44]. This might be explained by the volume expansion during hydrogenation and volume shrinkage due to dehydrogenation in which the volume changes by approximately 30 % (see chapter 2.1).

The second distinct feature in Figure 6.15, is the pressure dependency on the ETC of dehydrogenated material, which is more pronounced after 28 or 27 cycles than after 11 or 10 cycles, at a temperature of 390 or 410°C , respectively.

The thermal conductivity of the packed bed at 390°C , which experienced 11 de-/hydrogenation cycles, increases by $0.15 \text{ W m}^{-1} \text{ K}^{-1}$ after increasing the hydrogen pressure from ambient pressure to 14.1 bar. After 27 cycles and 390°C , the ETC changes by $0.4 \text{ W m}^{-1} \text{ K}^{-1}$ after increasing the pressure from 1 to 14.1 bar. At the temperature of 410°C the ETC changes by $0.3 \text{ W m}^{-1} \text{ K}^{-1}$ in the pressure range between ambient pressure and 21.1 bar after 10 cycles and by $0.5 \text{ W m}^{-1} \text{ K}^{-1}$ for the sample which was cycled 28 times. Each of the ETC values of the hydrogenated material at 390 and 410°C is increased by $0.1 \text{ W m}^{-1} \text{ K}^{-1}$ at all hydrogen gas pressures above equilibrium pressure (see Figure 6.15).

The increased capability to transfer heat in the magnesium hydride regardless if hydrogenated or dehydrogenated may be caused by repeated charging and discharging with hydrogen. This repeated cycling of magnesium hydride leads to a change in the arrangement of the particles in the packed bed. In literature, this change is attributed to the merging of single particles during the hydrogenation, which results in the formation of coarse particle ensembles [44, 89, 115, 116]. Furthermore, it was shown in literature that MgH_2 powder beds might form a percolated magnesium hydride network, after experiencing de-/hydrogenation cycles at temperatures around 400°C . A more detailed discussion will follow after a long term cycle test, described in chapter 6.8.

6. Results and Discussion

Removing sample from the measurement cell

After all the measurements were executed, the material was removed from the measurement cell. Therefore, the autoclave was cooled down. During that, the hydrogen gas pressure was kept stable above the hydrogenation pressure in order to obtain fully hydrogenated material. The cell was disassembled under argon atmosphere in a glovebox.

The thermogravimetric analysis in Figure 6.16 shows a mass loss of 6.7%, which is attributed to the hydrogen [114], which desorbs from the magnesium hydride in the temperature range of 380 °C to 410 °C. The hydrogen mass fraction is in good agreement with the literature [114] and a bit less than the value of 7.0 mass %, which was measured before inserting the material in the measurement cell (cf. Figure 6.10). Furthermore, the onset temperature for the dehydrogenation is slightly reduced which can be explained by the refining of the particles during the repeated de-/hydrogenation reactions, as shown in the literature [115,117], causing a reduction of the dehydrogenation temperature [118]. Results of the XRD experiments show that additionally to magnesium hydride and magnesium, magnesium oxide and aluminum is present in the sample. The presence of magnesium oxide and aluminum might be the reason for the slightly reduced hydrogen fraction of 6.7%, compared to 7.0%.

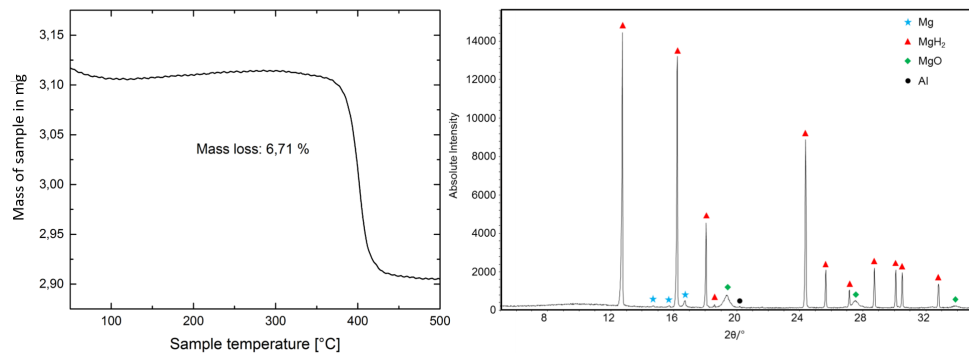


Figure 6.16.: Thermogravimetric analysis of MgH_2 after ETC measurements, showing the characteristic mass loss above 400 °C (left). X-ray pattern of the same material, which shows reflexes for MgH_2 , Mg, and MgO (right).

6.4. ETC measurement of nickel activated magnesium hydride

In this chapter the investigation of the thermal conductivity of nickel activated magnesium hydride under operating conditions is described. Adding nickel to magnesium is enhancing the reaction kinetics and therefore interesting for upscaled applications. This hydride was synthesized from magnesium and nickel powder under hydrogen pressure (see Table 6.1 and chapter 6.1.2). 9.60 g of the obtained nickel-activated magnesium hydride was transferred under an argon atmosphere into the 2nd generation measurement cell (30.24 cm³) where a packing density of 22% was achieved. This packing density is close to the packing density of the MgH₂, which was described in chapter 6.3. After sealing of the autoclave and the connection to the test rig and subsequent hydrogen purging, as described in chapter 5, measurements were performed.

6.4.1. Measurements of nickel activate MgH₂ at temperatures of up to 300°C

Firstly, measurements were executed at temperatures up to 300 °C and under hydrogen atmosphere up to 25 bar. Results are presented in Figure 6.17 which shows the effective thermal conductivity of the synthesized metal hydride in the pressure range of 1 to 25 bar hydrogen.

As depicted in Figure 6.17, the measured thermal conductivity of the nickel activated magnesium hydride, which experienced 51 cycles of dehydrogenation and hydrogenation, is presented for the temperatures of 25, 100, 200 and 300 °C as a function of applied hydrogen gas pressure. There is a pressure dependency of the ETC, especially in the range of 1 bar to 10 bar, for all sample temperatures. At temperatures above 100 °C, this effect is more pronounced. At 25 °C, the ETC increases from 0.56 W m⁻¹ K⁻¹, at atmospheric pressure to 0.77 W m⁻¹ K⁻¹ at 25 bar hydrogen. The same applies to the values of the samples at temperatures of 100, 200 and 300 °C, at which the ETC increases in the same manner. For all temperatures, the increase is in the range between 0.21 W m⁻¹ K⁻¹ and 0.26 W m⁻¹ K⁻¹.

At atmospheric pressure, the ETC increases at temperatures of 25 and 300 °C, from 0.56 to 0.64 W m⁻¹ K⁻¹. At a pressure of 25 bar, the temperature dependency is a little bit more pronounced than at atmospheric pressure. The temperature

6. Results and Discussion

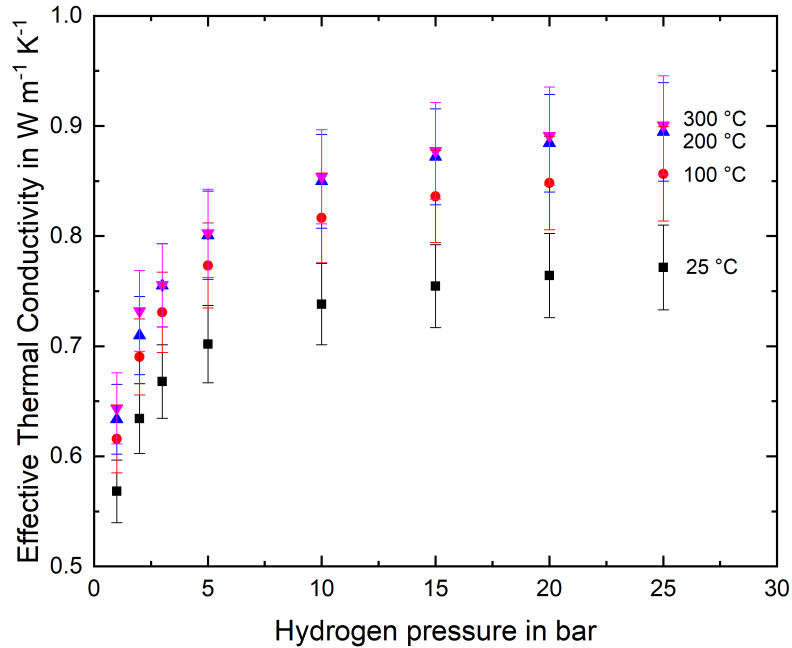


Figure 6.17.: ETC measurement of nickel activated magnesium hydride as a function of hydrogen gas pressure at temperatures up to 300 °C.

dependency of the ETC follows the same trend as mentioned in chapter 6.2. The heat transfer by conduction in gas increases non-linearly with the gas temperature, according to the kinetic gas theory (described in Chapter 3). Comparing the temperature dependency of the ETC of this sample (cf. Figure 6.17) with the ETC of the magnesium hydride in the previous Chapter (cf. Figure 6.11), the temperature dependency is more pronounced in this one.

6.4.2. Measurement of nickel activated MgH_2 at temperatures above 300 °C

In this chapter, the ETC values of the nickel activated magnesium hydride powder bed at temperatures of up to 400 °C and a gas pressure of up to 25 bar will be discussed. These temperatures and gas pressure are the operating conditions of nickel activated magnesium hydride in heat storage applications.

The ETC values are presented in Figure 6.18. In this graph, the conductivity values of the sample at 25 °C, 300 °C, and 400 °C, as a function of hydrogen pressure are presented.

6.4. ETC measurement of nickel activated magnesium hydride

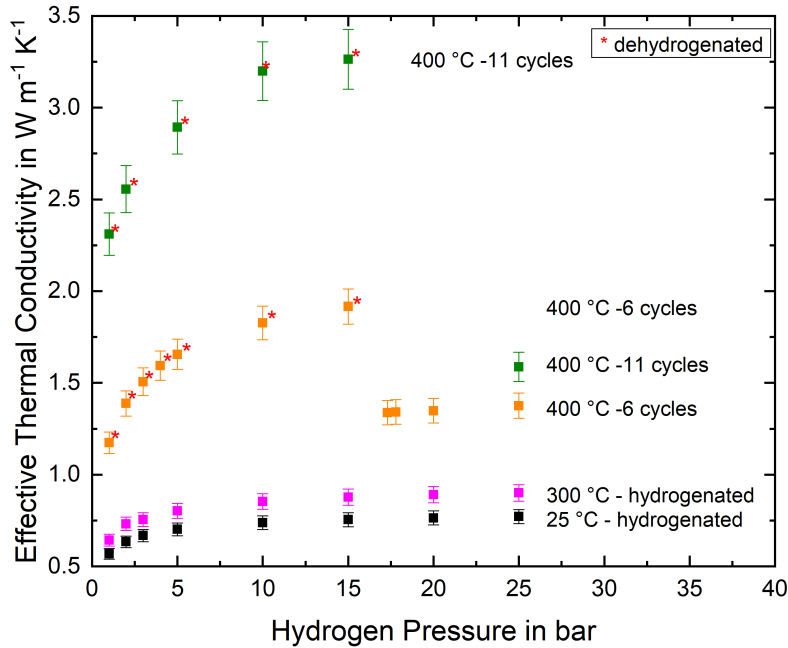


Figure 6.18.: Effective thermal conductivity of nickel activated magnesium hydride under operating temperatures as a function of the applied gas pressure

The values, which were measured at 25 and 300 °C (Figure 6.18), are the same values as presented in Figure 6.17 and present ETC values of magnesium hydride. The orange and the green marks in Figure 6.18 are presenting the ETC values at a temperature of 400 °C. The ETC values, which were recorded at 400 °C, are of a material that experienced 6 and 11 de-/hydrogenation cycles in the measurement cell. Since magnesium hydride can be hydrogenated and dehydrogenated at temperatures above 300 °C, there are ETC values of the material of two different states presented in Figure 6.18. The marks without the red stars are representing the measured values when the magnesium hydride is in the fully hydrogenated state. The marks with the stars are showing the ETC values of dehydrogenated material, which means it is considered to be a metallic (alloy) powder.

The dependency of the measured ETC on the applied hydrogen pressure and on the sample and gas temperature is observable, as Figure 6.18 clearly shows and which is comparable to the ETC plots of the MgH₂ packed bed in Figure 6.15. For the values of the sample at 400 °C, the pressure dependency is more pronounced than for the values of the sample at 25 and 300 °C.

The most prominent features are the exceedingly increased ETC values at a sam-

6. Results and Discussion

ple temperature of 400 °C, especially with respect to the cycle number. The values of the ETC increases in the hydrogenated state, measured at 25 bar, from 0.90 W m⁻¹ K⁻¹ at 300 °C to 1.38 W m⁻¹ K⁻¹ at 400 °C after 6 cycles. Furthermore, the same packed bed shows an ETC of 1.59 W m⁻¹ K⁻¹ after 11 cycles in total.

In the dehydrogenated state, the influence of the charging and discharging seems to have a bigger impact on the heat transfer capability. The thermal conductivity at 400 °C of the magnesium nickel powder increases from 1.17 W m⁻¹ K⁻¹ at 1 bar to 1.92 W m⁻¹ K⁻¹ at 15 bar. After 5 additional dehydrogenation and hydrogenation cycles, the ETC increases from 2.31 W m⁻¹ K⁻¹ at 1 bar to 3.26 W m⁻¹ K⁻¹ at 15 bar. The resulting difference between the conductivity values is 1.14 W m⁻¹ K⁻¹ at 1 bar and 1.34 W m⁻¹ K⁻¹ at 15 bar. The pressure dependency does not change with the increased cycle number but the offset at atmospheric pressure does.

The increased thermal conductivity of the nickel activated magnesium hydride bed is apparently caused by the repeated dehydrogenation and hydrogenation of the material, as shown in Figure 6.18. This cycling of magnesium hydride has an impact on the powder arrangement in the measurement vessel, as already described in chapter 6.3.4. Interestingly the material must undergo some changes in arrangement, thus the ETC changes just after a few cycles in the measurement cell, even though the material experienced already 51 cycles by the synthesis (chapter 6.1.2).

6.5. Comparison of the ETC of MgH₂ and nickel activated MgH₂

Both packed beds, from MgH₂ and nickel activated MgH₂ particles, experience a change of the thermal conductivity with the cycle number. In this chapter, the change of the ETC in the MgH₂ and the nickel activated MgH₂ as a function of the cycle number are contrasted.

It is noteworthy that the impact of the cycling number on the change of thermal conductivity is stronger pronounced in this nickel activated magnesium hydride sample than in the additive-free magnesium hydride. Table 6.5 serves for comparison and presents the ETC values. It shows that the thermal conductivity in the dehydrogenated state of the sample.

Even though both samples consist mainly of magnesium, which has a similar stor-

6.5. Comparison of the ETC of MgH₂ and nickel activated MgH₂

Table 6.5.: ETC values of MgH₂ and MgH₂ (4 mass – %Ni) as a function of the de-/hydrogenation cycles.

State		Number of cycles and ETC		Absolute and relative difference
		10	28	18 cycles
Magnesium hydride (410 °C)	Dehydrogenated (15 bar)	1.21 W m ⁻¹ K ⁻¹	1.77 W m ⁻¹ K ⁻¹	0.56 W m ⁻¹ K ⁻¹ 46.3 %
	Hydrogenated (25 bar)	0.99 W m ⁻¹ K ⁻¹	1.08 W m ⁻¹ K ⁻¹	0.09 W m ⁻¹ K ⁻¹ 9.1 %
		6	11	5 cycles
Nickel activated magnesium hydride (400 °C)	Dehydrogenated (15 bar)	1.91 W m ⁻¹ K ⁻¹	3.26 W m ⁻¹ K ⁻¹	1.35 W m ⁻¹ K ⁻¹ 97.8 %
	Hydrogenated (25 bar)	1.38 W m ⁻¹ K ⁻¹	1.59 W m ⁻¹ K ⁻¹	0.21 W m ⁻¹ K ⁻¹ 15.2 %

age hydrogen capacity, as presented by the results of the TG measurements (Figure 6.10 and Figure 6.16), thus similar thermodynamically properties and nearly the same starting packing density (25.6 % and 24.7 %) the difference of cycle-dependent thermal conductivities is tremendous. The increase of ETC in the nickel catalyzed MgH₂ is nearly twofold than in the non-catalyzed MgH₂. Additionally, the more distinct increase of ETC in the nickel catalyzed MgH₂ occurs after fewer dehydrogenation and hydrogenation cycles than in non-catalyzed MgH₂.

The reason for the difference between the non-catalyzed MgH₂ and the catalyzed MgH₂ in the cycle number dependency on the ETC might be the fact that nickel and magnesium tend to form alloys at temperatures above 350 °C [119]. Additionally, to the formation of coarser magnesium hydride particle ensembles during hydrogenation, the formation of nickel magnesium alloys can possibly initiate the development of coarser Mg-Ni-particle ensembles during the dehydrogenation steps at 400 °C.

Since the nickel activated MgH₂ is considered to be used in up-scaled applications, it will be exposed to more de-/hydrogenation cycles in order to investigate the ETC lifetime stability. The change of the ETC will be investigated and discussed further in Chapter 6.8.1.

6.6. Theoretical calculation of a cylindrical heat storage tank

High thermal conductivity of the metal hydride bed is beneficial for dimensioning a heat storage tank. To identify the significance of the thermal conductivity in metal hydrides as a heat storage material a theoretical calculation of the heat resistivity. The ETC values, which are used in this calculation are in the range of measured results, presented in the previous chapter. In this model a cylindrical heat storage tank (cf. Figure 6.19) was considered. A sinter tube for gas supply was placed in the center of a cylindrical reactor which was filled with dehydrogenated magnesium hydride. In this calculation, the heat resistivity of the heat flow from the center, where a reaction takes place to the high-temperature fluid (HTF), which acts as heat drain, was assumed. To simplify this calculation some assumptions had to be made:

- Axial heat transfer to the front and the back end are neglected.
- The metal hydride is homogeneously distributed.
- Heat in the metal hydride is transferred via conduction (radiation and convection is neglected).

The overall heat resistance can be split up into the resistance of the metal hydride bed R_{mh} , the heat transfer resistance from the metal hydride to the outer wall $R_{mh-wall}$, the heat resistance of the wall R_{wall} and the heat transfer resistance from the wall to the high-temperature fluid $R_{wall-HTF}$ (see Figure 6.19).

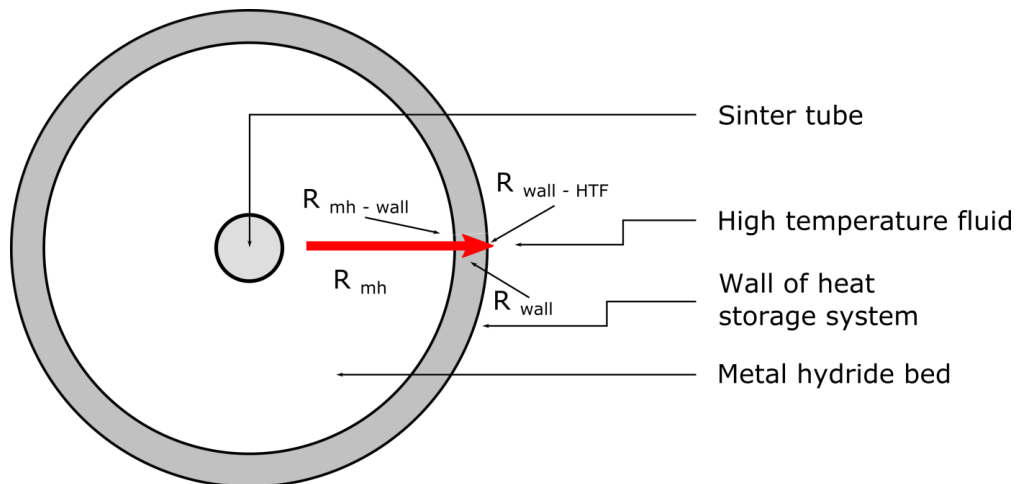


Figure 6.19.: Schematic draft of cross-section view on 2-D model for the theoretical calculation to estimate the influence of the ETC values of the metal hydride to the heat resistance.

6.6. Theoretical calculation of a cylindrical heat storage tank

Table 6.6.: Temperature, step time and/or temperature rate for the de-/hydrogenation experiment of Mg_2FeH_2 .

Assumed diameter of heat storage tank d	x
Length of heat storage tank L	700 mm
Diameter of sinter tube d_{st}	6 mm
Thickness of outer wall d_{wall}	2 mm
Thermal conductivity of the wall κ_{wall}	$15 \text{ W m}^{-1} \text{ K}^{-1}$
Inner heat transfer coefficient h_i	$50 \text{ W m}^{-2} \text{ K}^{-1}$
Outer heat transfer coefficient h_a	$1000 \text{ W m}^{-2} \text{ K}^{-1}$
Effective thermal conductivity 1 κ_1	$0.5 \text{ W m}^{-1} \text{ K}^{-1}$
Effective thermal conductivity 2 κ_2	$1.5 \text{ W m}^{-1} \text{ K}^{-1}$
Effective thermal conductivity 3 κ_3	$2.0 \text{ W m}^{-1} \text{ K}^{-1}$

$$R_{\text{total}} = R_{\text{mh}} + R_{\text{mh-wall}} + R_{\text{wall}} + R_{\text{wall-HTF}} \quad (6.6)$$

For the calculation of every single resistance some assumptions had to be made, which are presented in Table 6.6 and used in the following equation.

$$R_{\text{total}} = \frac{\ln\left(\frac{d}{d_{\text{st}}}\right)}{\pi L \kappa_{1,2}} + \frac{1}{h_i \pi L d} + \frac{\ln\left(\frac{d+4}{d}\right)}{\pi L \kappa_{\text{wall}}} + \frac{1}{h_a \pi L d} \quad (6.7)$$

The inner heat transfer coefficient is set to $h_i = 50 \text{ W m}^{-2} \text{ K}^{-1}$ [120, 121] which is the lowest value which has been reported in the literature. The outer heat transfer coefficient was set to $1000 \text{ W m}^{-2} \text{ K}^{-1}$ because to simulate a good heat transfer, which is basically caused by convection in the HTF.

A change of the heat transfer coefficient because of changing ETC of the metal hydride during hydrogenation is not considered. Furthermore, inhomogeneous powder distribution and fluctuation in packing densities are not contemplated in this model.

Pictured in Figure 6.20, it is clearly visible that all of the heat resistance sources differ with changing the outer diameter of the model heat storage tank. The strongest dependency can be found for the heat transfer between metal hydride and the wall ($R_{\text{mh-wall}}$) and the resistance in the metal hydride bed, under the assumptions, which were made above (cf. Table 6.6). By adding each source of heat

6. Results and Discussion

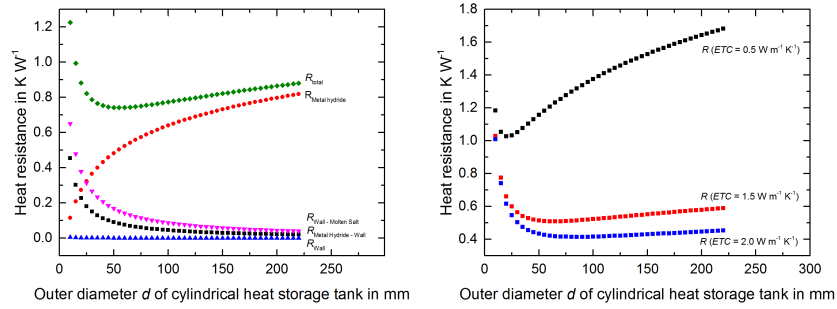


Figure 6.20.: Heat resistivity of the contributing sources for resistance with an assumed ETC in the magnesium hydride bed of $1 \text{ W m}^{-1} \text{ K}^{-1}$ (left) and the comparison of the overall heat resistivity between different ETC values of the metal hydride (right), as a function of the reactor diameter.

resistivity, an overall heat resistance can be found. Two main conclusions can be drawn, respective the results of this theoretical calculation. The first inference is, that an increased effective thermal conductivity of the metal hydride bed leads to a lower heat resistivity which finds a minimum at a larger diameter. Minima can be found at 20 mm (1.02 W K^{-1}), 65 mm (0.51 W K^{-1}) and 85 mm (0.41 W K^{-1}) of reactor diameter for an ETC of $0.5 \text{ W m}^{-1} \text{ K}^{-1}$, $1.5 \text{ W m}^{-1} \text{ K}^{-1}$, and $2.0 \text{ W m}^{-1} \text{ K}^{-1}$, respectively. In general, increasing the thermal conductivity in the metal hydride bed enables the design of larger heat storage tanks.

The second conclusion is that two sources of heat resistances are driving the overall heat resistivity. Even though the ETC in the metal hydride bed is increased much, the overall heat resistance will then be mainly defined by the heat transfer from the metal hydride powder bed to the wall. Both sources have to be considered while planning a heat storage tank. Additionally, it is worth to note, that the hydrogen diffusion and thus convection is not considered in this model and might be a crucial factor if the diameter becomes too large. The hydrogenation reaction spot might move from the inner part to the outer part but the reaction might as well takes place all over the sample, which would result that even the outer parts act as heat sources. To conclude, this simplified calculation shall give a rough idea about the importance and significance of a high thermal conductivity value in a metal hydride bed for the design of a heat storage reactor.

6.7. ETC measurement of magnesium iron hydride

This chapter describes the thermal conductivity measurements of stoichiometric magnesium iron hydride (Mg_2FeH_2). The material was synthesized from starting material magnesium and iron powder. The measurements were conducted in the 3rd generation measurement cell (see chapter 5.4).

13.27 g of the magnesium iron hydride/ magnesium hydride composition was transferred to the 3rd generation measurement autoclave under argon atmosphere to avoid further contamination with oxygen (right picture in Figure 6.5). The packing density of the powder is 17.78 %. After closing and sealing of the measurement cell, it was attached to the hydrogen gas supply set-up. The system was evacuated and purged with hydrogen three times prior to the opening of the gas inlet valve of the cell. Three more hydrogen flushing steps were executed to remove residual argon.

The first measurements were executed on fully hydrogenated magnesium iron hydride/magnesium hydride mixture at temperatures up to 300 °C. With the limitation to a temperature of 300 °C any dehydrogenation reaction is avoided [69]. The results of the effective thermal conductivity as a function of the applied hydrogen pressure are presented in Figure 6.21⁹. The lowest ETC value presented in this graph is $0.39 \text{ W m}^{-1} \text{ K}^{-1}$ at 50 °C and 2 bar hydrogen pressure. At 50 °C, the ETC increases to $0.45 \text{ W m}^{-1} \text{ K}^{-1}$ at 100 bar. At 300 °C, the thermal conductivity rises from $0.45 \text{ W m}^{-1} \text{ K}^{-1}$ to $0.54 \text{ W m}^{-1} \text{ K}^{-1}$ at gas pressures from 2 bar to 100 bar. The gas pressure has a higher impact on the thermal conductivity at higher temperatures. The temperature dependency on ETC is more pronounced at an elevated gas pressure.

These results show comparable gas pressure and temperature dependencies as the values presented in the previous chapters, in which non-activated and nickel activated magnesium hydride were investigated.

Even though the material is partly metallic and consists of about 74 mass – % of a metal hydride, the thermal conductivity is lower than in nickel activated magnesium hydride. This might have been caused by the lower packing density of 17.78 % (compared to 24.7%), which was already shown by comparing magnesium packed beds of different packing densities, in chapter 6.2.1. Another reason might be the fact that magnesium and nickel form an alloy at temperatures above

⁹Measurement parameters are presented in Table A.3 in the Appendix.

6. Results and Discussion

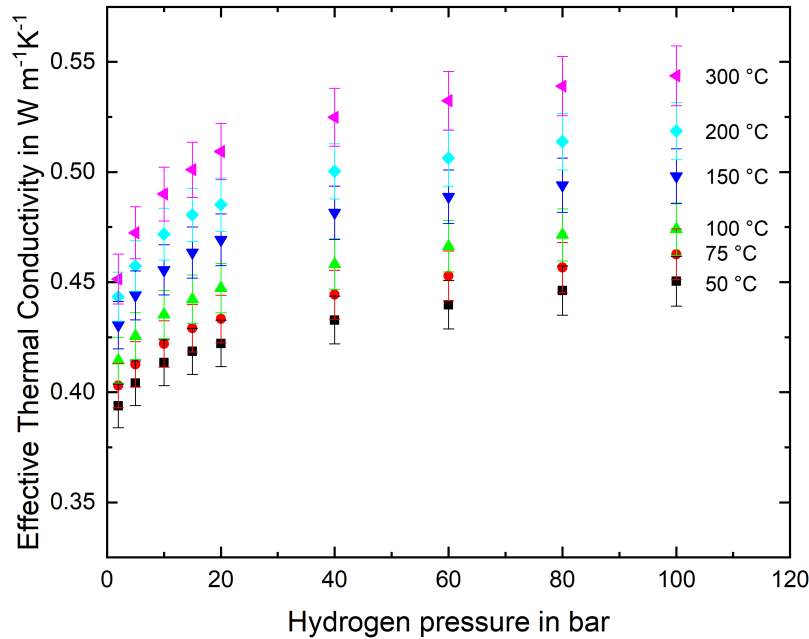


Figure 6.21.: Effective thermal conductivity of Mg_2FeH_2 powder under a hydrogen gas atmosphere.

350 °C, whereas magnesium and iron do not alloy under temperatures of up to 300 °C. Forming alloys might increase the chance of the formation of coarser particle ensembles, which would contribute for better thermal conductivity.

Conclusion

The effective thermal conductivity shows a similar gas pressure and sample temperature dependency as the non-activated and nickel activated magnesium hydride samples. Further experiments in which the cycle stability is investigated will be presented in Chapter 6.8.

6.8. Long term experiments

It could be shown in Chapter 6 that the influence of the effective thermal conductivity of the different magnesium hydrides depends on the sample and gas temperatures and the hydrogen pressure. But more importantly, there is a remarkable dependency on the number of de-/hydrogenation cycles to the ETC. This is the

reason that long term experiments were initiated in which nickel activated magnesium hydride and magnesium iron hydride were exposed to dehydrogenation and hydrogenation cycles.

The set-up is supplied with a one-liter autoclave, which acts as a hydrogen reservoir (Figure 5.1). In order to ensure temperature stability of the stored hydrogen gas, a heater is installed which kept the temperature of the vessel at constant 30 °C and to overcome day-night fluctuations of the temperature of the environment. To achieve a controlled temperature of the heater, a temperature controller *Dicon 308* was in use. The temperature of the measurement autoclave was controlled by a *Jumo Imago 500*, as described in Chapter 5.

6.8.1. Nickel activated magnesium hydride

The magnesium hydride which was in focus of this investigation was the same material that was used for the measurements in Chapter 6.4. It was cycled 51 times in the autoclave during the synthesis and was exposed to 13 additional dis-/charging cycles in the measurement cell prior to the long-term cycling test starts.

The starting conditions of the cycling were 355 °C sample temperature and 15 bar hydrogen gas pressure. The valves to the gas inlet and the outlet (V_1 and V_2 in Figure 5.1) were closed in order to have a closed system. After setting the operational conditions, a temperature-controlled program was started in which the temperature was increased from 355 °C to 420 °C with a heating rate of 5 K/min. During this step, the dehydrogenation process was initiated, and the magnesium hydride decomposed into magnesium and hydrogen gas. This evolution of hydrogen gas was noticeable due to increased gas pressure. The dehydrogenation step lasted for 2 hours at 420 °C to allow the material a full decomposition. After this step, the temperature was decreased again to 355 °C with a cooling rate of 5 K/min to hydrogenate the material again. The total hydrogenation step lasted for 2 hours and 13 min. By finishing the last step, one full cycle was completed. The process steps are summarized in Table 6.7.

After 24 of these un-/loading cycles, the temperature was set to 400 °C manually, followed by measurements of the effective thermal conductivity in the pressure range from 1 to 25 bar. Measurements were taken in hydrogenated and in dehydrogenated state. By decreasing the pressure to 1 bar, the material was dehydrogenated (Table A.2). After measuring the ETC of the material in dehy-

6. Results and Discussion

Table 6.7.: Process steps of one de-/hydrogenation cycle for the long term cycle test of magnesium hydride.

Step number		Temperature in °C	Time in h:min:sec	Temperature ramp in K/min
1	Dehydrogenation	355 - 420	00:13:00	5
2	Dehydrogenation	420	02:00:00	-
3	Hydrogenation	420 - 355	00:13:00	5
4	Hydrogenation	355	02:00:00	-

drogenated state, the pressure was increased above the equilibrium pressure (17.3 bar at 400 °C). Consequently, by executing these measurements of the magnesium hydride, the material is automatically subjected to another dehydrogenation and hydrogenation cycle. The 24 cycles prior to the ETC measurement and the de-/hydrogenation cycle during the measurement add up to 25 cycles, which were performed on the material.

Once the measurements were performed the dehydrogenation and hydrogenation cycles started again for 24 cycles. This was continued until the material has experienced 451 cycles in the measurement autoclave. The material was hydrogenated in total 510 times (synthesis plus cycling test plus some measurements after finishing the cycle test, see chapter 6.8.1).

ETC measurement

In Figure 6.22 the measured effective thermal conductivity of the nickel activated magnesium hydride is presented as the function of the number of dehydrogenation and hydrogenation cycles. The ETC readings are shown at a temperature of 400 °C and at a gas pressure of 1, 15 and 25 bar. All measurements were performed under equilibrium conditions.

As the most distinct feature in this plot, the ETC values in the dehydrogenated state increased strongly during the first 100 cycles. At a hydrogen pressure of 1 bar, it increased from 1.17 W m⁻¹ K⁻¹ after 6 cycles to 6.75 W m⁻¹ K⁻¹ after 76 cycles. At a hydrogen pressure of 15 bar, the ETC value increased from 1.92 W m⁻¹ K⁻¹ after 6 cycles to 7.71 W m⁻¹ K⁻¹, measured after 76 cycles. The maximum value, measured at 15 bar, which can be observed is an ETC of 8.05 W m⁻¹ K⁻¹ after 201

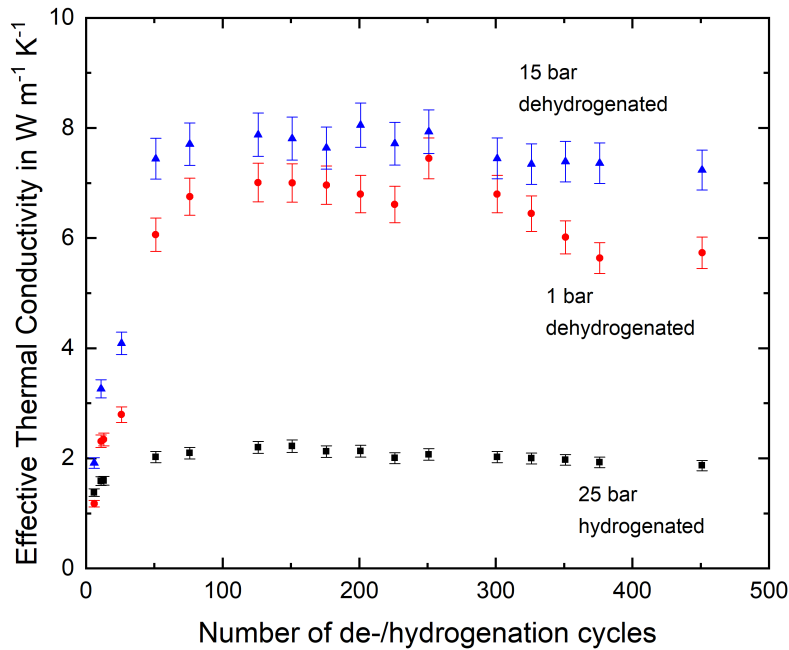


Figure 6.22.: Effective thermal conductivity of nickel activated magnesium hydride at 400 °C at 1, 15 and 25 bar hydrogen and as a function of the cycle number in the measurement cell.

dis/-charging cycles. Furthermore, once these relatively high thermal conductivity values were reached it did not increase further but rather declined slightly to an ETC value of $5.73 \text{ W m}^{-1} \text{ K}^{-1}$ at 1 bar and $7.23 \text{ W m}^{-1} \text{ K}^{-1}$ at 15 bar hydrogen, after 451 cycles.

In the case of the hydrogenated form of the nickel activated magnesium hydride, which is presented with the black dots in Figure 6.22, an increasing ETC values within the first 50 cycles can be observed. The ETC is presented at a hydrogen pressure of 25 bar. After 6 cycles the thermal conductivity was $1.38 \text{ W m}^{-1} \text{ K}^{-1}$ which increased to $2.10 \text{ W m}^{-1} \text{ K}^{-1}$ after 76 de- and hydrogenations. The maximum value of $2.22 \text{ W m}^{-1} \text{ K}^{-1}$ was reached after 151 cycles. After 451 cycles, the effective thermal conductivity was slightly reduced to $1.87 \text{ W m}^{-1} \text{ K}^{-1}$.

Hydrogen content during the long term cycle experiment

To investigate if the strong increase of the thermal conductivity in the nickel activated magnesium hydride bed (Figure 6.22) can be correlated to changes in morphology or thermodynamic properties, investigations were performed.

6. Results and Discussion

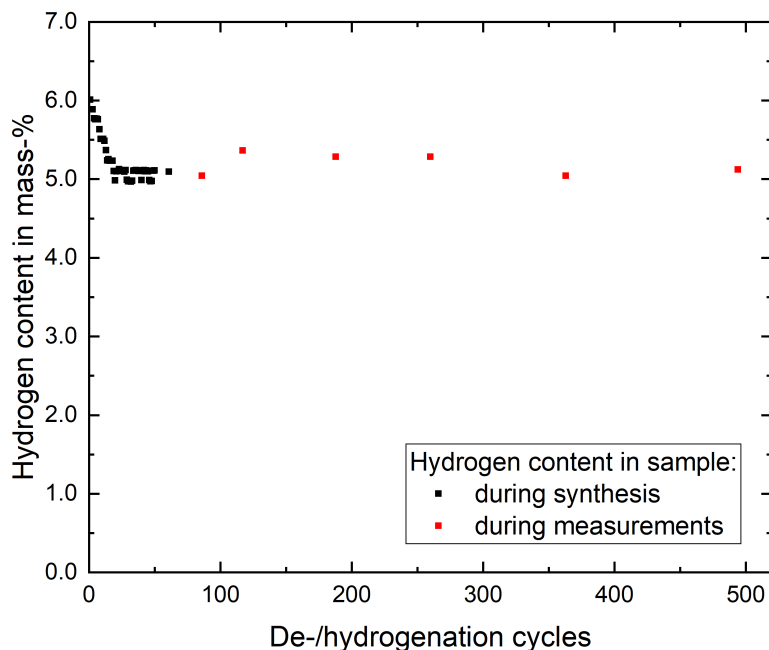


Figure 6.23.: Hydrogen content in the nickel activated magnesium hydride, during the synthesis and the cycling experiment, estimated from the difference between the dehydrogenation pressure and the hydrogenation pressure.

The results of the hydrogen mass fraction in the material are presented in Figure 6.23. The black marks present the hydrogen content which was recorded during the synthesis. The hydrogen pressure was recorded after each hydrogenation and dehydrogenation step. Subsequently, the pressure difference was calculated for every dehydrogenation and hydrogenation cycle. For the estimation of the hydrogen content, the pressure difference was used according to equation (6.3) in chapter 6.1.1.

The red marks presenting the hydrogen mass fraction, which were recorded during the long term experiment (Figure 6.22). A closer look at this figure presents the steep decrease during the synthesis, as already described in chapter 6.1.2. The hydrogen content which was calculated during the long term experiments is on average 5.1 mass – %.

The thermogravimetric analysis does not show any significant change or trend after the discharging and charging cycle test (Figure 6.22). The mass loss, determined by the TGA measurement was on average 6 mass – % after the long term experiment.

Interpretation of the results

Increase of the ETC

An explanation for the strong ETC increase of the nickel activated magnesium hydride can be found in the literature [23]. The MgH_2 is prone to form a network by repeated hydrogenation and dehydrogenation cycles at temperatures above $400\text{ }^\circ\text{C}$, as shown in [23, 44, 115]. An increased thermal conductivity is among others [23] one of the features of a percolated network. In the long-term cycle experiment for the determination of the ETC (Figure 6.22), the temperature was $355\text{ }^\circ\text{C}$ during hydrogenation and $420\text{ }^\circ\text{C}$ during dehydrogenation and thus in the temperature window under which the formation of a magnesium hydride network was observed in the literature [23].

Observation by eye showed that the material, which was placed in the measurement cell prior to the long-term cycle test was a loose fine powder (left picture in Figure 6.24). It had a homogeneous appearance. No chunks could be observed. In comparison, the material which was sampled from the measurement cell after the long-term cycle test was not a loose finely dispersed powder anymore (right picture in Figure 6.24). The right picture in Figure 6.24 shows powder in which material chunks are presented and larger pieces of the sample material. The formation of material pieces gives a hint to a change of the powder towards condensed particle arrangement and thus a changed thermal conductivity.

Another observation is the increased overall volume of the material, which can be seen in Figure 6.25. In the left picture of Figure 6.25, the nickel activated MgH_2



Figure 6.24.: Nickel activated magnesium hydride after 51 cycles of de-/hydrogenation (left), and nickel activated magnesium hydride after 510 cycles of de-/hydrogenation in the measurement autoclave (right).

6. Results and Discussion

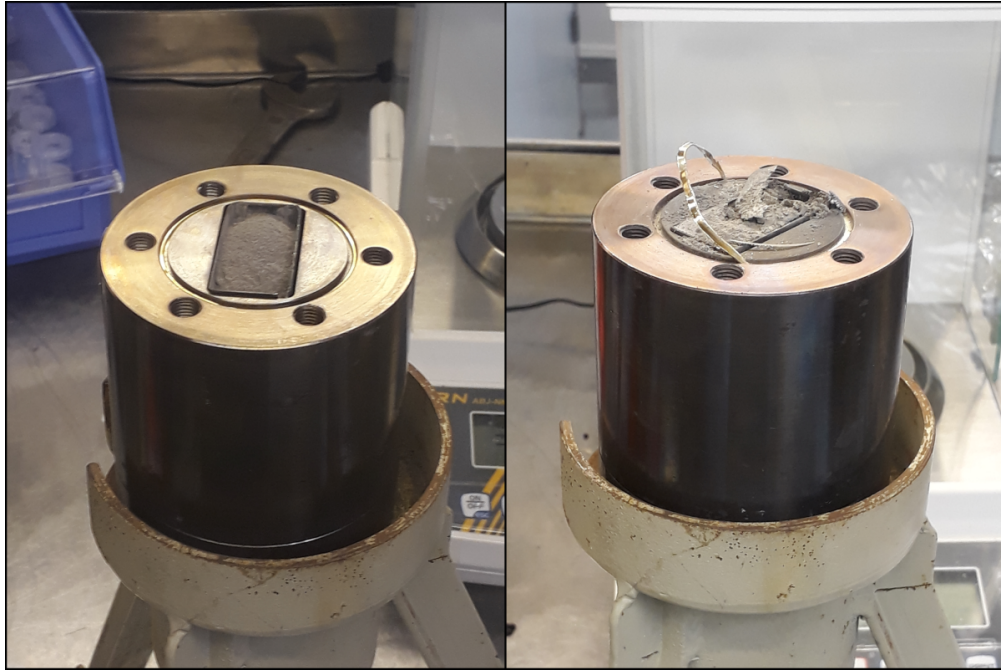


Figure 6.25.: The left picture shows nickel activated magnesium hydride, which was synthesized by 51 cycles of de-/hydrogenation and placed in the measurement cell for the ETC long term experiment. In the right picture, the nickel activated magnesium hydride can be seen, which experienced additionally 459 cycles of de-/hydrogenation in the measurement autoclave during the long term experiment.

prior the long-term experiment and in the right picture after the long-term ETC measurements can be seen. In the left picture, Figure 6.25 shows that the edge of the powder filling is not reaching completely the rim of the measurement cell prior to the long-term experiment. In the right picture of Figure 6.25, the material is expanded to the edge of the measurement cell. It appears to be compressed because the powder is not loose form but rather appears in pieces. This expanding behavior of MgH_2 after 150 cycles at $400\text{ }^\circ\text{C}$ had been shown in the literature [116]. The material seems to have been expanded in the measurement cell during the 459 de-/hydrogenation cycles.

In order to verify and to proof the statement of the formation of a percolated network and the expanding material filling, SEM investigations were performed. Additionally, EDX mappings were performed to investigate the elemental distribution in the samples.

At first, the nickel activated magnesium hydride powder, which experienced 510 cycles, was investigated with a Scanning Electron Microscope *SU3500 by Hitachi* to deliver an overview and an EDX analysis. Two samples will be presented; the first one is in hydrogenated state, as removed after 510 cycles from the measurement

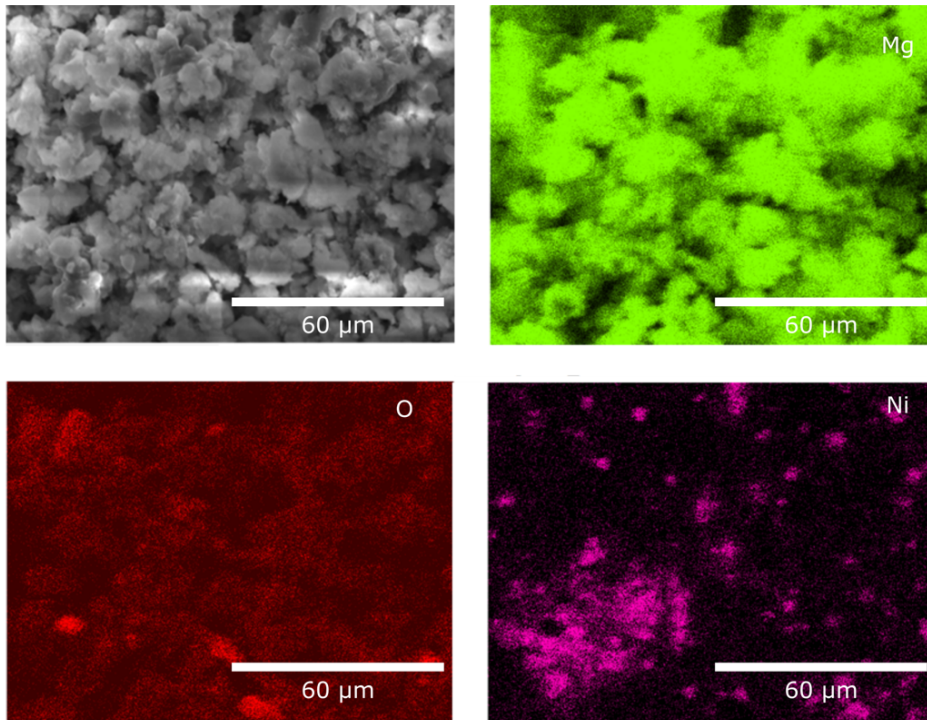


Figure 6.26.: SEM overview (magnification: 1000) of nickel activated magnesium hydride with EDX mapping after 510 cycles.

autoclave. The second sample is as well material, which was removed from the measurement autoclave but this one was subsequently dehydrogenated at 420 °C and 1 bar pressure in an autoclave. The micrograph of the hydrogenated sample at a magnification of 1000 and its elemental distribution of magnesium, nickel, and oxygen is presented in Figure 6.26. The image on the top left of Figure 6.26 shows a porous particle bed of particles in a size of a few microns to some tens of microns in different shapes and smaller voids in between. The particles seem to be connected by large areas. The particles have formed particle ensembles that have been growing together. The EDX mapping on the top right shows that all the particles contain magnesium as expected and that the magnesium is well distributed over this probe. The lower left picture presents the dispensation of the oxygen over the probe. Some spots are oxygen-enriched which leads to the conclusion that magnesium oxide particles are present in the sample. The nickel is accumulated at single spots and particles which results in nickel enriched part of the probe and parts in which no nickel is located.

The image on the top left, in Figure 6.27 shows a well-connected network of dehydrogenated magnesium hydride particles which consists of a few microns to some

6. Results and Discussion

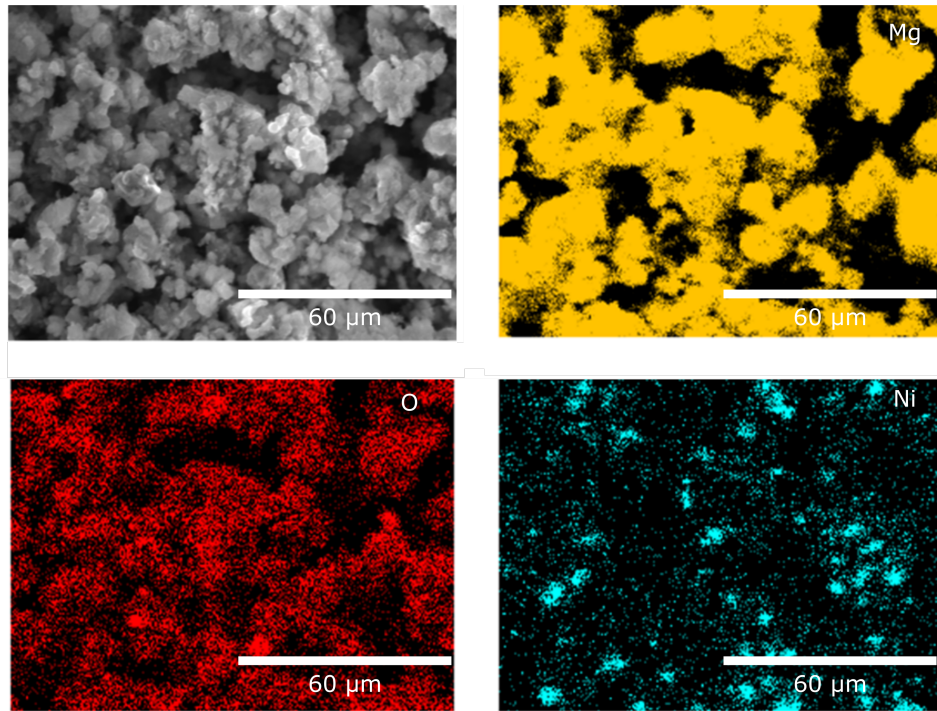


Figure 6.27.: SEM overview (magnification: 1000) of nickel activated magnesium hydride in the dehydrogenated state with EDX mapping after 510 cycles.

tens of microns. These particles are smaller than in the hydrogenated state, which is stated in Chapter 2.1. The voids between these grown-together particle ensembles are larger than in the hydrogenated magnesium hydride. The porosity is larger over the whole sample than the porosity in the hydrogenated sample. As in the hydrogenated material presented in Figure 6.26, the magnesium (top right) and the oxygen (lower left) are well dispersed all over this probe. The nickel again seems to accumulate at specific spots which results in an inhomogeneous distribution. The EDX spectra of both samples show – additional to magnesium, nickel, and oxygen – signals of fluorine, silicon, chlorine, calcium, and iron. The determined mass fraction sums up to approximately 1 mass – % in the mapping and can be attributed to the starting material, to impurities caused by the wall of the vessels and the thermocouple and can originate from the Mica capsulation of the ETC measurement sensor (Table A.4).

The observation of a connected network of the magnesium hydride particles (Figure 6.26) is comparable to the sponge-like appearance of an MgH_2 particle sample, which was cycled for 280 times at $400\text{ }^\circ\text{C}$ as presented in the literature [23]. The formation of the particle network can be attributed to two different mechanisms.

- During the hydrogenation, two neighboring magnesium particles, which are in physical contact, might merge together to one larger particle. This is due to the fact, that during the hydrogenation this material gains approximately 30 % of its volume [53]. This expansion of the particles is caused by the incorporation of two hydrogen atoms per magnesium atom, thus the crystal structure changes from simple hexagonal to tetragonal which has larger lattice constants (see Chapter 2.1). At the contact point the volume expansion causes an increase of the contact area. According to thermodynamics, it is favorable for a particle to reduce the overall surface area. Thus, during a subsequent dehydrogenation it might appear that the contact point is not fully restored which results in the formation of one larger magnesium particle instead of two smaller magnesium particles.
- During the dehydrogenation steps of the material at 400 °C, two neighboring magnesium particles might experience thermal sintering, which is possible because the sintering temperature is assumed to be 2/3 of the melting temperature. In the case of the magnesium, the sintering temperature is approximately 352 °C. This results in the formation of a larger particle. Unfortunately, an observation of sinter necks between particles could not yet be observed during the SEM investigation. One reason might be that the magnification was too low for the observation of sinter necks. Another reason might be the fact that the material was cycled for 510 times thus the contacts between these particles have grown too much to be identified as sinter necks.

Both mechanisms might have caused the formation of the coarse grown-together particle ensembles, as presented in Figure 6.26 and Figure 6.27. Another feature of the particle coalescence is the large void size in the dehydrogenated sample, as shown in Figure 6.27.

Stagnation of ETC

The stagnation of the increased thermal conductivity in the nickel activated magnesium hydride bed can be explained by the following: the particle size distribution and arrangement reached a point in which no change happened anymore which was caused by particle expansion, compression, coalescence, coarsening and sintering. The heat management during the hydrogenation was at a level at which no local over-heating could have caused any further process.

6. Results and Discussion

Decline of ETC

A slightly reducing effective thermal conductivity, measured at the presented gas pressures of 1,15 and 25 bar, can be observed in the range of the approximately 200th to the 459th cycle, in Figure 6.22. An explanation for this diminishing behavior of the ETC on the de-/hydrogenation cycle number can be given with X-ray analysis.

X-Ray diffraction and Rietveld analysis were performed to determine the composition of the material which was prepared by 51 cycles of dehydrogenation and hydrogenation (cf. Figure 6.4) and of the material which has experienced overall 510 cycles (cf. Figure A.3). The XRD pattern in Figure A.3 shows clear reflexes for magnesium hydride, magnesium nickel hydride, metallic magnesium, and magnesium oxide. A closer look via Rietveld analysis unveils that the largest amount in the obtained composition is magnesium hydride, as presented in Table 6.8. The content of MgH₂ prior to the cycle test is 92.5 mass – % and after 83.9 mass – %. This change of magnesium hydride content might be caused by an increased mass fraction of MgO, which is enhancing from 3.5 mass – % to 6.8 mass – % and an increased Mg₂NiH₄ content (3.0 to 8.2 mass – %). Enhanced oxide content can be attributed to either oxygen contamination during the whole experimental procedure of approximately 8 months or by the formation of more detectable crystalline magnesium oxide surface layers on the magnesium hydride particles and magnesium oxide particles.

The amount of magnesium is almost uninfluenced by the long-running time. It slightly changes, from 1.0 mass – % to 1.1 mass – % which can be attributed to the detection limit of X-ray diffraction.

Table 6.8.: Composition of the nickel activated magnesium hydride sample, determined by Rietveld analysis.

Component	Mass fraction of components in the sample which experi- enced 51 cycles	Mass fraction of components in the sample which experi- enced 510 cycles
MgH ₂	92.5 %	83.9 %
Mg ₂ NiH ₄	3.0 %	8.2 %
Mg	1.0 %	1.1 %
MgO	3.5 %	6.8 %

6.8. Long term experiments

The Rietveld results, presented in Table 6.8 will help to identify a possible reason for the decline in thermal conductivity after reaching a maximum after 200 cycles. It shows an increasing mass fraction of magnesium oxide in the sample material with an increasing number of cycles from 3.5 mass – % after 51 cycles to 6.8 mass – % after 510 cycles. This increasing oxide content might be originated in magnesium oxide particles and in the formation and growth of oxide layer. MgO has an average thermal conductivity of 45–60 W m⁻¹ K⁻¹ [122], which is lower than in pure magnesium (160 W m⁻¹ K⁻¹ [123]). There may be three reasons which can cause a reduction of the heat transfer capability in the magnesium powder bed caused by oxides. The first reason is the lower thermal conductivity of magnesium oxide, compared to magnesium. The second reason is the formation of new phases which act as resistance for the heat transfer. The third reason cannot be seen but it might be that the coalescence of the magnesium particles and their growth is inhibited by these oxide coatings.

Concluding this, the overall heat transfer in powder nickel activated magnesium hydride is at the first strongly determined by the state in which the material is present. In the dehydrogenated state, the thermal conductivity is higher than in the hydrogenated state. A second, crucial factor is the gas pressure, as can be seen in the dehydrogenated state. The difference of the ETC is approximately 1 W m⁻¹ K⁻¹ when comparing the values at 1 and 15 bars (Figure 6.22) With an increased number of cycling the heat transfer is more and more determined by the solid-solid interaction of the particles because the particles experience coalescence and coarsening.

After all the measurements were executed the magnesium hydride was removed from the measurement autoclave. For this, the autoclave was moved into the glove box in order to ensure that the material will not be contaminated with air and moisture during the removal process.

Influence of heating power and the number of data points for the evaluation of the calculated ETC values.

In the previous chapter, it could be shown that the magnesium hydride, which was removed from the measurement cell after the long-term cycle test was not loose powder. It consisted of powder as larger pieces and chunks. Therefore, the question arises if the presence of larger chunks can be observed with the ETC measurement. For this experiment, the working principle of the evaluation by

6. Results and Discussion

software will be shortly described in the following.

During the heating pulse of the transient reading in the measurement procedure of the TPS system, 200 data points are collected. These data points are recorded in equidistant intervals. This means that e.g. in a transient reading of 5 s, the time difference between each data point is 25 milliseconds because the 5 seconds are divided by 200. An option in the *Hot Disk Thermal Constants Analyzer (v. 7.2.10)* software allows discarding data points, by cutting them off. Therefore, it is possible to remove data points from the beginning of the transient reading time or the end of the transient reading. It is recommended to use at least 100 data points for the calculation of the thermophysical properties of the metal hydrides, as described in Chapter 4.1.1. This option is necessary because at the beginning of the measurement the insulating layer of the sensor and the surface of the sample material must be heated up. This temperature response of the insulating layer to the sensor shall not be included in the evaluation of the ETC of the metal hydride since it is not a property of the material. Removing data points from the end of the measurement time is sometimes required if the thermal response of the sample is disturbed by boundary effects of the measurement cell wall. This can occur if the penetration depth¹⁰ of the heatwave is exceeding double the shortest distance between the sensor and the wall. This might also happen if inhomogeneous parts with different thermal properties appear in the sample bed.

In this chapter the influence of the heating power of the sensor and the cut-off time from the beginning of the transient reading, to the measured ETC values will be discussed. For this experiment, measurements were performed on the nickel activated MgH₂, which had been hydrogenated 502 times in total (451 times in the measurement autoclave, see chapter 6.8.1). The first test was executed on fully hydrogenated magnesium hydride at 400 °C and 20 bar of hydrogen pressure. Transient readings were performed for 5 s and at heating power of 100, 150 and 150 mW. A lower or higher input power led to results that were beyond the warning level of the temperature increase, respectively, controlled by the software [94].

The influence of the heating power to the obtained ETC values is presented in Figure 6.28. The ETC values were determined from the measurement with three different times, being cut-off prior to the calculation. Three different time intervals, 0.5, 1.25 and 1.75 seconds were removed from the beginning of the transient read-

¹⁰Penetration depth is the total distance of the propagated heat wave during the transient reading. Not to confused with probing depth, which considers the measurement time for the calculation of the ETC [93].

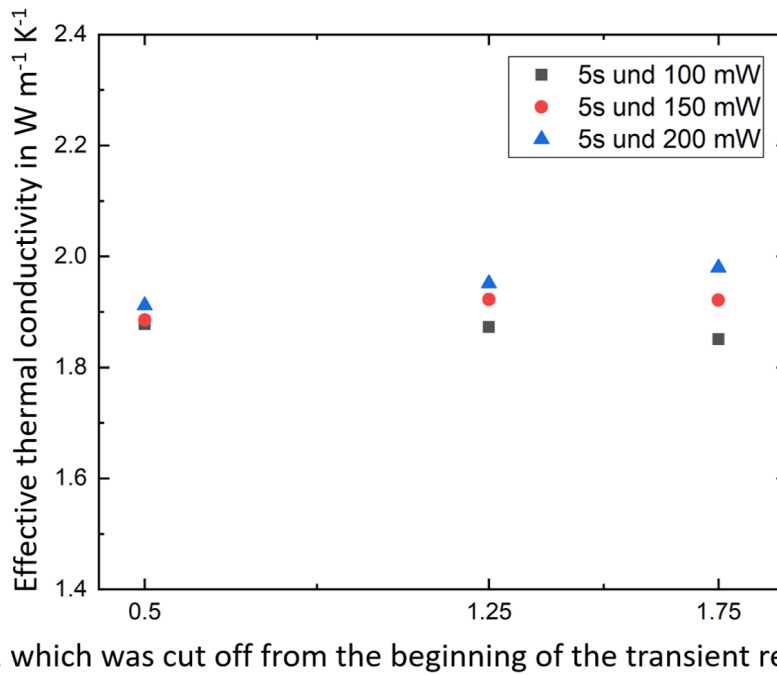


Figure 6.28.: The influence of the heating power and the time which was removed from the beginning of the transient reading before the calculation of the effective thermal conductivity of MgH_2 after 502 hydrogenations, measured at 20 bar hydrogen pressure and 400°C , was performed.

ing. The mean ETC values are $1.88 (\pm 0.02)$, $1.91 (\pm 0.03)$ and $1.92 \text{ W m}^{-1} \text{ K}^{-1} (\pm 0.04)$, for cutting off 0.5, 1.25 and 1.75 s from the start of the transient reading, respectively. The relative mean deviation in all three cases is in the range of 1–2%. This is within the standard specification of the TPS method for bulk materials (1–2%) [94]. Therefore, it is lower than the standard specification. There is no influence of the heating power or the removed time interval to the resulting ETC values of hydrogenated MgH_2 , as long as the control parameters are kept below the warning level.

The results of the ETC values of the dehydrogenated MgH_2 , removed after 502 cycles, measured at 1 bar hydrogen pressure and 400°C are presented in Figure 6.29. The transient reading time was 5 seconds and the heating power 100 and 150 mW in order to stay within the valid measurement conditions, as described earlier in Chapter 4.1.1. The cut-off time from the transient reading was chosen to be 0.5, 1.25 and 1.75 seconds, as in Figure 6.28. The mean ETC value is $6.02 (\pm 0.05)$, $6.00 (\pm 0.03)$ and $5.72 \text{ W m}^{-1} \text{ K}^{-1} (\pm 0.12)$, for the cut-off time from the start of the transient reading of 0.5, 1.25 and 1.75 seconds, respectively. The

6. Results and Discussion

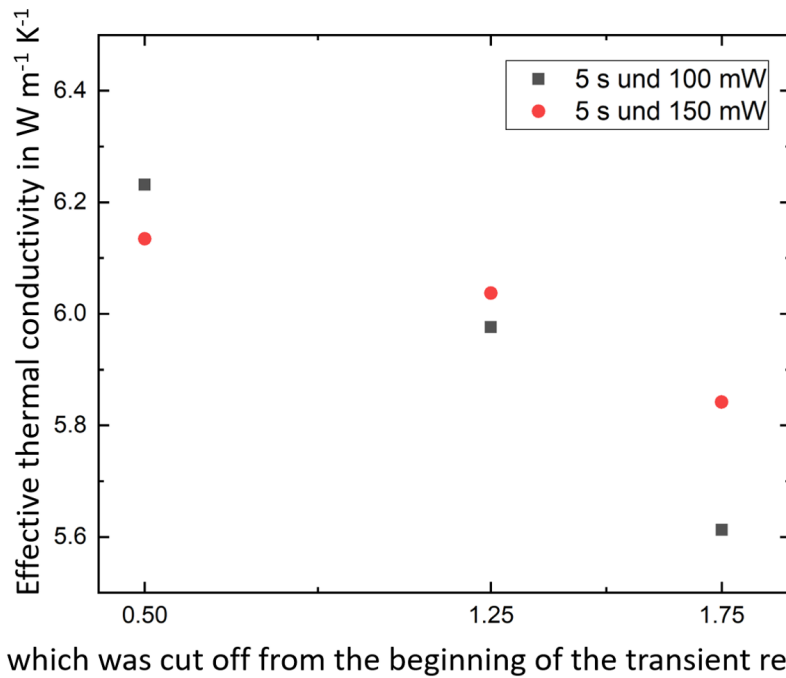


Figure 6.29.: The influence of the heating power and the time which was removed from the beginning of the transient reading before the calculation of the effective thermal conductivity of dehydrogenated MgH_2 after 502 hydrogenations, measured at 1 bar hydrogen pressure and 400°C , was performed.

relative mean deviations are in the range between 1 and 2 %, which is in the range of the standard specification for bulk specimen of 1–2 % [94].

The choice of the cut-off time of the transient reading does not have a significant effect on the determined ETC of the hydrogenated magnesium hydride, whereas it does for the calculation of the ETC in the dehydrogenated material (see Figure 6.28 and Figure 6.29). A visible feature in Figure 6.29 is the decline of ETC by reducing the evaluated measurement time. By cutting off 1.75 seconds of the transient reading the ETC appears to be lower than by skipping a shorter time interval for calculation.

To find an explanation for this observed trend, the meaning of cutting off measurement time will be explained in the following. As mentioned earlier in this chapter, cutting off time from the beginning of the transient reading allows neglecting the temperature drop between the sensor and the surface of the sample. This is necessary because measuring the temperature change in the sample is desired and not the thermal contact resistance between the sensor and the sample.

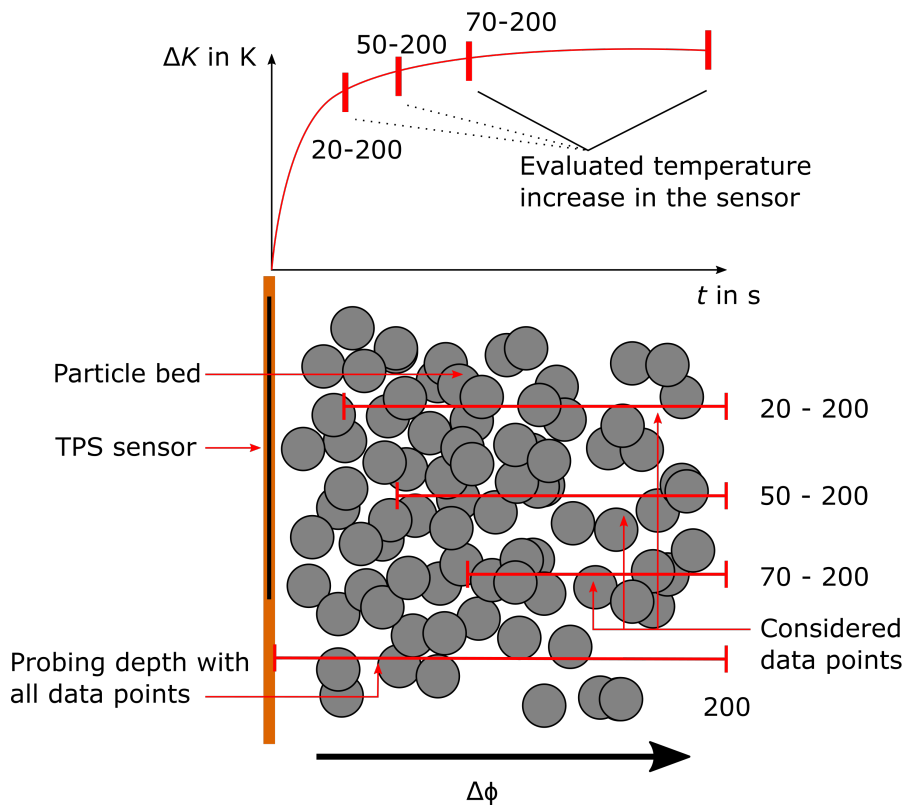


Figure 6.30.: Profile of TPS sensor in a powder bed with a gradient of the packing density, indicating different times t of the transient reading, which were considered for the evaluation (bottom). On the top, the schematic temperature increase of sensor as a function of measurement time with different time ranges for evaluation.

Experiments have shown that it is required to discard at least 20 data points for measuring the ETC of metal hydride powder beds, which is equal to 0.5 seconds at a total transient reading time of 5 seconds. By cutting off different amounts of time from the transient reading, the measurement window changes. Therefore, the considered temperature change is starting from different sample depths, as shown schematically in Figure 6.30.

The following description might give an explanation for the decreased ETC value of dehydrogenated MgH_2 in Figure 6.29, which was calculated by discarding 1.75 seconds from the beginning of the transient reading, compared to the ETC values which were calculated by discarding 0.5 and 1.25 seconds from the beginning of the transient reading. It is assumed that the dehydrogenated sample material has a slightly inhomogeneous packing density since the particles lose approximately 30% of its volume during the dehydrogenation (Chapter 2.1).

From the TPS sensor in the left of Figure 6.30, the heatwave propagates to the right side into the powder bed. Under the assumption that the temperature left of the

6. Results and Discussion

cut-off is at the same temperature, any further temperature increase of the sensor depends only on the thermal properties of the powder on the right side of the cut-off point. As depicted in Figure 6.30 the packing density of the dehydrogenated metal hydride powder bed decreases from the left to the right. By discarding time from the beginning of the reading (left side), the temperature increase of the area close to the sensor will not be considered in the ETC measurement. If a larger time interval from the beginning of the reading was removed, like 1.25 or 1.75 seconds, the ETC will be determined from the particle bed of lower packing density. This determined ETC will be lower than if the whole packed bed, including the high packing density bed, has been considered since the packing density is a crucial factor of the thermal conductivity in a packed bed.

The ETC measurement method gives an opportunity to qualitatively state about the homogeneity of the powder bed by evaluating the thermal conductivity.

Concluding remarks on the used error bars in this work. It could be shown that the influence of the heating power and skipped intervals of the transient reading time during the evaluation do not lead to a mean deviation of more than 5 % regarding the determined ETC values. Two values are given by literature [93] 1–2 % repeatability and 2–5 % accuracy. In this work, the accuracy will be used for the error bars. According to the ISO–5725–1, the accuracy is the sum of the trueness, which is the proximity of the measured values to the true value and the precision, which displays the repeatability and reproducibility of the measurements [124]. In this work, the error bars will be set to 5 %, according to [93], of the mean values of three readings that present one ETC value.

6.8.2. Iron magnesium hydride

Since the effective thermal conductivity of the nickel activated magnesium hydride changes so drastically, as described in Chapter 6.7.1, the question arises if these changes occur to other metal hydrides. Therefore, a similar cycling test was performed on magnesium iron hydride powder in order to investigate if similar changes occur as in magnesium hydride, which was presented in Figure 39. In literature, it is mentioned that magnesium and iron do not form any alloy, furthermore iron is considered to be an inhibitor for coarsening of the magnesium particles [125]. It is expected that the ETC does not experience such a tremendous change with an enhanced number of cycles, because the coalescence and coarsening were determined as main reason for the ETC change in a powder bed (Chapter 6.8.1). The ma-

6.8. Long term experiments

Table 6.9.: Temperature, step time and/or temperature rate for the de-/hydrogenation experiment of Mg_2FeH_2 .

step number		Temperature in °C	Time in h:min:sec	Temperature ramp in K/ min
1	Dehydrogenation	480–520	00:08:00	5
2	Dehydrogenation	520	03:00:00	-
3	Hydrogenation	520-480	00:08:00	5
4	Hydrogenation	480	03:00:00	-

material described in Chapter 6.5 was the probing material. As already mentioned, the powder is a mixture of magnesium iron hydride (64 mass – %), magnesium hydride (10 mass – %), magnesium oxide, magnesium and iron, which experienced 20 cycles of dehydrogenation and hydrogenation.

The parameters for this experiment were chosen to simulate as realistic conditions as possible, as presented in Table 6.9. The temperature and gas pressure regime was chosen to avoid the formation of magnesium hydride (see Figure 6.2). Measurements were performed after a few charging and discharging cycles at a pressure of 70 bar. The ETC is taken at temperatures of 480 °C and 520 °C, in the hydrogenated and dehydrogenated state, respectively.

The results of the cycling test are presented in Figure 6.31. ETC values are presented in the dehydrogenated and hydrogenated state with red and black points, respectively. The thermal conductivities do not change with the first 50 cycles. The ETC of the hydrogenated material stays at $0.75 \text{ W m}^{-1} \text{ K}^{-1}$ and in dehydrogenated state at $0.95 \text{ W m}^{-1} \text{ K}^{-1}$. The deviation between some measured values at specific cycle numbers can be explained by the slow conversion of metal to hydride and vice versa. If three data points are plotted for one cycle number, they present the values after 2, 2.5 and 3 hours of the reaction. The larger ETC values in the dehydrogenated state and the lower values in the hydrogenated state of the material are presenting the values which were measured after 3 hours. This means, that the ETC increases in dehydrogenated and decreases in hydrogenated with the time.

The feature of a stable thermal conductivity over the first 50 cycles in the powder bed of magnesium iron hydride confirms the hypothesis that the iron might prevent

6. Results and Discussion

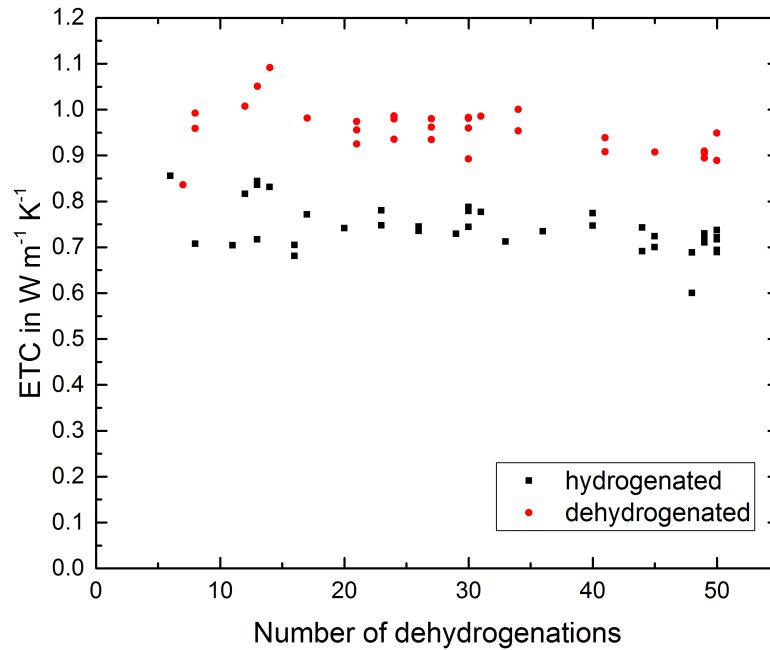


Figure 6.31.: ETC measurement of magnesium iron hydride powder bed as a function of the de-/hydrogenation cycles. The measurements were taken at a hydrogen pressure of 70 bar and at temperatures of 480 °C (hydrogenated) and 520 °C (dehydrogenated).

the formation of coarse particle structures, as shown in the case of magnesium hydride. Furthermore, the chosen temperature during these experiments is 100 °C higher than in the experiments on the nickel activated MgH_2 , as described in Chapter 6.8.1. One could expect that the coalescence and the coarsening of the magnesium particles at 520 °C would be more pronounced than at 420 °C, as in the experiment on the MgH_2 , which would lead to increased thermal conductivity.

The changes in the gas pressure in the H_2 -reservoir during the hydrogenation and dehydrogenation cycles enable the estimation of the absorbed and desorbed hydrogen in the probing material. It was found that 2.5–3.0 mass – % could be absorbed by the magnesium iron hydride/magnesium hydride powder. This hydrogen content of maximum 3.0 mass – % is a little bit lower than the value of 3.3 mass – %, which was observed after the synthesis of this material.

The reasons for the absence of a change of ETC values with an increased cycle number, presented in Figure 6.31 might be that iron and magnesium are immiscible. They do not form alloys at temperatures of 520 °C. The fact, that magnesium and iron are present in stoichiometric ratio leads to the conclusion that magnesium particles, which would experience coalescence (see Chapter 6.8.1), are locally separated by an iron particle¹¹. This separation inhibits the growing of a percolated network of the magnesium particles [18, 34, 43]. Since the Mg_2FeH_2 is decomposing during the dehydrogenation into particles which do not form an alloy and no percolated magnesium-magnesium network, many grain boundaries are present. These grain boundaries cause phonon scattering and are thus thermal resistances for phonon transport. This limits the thermal conductivity in a packed bed of iron and magnesium particles.

Because magnesium iron hydride is highly reactive and difficult to handle for SEM and EDX investigation it was not possible to evaluate the morphology and elemental distribution, as it was performed for the nickel activated magnesium hydride in this work.

¹¹Both types of iron particles, iron particles which are taking part in the reaction and the iron particles which are not reacting with magnesium to magnesium iron hydride.

7. Conclusion, final Remarks and Outlook

In this work the effective thermal conductivity under operating conditions of magnesium hydride, nickel activated magnesium hydride and magnesium iron hydride was investigated. Just a few publications can be found up to now in literature which has been surveying and determining heat transfer in metal hydride packed beds. Most of the work was performed theoretically and have had always some limitations and assumptions involved. As described in Chapter 3.3, the heat transfer of low-temperature metal hydrides has been determined by simulation, including the change of void fraction due to volume change during hydrogenation and dehydrogenation of hydrogen storage particles. This was not carried out yet for high-temperature metal hydrides in which heat related changes of the powder takes place. Experimental work was carried out by Kapischke et al. (see Chapter 3.3) in which the heat transfer in a magnesium hydride packed cylinder was determined via oscillating heating and an indirect determination of the thermal conductivity.

For measuring the effective thermal conductivity of magnesium based hydrides high pressure and high-temperature set-ups were developed and constructed. The first measurement set-up was constructed to enable measurement at temperatures of up to 100 °C and pressures of up to 120 bar. The designed 2nd Generation set-up facilitates a TPS sensor to enable direct measurement of the ETC under operating conditions of MgH₂, MgH₂ (4 mass – % Ni) and Mg₂FeH₂. It was possible to execute measurements at temperatures of up to 520 °C and hydrogen gas pressures of up to 100 bar. To achieve this, a measurement procedure was developed to enable as precise results as possible for reacting metal hydrides under above mentioned harsh conditions. Especially, the pressure control and handling are delicate for a successive operating of long term experiments under these harsh conditions. A third set-up was developed during this work which allows continuous use of a measurement set-up because the sensor had become easily accessible and replaceable.

7. Conclusion, final Remarks and Outlook

ETC measurements were performed on magnesium particles in order to find a strong dependency of the ETC on the porosity and particle size. Larger particles and a higher packing density lead to an enhanced thermal conductivity at close to atmospheric pressure. At higher gas pressure smaller particles achieve a comparably higher ETC. The pressure dependency of the ETC is stronger pronounced for smaller particles, as the dehydrogenated metal hydride particles steeply increase with raising gas pressure.

It could be shown that adding nickel to magnesium hydride does not influence significantly the thermal conductivity. The ETC in hydrogenated magnesium based hydride is basically not changing with changing gas pressure. This is caused by the fact that the gas molecules are in the continuums regime, in which the thermal conductivity of the gas is pressure independent (see Chapter 3.1). The dependency of the ETC increase to the sample temperature could be found to be related to the temperature dependency of the thermal conductivity of ideal gases in a confined pore system.

Long term ETC measurements could be performed over 8 months in order to do measurements of nickel activated magnesium hydride which was cycles in total 510 times. It was found that the coarsening of magnesium due to the repeated hydrogenation and dehydrogenation is having an enormous effect on the ETC. The biggest change of ETC occurred within the first 100 cycles. The porosity of the powder bed and the particle size distribution has a big impact on the behavior of a "breathing" material bed. Effects as the Hertzian contact stress, the mechanical and thermal properties play an important role in the formation of a sponge-like network in which the solid phase forms a continuous phase. The solid thermal conductivity has become the dominant mechanism for transferring heat in such a percolated matrix, as the pressure dependency does not change. As assumed this effect is not valid for immiscible powder mixture, which does not form any alloy under given conditions. This could be shown via a steady ETC of the magnesium iron hydride which was cycled for 50 times.

It could be shown that the formation of magnesium oxide and magnesium hydroxide do have little influence on the ETC but are overwhelmed by the formation of a percolated network of magnesium particles. Impurities, like oxygen, in small amounts reduce the heat transfer but not the overall stored hydrogen content. The nickel was incorporated in magnesium nickel hydride during the long term experiment.

The big challenge in measuring the thermal conductivity is the high temperature which makes the sealing and leakage proof measurement set-up sophisticated to develop, construct and to run. Especially, the electrical connection from the measurement cell to the hardware is prone to gas leakages. Another issue is hydrogen corrosion and elemental leaching from the nickel rich steel which was used for the construction of the measurement autoclave. The leaching of elements from the insulating layer of the Mica sensor can be investigated via EDX in the sample material. It does not seem to have a big impact on the overall measured ETC and accuracy of the method but it will limit the maximal lifetime of this sensor and thus the maximal experimental time.

The thermal conductivity of the metal hydride bed in a heat storage reactor is one of a few parameters which determine the overall heat transfer capability in such a system. It had been shown that an increased ETC of the metal hydride lowers the heat resistance of a model tank. Furthermore, the minimum value of the heat resistance appears to be at a larger diameter of a cylindrical heat storage system.

For future work, the ETC of different packing densities could be investigated to gain information about the change of ETC of magnesium hydride powder beds of different porosities. By applying these more precise and diverse values which are valid under working conditions the design of a heat exchanger will be more efficient. This will help to promote the installation of efficient and long-living thermochemical heat storage systems in industrial size (> 100 MW).

Performing in-situ ETC measurements during hydrogenation and dehydrogenation could give additional information about the formation of magnesium iron hydride. Therefore measurement procedures and experiments have to be developed and the set-up has to be improved in order to enable a quasi-stationary state during slow hydrogenation and/or dehydrogenation to facilitate conditions for a proper ETC measurement with the TPS method.

New measurement autoclaves should be developed to simplify the loading with the metal hydrides, to reduce the maintenance time/cost and to exceed the temperature and pressure range to the operating conditions of all metal hydrides.

A. Appendix

A.1. Calculation of the ETC Mean Value

The mean value of the ETC ($\tilde{\kappa}$), the mean absolute deviation (*Mean dev.*) and the relative mean deviation (*Rel. dev.*) was calculated by the following equations:

Mean value of ETC

$$\tilde{\kappa} = \frac{1}{n} \sum_1^n \kappa_i \quad (\text{A.1})$$

Mean absolute deviation

$$\text{Mean dev.} = \frac{1}{n} \sum |\kappa - \tilde{\kappa}| \quad (\text{A.2})$$

Relative mean deviation

$$\text{Rel. dev.} = \frac{\text{Mean dev.}}{\tilde{\kappa}} \cdot 100 \quad (\text{A.3})$$

n is the number of ETC values and is itself a mean value of three ETC measurements.

A. Appendix

Table A.1.: Mean value, mean absolute deviation and relative mean deviation of ETC values of MgH₂ (4 mass – % Ni), calculated using different amounts of data points.

	Data points discarded from the start of transient reading			Mean of 20, 50 & 70
	20	50	70	
20 bar hydrogenated mean value in W m ⁻¹ K ⁻¹	1.919	1.933	1.934	1.929
mean absolute deviation in W m ⁻¹ K ⁻¹	0.027	0.023	0.032	0.006
relative mean deviation in %	1.435	1.224	1.672	0.335
1 bar dehydrogenated mean value in W m ⁻¹ K ⁻¹	6.023	5.895	5.675	5.864
mean absolute deviation in W m ⁻¹ K ⁻¹	0.212	0.148	0.111	0.126
relative mean deviation in %	3.524	2.519	1.960	2.155
7,5 bar dehydrogenated mean value in W m ⁻¹ K ⁻¹	6.799	6.734	6.540	6.691
mean absolute deviation in W m ⁻¹ K ⁻¹	0.174	0.133	0.167	0.100
relative mean deviation in %	2.561	1.977	2.563	1.499
15 bar dehydrogenated mean value in W m ⁻¹ K ⁻¹	7.447	7.437	7.148	7.344
mean absolute deviation in W m ⁻¹ K ⁻¹	0.088	0.031	0.279	0.130
relative mean deviation in %	1.194	0.429	3.907	1.778

A.2. Picture of MgH_2 (4 mass-% Ni) after ETC Measurements

Figure A.1 shows the measurement autoclave (2nd Generation) during the removal of the nickel activated magnesium hydride after 462 hydrogenations in the measurement cell. The gold sealing is deformed during detaching the flange because of the high temperatures caused the sticking of the gold to vessel material.

The powder has a grey appearance and is mostly a loose powder. The powder in the close vicinity of the sensor had formed rather solid pieces, which were hard to break by the usage of a spatula. This is contradicting to the shown particle arrangement shown in Figure 5.9, which predicts a looser particle bed next to sensor, at least on one side. But it is in agreement with predicted inhomogeneous particle distribution, predicted and explained in Chapter 6.8.1. Even though, this picture presents hydrogenated MgH_2 and not in dehydrogenated state. But the volume shrinkage will enhance the inhomogeneous particle distribution, which is in agreement with the resulted ETC values as function of the chosen data points for calculating the ETC (see Figure 6.29 and Figure 6.30).

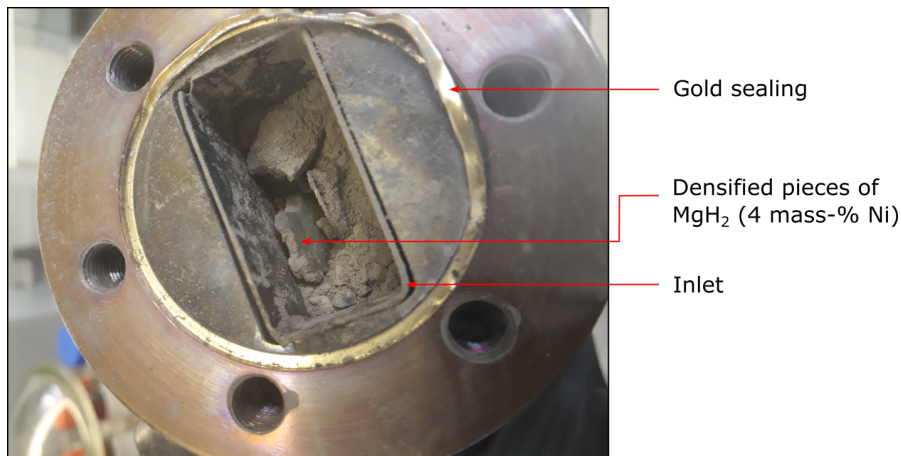


Figure A.1.: MgH_2 (4 mass - % Ni) after 462 cycles of de-/hydrogenation during removing it from the measurement autoclave.

A.3. Equilibrium pressure data of MgH_2 and Mg_2FeH_6

For calculating the equilibrium pressure following equations were used [18, 45, 69]:

MgH_2 :

$$\ln(p_{\text{eq}}) = \frac{-8984.4}{T \text{ in K}} - (-16.2) \quad (\text{A.4})$$

Mg_2FeH_6 :

$$\ln(p_{\text{eq}}) = \frac{-9526.9}{T \text{ in K}} - (-16.5) \quad (\text{A.5})$$

A.3. Equilibrium pressure data of MgH_2 and Mg_2FeH_6

Table A.2.: Equilibrium pressure of MgH_2 and Mg_2FeH_2

T in °C	T in K	p in bar (MgH_2)	p in bar (Mg_2FeH_2)
250	523.15	0.3777	
260	533.15	0.52124	
270	543.15	0.71085	
280	553.15	0.95863	
290	563.15	1.27912	
300	573.15	1.68965	
310	583.15	2.21074	
320	593.15	2.86644	
330	603.15	3.68475	
340	613.15	4.69802	
350	623.15	5.94341	3.35921
360	633.15	7.4633	4.27665
370	643.15	9.30573	5.40393
380	653.15	11.52487	6.77959
390	663.15	14.18144	8.44748
400	673.15	17.34315	10.45714
410	683.15	21.08515	12.86427
420	693.15	25.49044	15.73118
430	703.15	30.65025	19.12723
440	713.15	36.6645	23.12928
450	723.15	43.64207	27.82212
460	733.15	51.70124	33.29889
470	743.15	60.96997	39.66149
480	753.15	71.58619	47.02099
490	763.15	83.69809	55.49799
500	773.15	97.46433	65.22296
510	783.15	113.0543	76.33663
520	793.15	130.64822	88.99025
530	803.15	150.43734	103.34587
540	813.15	172.62404	119.57663
550	823.15	197.42187	137.86697

A.4. Measurement parameters

Table A.3.: Parameters for the measurement of the ETC of Mg, MgH₂, MgH₂ (4 mass – % Ni) and Mg₂FeH₂ in this work. Each reading was performed at least three times and the waiting time between each reading was set to 3 to 10 minutes.

State of the material	Measurement time in s	Heating power in mW
Mg powder (Chapter 6.2)		
x	3-10	50-100
MgH ₂		
Hydrogenated	3-5	100
Dehydrogenated	3-5	100
MgH ₂ (4 mass – % Ni)		
Hydrogenated	5	100
Dehydrogenated	2 and 3	100
	5(after ~ 350 cycles)	200(after ~ 350 cycles)
Mg ₂ FeH ₂		
Hydrogenated	5-10	75
Dehydrogenated	2-3	150

A.5. Thickness and EDX data of Mica sensor

Properties of the TPS sensor before and after the 461 de-/hydrogenation cycles of nickel activated magnesium hydride in the 2nd Generation measurement autoclave.

The thickness of the TPS sensor was measured with a millimeter measuring screw. The sensor had an average thickness of 211.1 μm before the measurements. After the long exposure time to hydrogen gas pressure, temperature and large cycle number the thickness of sensor, which was in direct contact with the MgH_2 was 319.7 μm on average, an increase of 51%. A sign for the delamination of the covering layer, the electrical resistance of the sensor was not influenced by this change.

The EDX analysis of the TPS sensor cover layer shows strong signals for oxygen, which might be a source for further oxygen contamination of the magnesium hydride during the cycle test in Chapter 6.8.1.

Table A.4.: Elemental analysis of TPS sensor cover material (Mica) before and after 461 cycles of de-/hydrogenation of nickel activated magnesium hydride.

Before 459 cycles			After 459 cycles		
Element	Mass-%	Std deviation	Element	Mass-%	Std deviation
O	55.94	0.67	O	32.20	0.09
Na	0.85	0.17	F	0.68	0.07
Al	15.22	0.33	Mg	40.26	0.07
Si	21.45	0.42	Al	8.14	0.03
K	5.55	0.18	Si	12.37	0.04
Fe	0.98	0.13	K	4.16	0.02
			Ca	0.25	0.01
			Fe	1.10	0.02
			Ni	0.83	0.02

A.6. Process feed through

Figure A.2 shows a process feedthrough for four electrical contact wires for high-temperature application by *Spectite* with a magnesium silicate sealing (Lava) sandwiched by two ceramic press bodies. By tightening the process feed through the Lava body will be crushed and form a gas-tight sealing that operates at temperatures up to 870 °C [126].

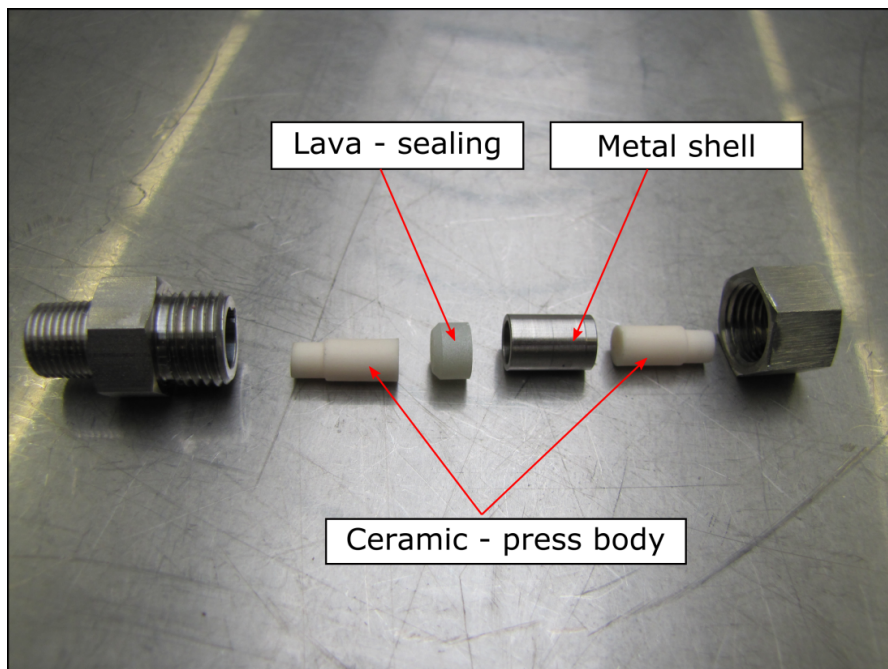


Figure A.2.: Process feedthrough for connecting the sensor.

A.7. XRD data nickel activated magnesium hydride after long term test

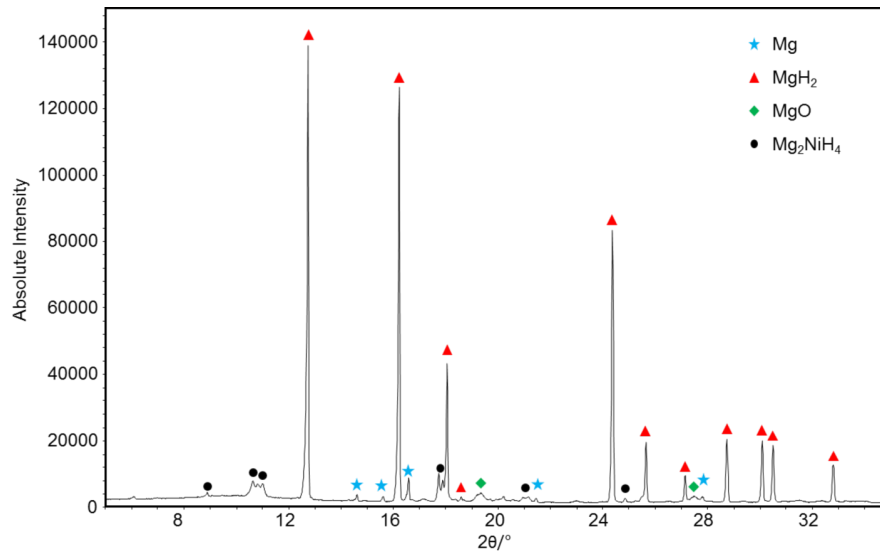


Figure A.3.: XRD pattern of nickel activated magnesium hydride after long term test (510 cycles).

A.8. Mass, gravimetric and packing density of samples.

Table A.5.: Sample mass, volume of respective measurement cells, gravimetric density and packing density of the samples.

Sample	Mass of sample in m	Volume of measurement cell in cm ³	Gravimetric density in g cm ⁻¹	Packing density in %
Mg-powder 1	11.21	17.04	0.65	38
Mg-powder 2	12.03	17.04	0.71	41
MgH ₂	9.82	30.24	0.33	22
MgH ₂ (4 mass – % Ni)	9.60	30.24	0.32	22
Mg ₂ FeH ₂	13.31	44.37	0.30	11

The packing density of the Mg₂FeH₂ was calculated with Equation (6.5) while considering the composition, which was determined by Rietveld analysis in Chapter 6.5.

Table A.6.: Elemental distribution of the magnesium iron hydride sample for calculating the packing density. Measurement cell has a volume of 44.37 cm³. The packing density was calculated to be approximately 11%.

	mass-% in %	Mass in g	Density in g/cm ³	Volume in cm ³
Mg ₂ FeH ₂	0,64	8,4928	2,74	3,099562044
MgH ₂	0,1	1,327	1,45	0,915172414
MgO	0,09	1,1943	3,6	0,33175
Fe	0,16	2,1232	7,874	0,269646939
Mg	0,01	0,1327	1,74	0,076264368
In total	1	13,27		4,692395765

A.9. Raw material cost of common metal hydride systems for high temperature heat storage

Table A.7.: List of raw material presents the cost of high-temperature metal hydrides. Two low-temperature metal hydrides (LTMH) for hydrogen storage are added for comparison reasons [20].

System	Raw material cost in €/kWh _{th}
$\text{Mg} + \text{H}_2 \rightleftharpoons \text{MgH}_2$	2.89
$2\text{Mg} + \text{Fe} + 3\text{H}_2 \rightleftharpoons \text{Mg}_2\text{FeH}_6$	2.25
$\text{Ca} + \text{H}_2 \rightleftharpoons \text{CaH}_2$	2.56
$\text{NaH} + \text{Mg} + \text{H}_2 \rightleftharpoons \text{NaMgH}_3$	4.90
$2\text{CaH}_2 + 3\text{CaSi} \rightleftharpoons \text{Ca}_5\text{Si}_3 + 2\text{H}_2$	15.27
$\text{NaH} + \text{Al} + 1.5\text{H}_2 \rightleftharpoons \text{NaAlH}_4$ (LTMH)	33.66
$\text{TiMn}_{1.5}\text{H}_{2.5}$ (LTMH)	89.95

A.10. Calculation of compressibility factor of hydrogen gas for operating conditions.

For the calculation of the real gas factor Z of the hydrogen in the temperature range of 280 K to 428 K the following equation was applied [24]:

$$Z(p, T) = 1 + (B_0 + B_1T + B_2T^2)p + (C_0 + C_1T + C_2T^2)p^2 \quad (\text{A.6})$$

For gas temperatures from 428 K to 800 K a simplified equation could be used:

$$Z(p, T) = 1 + (B_0 + B_1T + B_2T^2)p \quad (\text{A.7})$$

The maximum values in this work were found to be $Z = 1.06$, for 25 °C and 100 bar pressure.

Table A.8.: Coefficients for calculating the real gas factor of the hydrogen under operating conditions of the heat storage application [24].

B_0	9,66E-03	MPa ⁻¹
B_1	-1,54E-05	MPa ⁻¹ K ⁻¹
B_2	8,23E-09	MPa ⁻¹ K ⁻²
C_0	1,82E-04	MPa ⁻²
C_1	-8,32E-07	MPa ⁻² K ⁻¹
C_2	9,53E-10	MPa ⁻² K ⁻²

A.11. ETC values of Hydrogen Gas

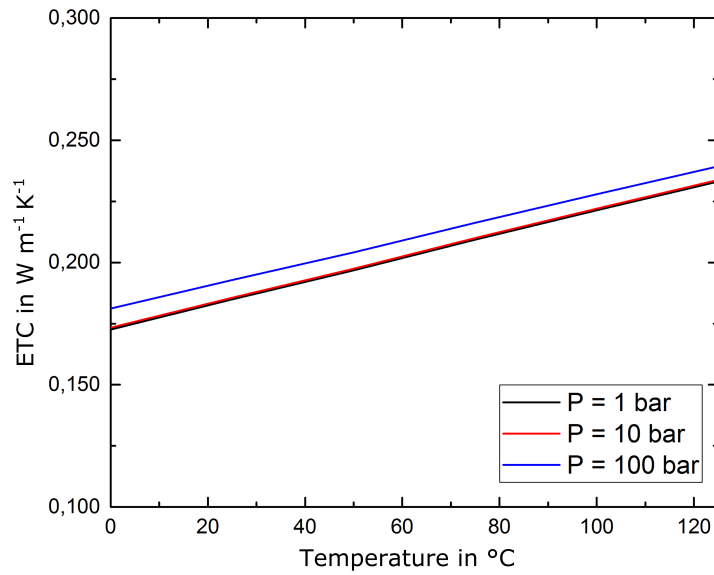


Figure A.4.: ETC of hydrogen gas, plotted with data from [85]

A.12. Technical drawing of first-generation measurement autoclave.

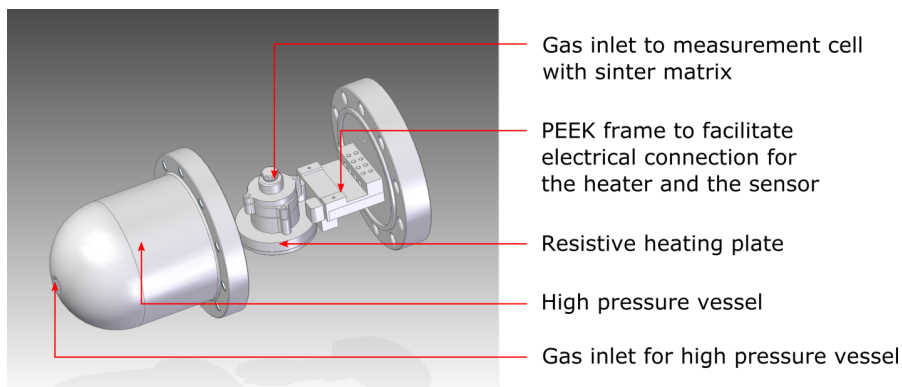


Figure A.5.: Technical sketch of first-generation measurement autoclave.

A.13. Estimation of residual oxygen after purging the test rig with hydrogen

The amount of oxygen was estimated with the ideal gas law. The volume is approximated to be 0.001 m^3 . The temperature is 298 K . For these calculations, it was approximated that the oxygen is removed in each step linearly and no pressure-dependent effects occur.

Table A.9.: Estimation of the amount of oxygen in the test rig during the purging process (Chapter 5).

Amount of oxygen before purging	8.476 mmol
Amount of oxygen after the first evacuation	$8.476 \times 10^{-5} \text{ mmol}$
Amount of oxygen after the second evacuation	$8.476 \times 10^{-10} \text{ mmol}$
Amount of oxygen after the third evacuation	$8.476 \times 10^{-15} \text{ mmol}$
Oxygen to hydrogen ratio after purging procedure	$2.1 \times 10^{-16} \text{ vol} - \%$

Bibliography

- [1] A. Lienkamp, “Klimawandel und gerechtigkeit,” *Politik im Klimawandel, Schönigh; 1st Edition Paderborn-München-Wien-Zürich*, pp. 127–159, 2009.
- [2] Umwelt Bundesamt, “Zu erwartende klimaänderungen bis 2100 — umweltbundesamt,” 2019, url: <https://www.umweltbundesamt.de/themen/klima-energie/klimawandel/zu-erwartende-klimaaenderungen-bis-2100>.
- [3] U.S. Department of Energy, “Clean energy,” 2019, url: <https://www.energy.gov/science-innovation/clean-energy>, accessed 03.07.2019.
- [4] K. Reisswig, “Ein Gastbeitrag: Die drei Säulen der Energiewende: Erzeugung, Verteilung und Speicherung regenerativ erzeugter Energie,” 2013, url: <https://www.next-kraftwerke.de/energie-blog/saeulen-energiewende-erzeugung-verteilung-speicherung>, accessed: 25.09.2019.
- [5] J. Mctigue, *Analysis and optimisation of thermal energy storage*. PhD thesis, St. Catharine’s College Cambridge University Engineering Department, 2016.
- [6] D. Rastler, “Electric energy storage technology options: A white paper primer on applications, costs and benefits,” *Eprî*, p. 170, 2010, url: <http://large.stanford.edu/courses/2012/ph240/doshay1/docs/EPRI.pdf>, accessed: 05.10.2019.
- [7] D.-B. Steber, *Integration of Decentralized Battery Energy Storage Systems into the German Electrical Power System*. PhD thesis, Technischen Fakultät der Friedrich-Alexander-Universität Erlangen-Nürnberg, 2018.
- [8] H. Seidl , S. Mischinger, M. Wolke, E.-L. Limbacher, “Optimierter Einsatz von Speichern für Netz- und Marktanwendungen in der Stromversorgung,” Deutsche Energie-Agentur GmbH (dena), Berlin, Germany, Tech. Rep., 2017.

Bibliography

- [9] R. A. Huggins, *Energy Storage*. Boston, MA: Springer Science+Business Media LLC, 2010.
- [10] M. Felderhoff, R. Urbanczyk, and S. Peil, “Thermochemical heat storage for high temperature applications – a review,” *Green*, vol. 3, no. 2, pp. 113–123, 2013.
- [11] A. Gil, M. Medrano, I. Martorell, A. Lázaro, P. Dolado, B. Zalba, and L. F. Cabeza, “State of the art on high temperature thermal energy storage for power generation. part 1-concepts, materials and modellization,” *Renewable and Sustainable Energy Reviews*, vol. 14, no. 1, pp. 31–55, 2010.
- [12] B. Cárdenas and N. León, “High temperature latent heat thermal energy storage: Phase change materials, design considerations and performance enhancement techniques,” *Renewable and Sustainable Energy Reviews*, vol. 27, pp. 724–737, 2013.
- [13] Zalba, B, Marin J, Cabeza, Luisa F and H. Mehling, “Review on thermal energy storage with phase change: materials, heat transfer analysis and applications,” *Applied Thermal Engineering*, vol. 23, no. 3, pp. 251–283, 2003.
- [14] E. Flores, “A review of latent heat thermal energy storage for concentrated solar plants on the grid,” *The Journal of Undergraduate Research at the University of Illinois at Chicago*, vol. 8, no. 1, 2015.
- [15] P. Pardo, A. Deydier, Z. Anxionnaz-Minvielle, S. Rougé, M. Cabassud, and P. Cognet, “A review on high temperature thermochemical heat energy storage,” *Renewable and Sustainable Energy Reviews*, vol. 32, pp. 591–610, 2014.
- [16] H. Buchner, *Energiespeicherung in Metallhydriden*. Innovative Energietechnik, Vienna: Springer, 1982.
- [17] M. Paskevicius, D. A. Sheppard, K. Williamson, and C. E. Buckley, “Metal hydride thermal heat storage prototype for concentrating solar thermal power,” *Energy*, vol. 88, pp. 469–477, 2015.
- [18] M. Felderhoff and B. Bogdanović, “High temperature metal hydrides as heat storage materials for solar and related applications,” *International Journal of Molecular Sciences*, vol. 10, no. 1, pp. 335–344, 2009.
- [19] D. A. Sheppard, M. Paskevicius, T. D. Humphries, M. Felderhoff, G. Capurso, J. Bellosta von Colbe, M. Dornheim, T. Klassen, P. A. Ward, J. A. Teprovich, C. Corgnale, R. Zidan, D. M. Grant, and C. E. Buckley, “Metal hydrides for concentrating solar thermal power energy storage,” *Applied*

- Physics A*, vol. 122, no. 4, p. 395, 2016.
- [20] K. Manickam, P. Mistry, G. Walker, D. Grant, C. E. Buckley, T. D. Humphries, M. Paskevicius, T. Jensen, R. Albert, K. Peinecke, and M. Felderhoff, “Future perspectives of thermal energy storage with metal hydrides,” *International Journal of Hydrogen Energy*, vol. 44, no. 15, 2019.
- [21] A. Hauer, A. Wörner, S. Kranz, P. Schumacher, S. Gschwander, J. von Appen, D. Hidalgo, B. Groß, and G. Katherina, “Wärmespeicher : Rolle im Energiesystem der Zukunft,” Presentation, Jahrestagung Forschungsverbund erneubare energien, 2014, url: https://elib.dlr.de/94300/1/FVEE_30_Hauer.pdf accessed: 05.10.2019.
- [22] DLR, “Wärme speichern in Kalk - effizienter durch Bewegung - Forschung Energiespeicher,” 2019, https://forschung-energiespeicher.info/waerme-speichern/projektliste/projekt-einzelansicht/108/Waerme_speichern_in_Kalk_effizienter_durch_Bewegung/, accessed: 08.07.2019.
- [23] V. A. Yartys, M. V. Lototsky, E. Akiba, R. Albert, V. E. Antonov, J. R. Ares, M. Baricco, N. Bourgeois, C. E. Buckley, J. M. Bellosta von Colbe, J.-C. Crivello, F. Cuevas, R. V. Denys, M. Dornheim, M. Felderhoff, D. M. Grant, B. C. Hauback, T. D. Humphries, I. Jacob, T. R. Jensen, P. E. de Jongh, J.-M. Joubert, M. A. Kuzovnikov, M. Latroche, M. Paskevicius, L. Pasquini, L. Popilevsky, V. M. Skripnyuk, E. Rabkin, M. V. Sofianos, A. Stuart, G. Walker, H. Wang, C. J. Webb, and M. Zhu, “Magnesium based materials for hydrogen based energy storage: Past, present and future,” *International Journal of Hydrogen Energy*, vol. 44, no. 15, pp. 7809–7859, 2019.
- [24] G. Friedlmeier, *Charakterisierung von Hochtemperatur-Metallhydriden auf Magnesium-Basis*. PhD thesis, ULB Düsseldorf, 1997.
- [25] J. J. Reilly and R. H. Wiswall, “Formation and properties of iron titanium hydride,” *Inorganic Chemistry*, vol. 13, no. 1, pp. 218–222, 1974.
- [26] M. Danaie, A. A. C. Asselli, J. Huot, and G. a. Botton, “Formation of the ternary complex hydride Mg_2FeH_6 from magnesium hydride (β - MgH_2) and iron: an electron microscopy and energy-loss spectroscopy study,” *The Journal of Physical Chemistry C*, vol. 116, pp. 25701–25714, 2012.
- [27] R. Urbanczyk, *Experimentelle Untersuchung der thermischen Kopplung*

Bibliography

- einer HT-PEM Brennstoffzelle mit einem Wasserstoffspeicher auf Basis von Natriumalanat.* PhD thesis, Universität Duisburg-Essen, 2013.
- [28] A. Züttel, A. Borgschulte, and L. Schlapbach, *Hydrogen as a Future Energy Carrier*. Weinheim: Wiley, 2008.
- [29] G. A. Lozano Martinez, *Development of hydrogen storage systems using Sodium alanate*. PhD thesis, Technischen Universität Hamburg-Harburg, 2011.
- [30] Ubbelohde, Alfred Rene Jean Paul, “Some properties of the metallic state I—Metallic hydrogen and its alloys,” *Proceedings of the royal society A*, vol. 159, no. 897, 1937.
- [31] Toshiba, “Utilizing hydrogen for a new approach to the supply of energy,” url: <https://www.toshiba-energy.com/en/hydrogen/product/h2one.htm>, accessed: 06.05.2019.
- [32] T. M. Pavlović, I. S. Radonjić, D. D. Milosavljević, and L. S. Pantić, “A review of concentrating solar power plants in the world and their potential use in serbia,” *Renewable and Sustainable Energy Reviews*, vol. 16, no. 6, pp. 3891–3902, 2012.
- [33] Clarke Energy, “Cogeneration / combined heat and power (CHP),” url: <http://www.clarke-energy.com/chp-cogeneration>, accessed: 06.05.2019.
- [34] X. Qu, Y. Li, P. Li, Q. Wan, and F. Zhai, “The development of metal hydrides using as concentrating solar thermal storage materials,” *Frontiers of Materials Science*, vol. 9, no. 4, pp. 317–331, 2015.
- [35] Solar Energy Technologies Office, “The sunshot 2030 goals,” 2017, url: <https://www.energy.gov/sites/prod/files/2018/05/f51/SunShot%202030%20Fact%20Sheet.pdf>, accessed 05.06.2019.
- [36] C. Corgnale, B. Hardy, T. Motyka, R. Zidan, J. Teprovich, and B. Peters, “Screening analysis of metal hydride based thermal energy storage systems for concentrating solar power plants,” *Renewable and Sustainable Energy Reviews*, vol. 38, pp. 821–833, 2014.
- [37] T. Motyka, “Low-Cost MH TES Systems for CSP,” CSP Program Review, April 23, 2013.
- [38] P. A. Ward, C. Corgnale, J. A. Teprovich, T. Motyka, B. Hardy, D. Sheppard, C. Buckley, and R. Zidan, “Technical challenges and future direction for high-

- efficiency metal hydride thermal energy storage systems,” *Applied Physics A: Materials Science and Processing*, vol. 122, no. 4, 2016.
- [39] Q. Lai, M. Paskevicius, D. A. Sheppard, C. E. Buckley, A. W. Thornton, M. R. Hill, Q. Gu, J. Mao, Z. Huang, H. K. Liu, Z. Guo, A. Banerjee, S. Chakraborty, R. Ahuja, and K. F. Aguey-Zinsou, “Hydrogen storage materials for mobile and stationary applications: Current state of the art,” *ChemSusChem*, vol. 8, no. 17, pp. 2789–2825, 2015.
- [40] A. M. Abdalla, S. Hossain, O. B. Nisfindy, A. T. Azad, M. Dawood, and A. K. Azad, “Hydrogen production, storage, transportation and key challenges with applications: A review,” *Energy Conversion and Management*, vol. 165, pp. 602–627, 2018.
- [41] S. M. Aceves, F. Espinosa-loza, E. Ledesma-orozco, T. O. Ross, A. H. Weisberg, T. C. Brunner, and O. Kircher, “High-density automotive hydrogen storage with cryogenic capable pressure vessels,” *International Journal of Hydrogen Energy*, vol. 35, no. 3, pp. 1219–1226, 2010.
- [42] D. A. Sheppard and C. E. Buckley, “The potential of metal hydrides paired with compressed hydrogen as thermal energy storage for concentrating solar power plants,” *International Journal of Hydrogen Energy*, vol. 44, no. 18, pp. 9143–9163, 2019.
- [43] B. Li, J. Li, H. Shao, and L. He, “Mg-based hydrogen absorbing materials for thermal energy storage—a review,” *Applied Sciences*, vol. 8, no. 8, p. 1375, 2018.
- [44] B. Bogdanović, A. Ritter, B. Spliethoff, and K. Straßburger, “A process steam generator based on the high temperature magnesium hydride/magnesium heat storage system,” *International Journal of Hydrogen Energy*, vol. 20, no. 10, pp. 811–822, 1995.
- [45] A. Reiser, B. Bogdanović, and K. Schlichte, “Application of Mg-based metal-hydrides as heat energy storage systems,” *International Journal of Hydrogen Energy*, vol. 25, no. 5, pp. 425–430, 2000.
- [46] B. Bogdanović, H. Hofmann, A. Neuy, A. Reiser, K. Schlichte, B. Spliethoff, and S. Wessel, “Ni-doped versus undoped Mg-MgH₂ materials for high temperature heat or hydrogen storage,” *Journal of Alloys and Compounds*, vol. 292, no. 1-2, pp. 57–71, 1999.
- [47] B. Bogdanović, S.-t. Liao, M. Schwickardi, P. Sikorsky, and B. Spliethoff,

Bibliography

- “Katalytische Synthese von Magnesiumhydrid unter milden Bedingungen,” *Angewandte Chemie*, vol. 92, no. 10, pp. 845–846, 1980.
- [48] A. Léon, “Summary for policymakers,” *Convection in Porous Media*, vol. 53, no. 9, 2013.
- [49] M. M. Antonova and R. A. Morozova, *Preparatory chemistry of hydrides*. Kiev, Ukraine: Naukova Dumka, 1967.
- [50] B. Bogdanović, “The development, testing and optimization of energy storage materials based on the MgH_2 -Mg system,” *International Journal of Hydrogen Energy*, vol. 18, no. 7, pp. 575–589, 1993.
- [51] S. Ono, Y. Ishido, K. Imanari, T. Tabata, N. Chemical, M. Doyama, Y. K. Cho, and R. Yamaioto, “Phase transformation and thermal expansion of Mg-Ni alloys in a hydrogen atmosphere,” *Journal of the Less-Common Metals*, vol. 88, pp. 57–61, 1982.
- [52] J. Kapischke and J. Hapke, “Measurement of the effective thermal conductivity of a metal hydride bed with chemical reaction,” *Experimental Thermal and Fluid Science*, vol. 9, no. 3, pp. 337–344, 1994.
- [53] J. C. Crivello, B. Dam, R. V. Denys, M. Dornheim, D. M. Grant, J. Huot, T. R. Jensen, P. de Jongh, M. Latroche, C. Milanese, D. Milčius, G. S. Walker, C. J. Webb, C. Zlotea, and V. A. Yartys, “Review of magnesium hydride-based materials: development and optimisation,” *Applied Physics A: Materials Science and Processing*, vol. 122, no. 2, pp. 1–20, 2016.
- [54] C. J. Webb, “A review of catalyst-enhanced magnesium hydride as a hydrogen storage material,” *Journal of Physics and Chemistry of Solids*, vol. 84, no. 1, pp. 96–106, 2015.
- [55] G. Liang, J. Huot, S. Boily, A. van Neste, and R. Schulz, “Catalytic effect of transition metals on hydrogen sorption in nanocrystalline ball milled MgH_2 -Tm (Tm=Ti, V, Mn, Fe and Ni) systems,” *Journal of Alloys and Compounds*, vol. 292, no. 1-2, pp. 247–252, 1999.
- [56] G. Barkhordarian, T. Klassen, and R. Bormann, “Catalytic mechanism of transition-metal compounds on Mg hydrogen sorption reaction,” *Journal of Physical Chemistry B*, vol. 110, no. 22, pp. 11020–11024, 2006.
- [57] A. Montone, A. Aurora, D. M. Gattia, and M. V. Antisari, “Microstructural and kinetic evolution of Fe doped MgH_2 during H_2 cycling,” *Catalysts*, vol. 2, no. 4, pp. 400–411, 2012.

- [58] G. Barkhordarian, T. Klassen, and R. U. Bormann, "Effect of Nb_2O_5 content on hydrogen reaction kinetics of Mg," *Journal of Alloys and Compounds*, vol. 364, no. 1-2, pp. 242–246, 2004.
- [59] V. V. Bhat, A. Rougier, L. Aymard, X. Darok, G. Nazri, and J. M. Tarascon, "Catalytic activity of oxides and halides on hydrogen storage of MgH_2 ," *Journal of Power Sources*, vol. 159, no. 1 SPEC. ISS, pp. 107–110, 2006.
- [60] J.-R. Ares-Fernández and K.-F. Aguey-Zinsou, "Superior MgH_2 kinetics with MgO addition: A tribological effect," *Catalysts*, vol. 2, no. 4, pp. 330–343, 2012.
- [61] M. Lototskyy, M. W. Davids, J. M. Sibanyoni, J. Goh, and B. G. Pollet, "Magnesium-based hydrogen storage nanomaterials prepared by high energy reactive ball milling in hydrogen at the presence of mixed titanium-iron oxide," *Journal of Alloys and Compounds*, vol. 645, no. S1, pp. S454–S459, 2015.
- [62] N. Hanada, T. Ichikawa, and H. Fujii, "Catalytic effect of nanoparticle 3d-transition metals on hydrogen storage properties in magnesium hydride MgH_2 prepared by mechanical milling," *Journal of Physical Chemistry B*, vol. 109, no. 15, pp. 7188–7194, 2005.
- [63] T. Sadhasivam, H. T. Kim, S. Jung, S. H. Roh, J. H. Park, and H. Y. Jung, "Dimensional effects of nanostructured Mg/ MgH_2 for hydrogen storage applications: A review," *Renewable and Sustainable Energy Reviews*, vol. 72, pp. 523–534, 2017.
- [64] O. Friedrichs, J. C. Sánchez-López, C. López-Cartes, T. Klassen, R. Bormann, and A. Fernández, " Nb_2O_5 pathway effect on hydrogen sorption in Mg," *Journal of Physical Chemistry B*, vol. 110, no. 15, pp. 7845–7850, 2006.
- [65] B. Wu, H. Ma, Z. Pan, J. Wang, W. Qu, and B. Wang, "Drying and quality characteristics and models of carrot slices under catalytic infrared heating," *International Agricultural Engineering Journal*, vol. 23, no. 2, pp. 70–79, 2014.
- [66] K. Edalati, K. Kitabayashi, Y. Ikeda, J. Matsuda, H. W. Li, I. Tanaka, E. Akiba, and Z. Horita, "Bulk nanocrystalline gamma magnesium hydride with low dehydrogenation temperature stabilized by plastic straining via high-pressure torsion," *Scripta Materialia*, vol. 157, pp. 54–57, 2018.
- [67] M. Matsuura, H. Sudoh, and T. Ohnuma, "Synthesis of MgH_2 and Mg_2NiH_4

Bibliography

- by ball milling under the hydrogen gas and their hydrogen absorption characteristics,” *Journal of Metastable and Nanocrystalline Materials*, vol. 20-21, pp. 343–348, 2009.
- [68] A. Zaluska, L. Zaluski, and J. O. Ström-Olsen, “Nanocrystalline magnesium for hydrogen storage,” *Journal of Alloys and Compounds*, vol. 288, no. 1-2, pp. 217–225, 1999.
- [69] B. Bogdanović, A. Reiser, K. Schlichte, B. Spliethoff, and B. Tesche, “Thermodynamics and dynamics of the Mg-Fe-H system and its potential for thermochemical thermal energy storage,” *Journal of Alloys and Compounds*, vol. 345, no. 1-2, pp. 77–89, 2002.
- [70] M. T. Fernández-Díaz, M. Retuerto, C. A. Garcia-Ramos, J. Sánchez-Benítez, R. Martínez, F. Jiménez-Villacorta, T. Ruskov, and J. A. Alonso, “Neutron powder diffraction, x-ray absorption and Mössbauer spectroscopy on Mg₂FeH₆,” *International Journal of Hydrogen Energy*, vol. 40, no. 30, pp. 9306–9313, 2015.
- [71] J. Puszkiel, M. Castro Riglos, J. Ramallo-López, M. Mizrahi, T. Gemming, C. Pistidda, P. Arneodo Larochette, J. Bellosta von Colbe, T. Klassen, M. Dornheim, and F. Gennari, “New insight on the hydrogen absorption evolution of the Mg-Fe-H system under equilibrium conditions,” *Metals*, vol. 8, no. 11, p. 967, 2018.
- [72] *VDI Heat Atlas*. VDI-Buch, Berlin: Springer-Verlag Berlin Heidelberg, 2. ed., 2010.
- [73] E. Tsotsas and H. Martin, “Thermal conductivity of packed beds: A review,” *Chemical Engineering and Processing*, vol. 22, no. 1, pp. 19–37, 1987.
- [74] R. Wulf, *Wärmeleitfähigkeit von hitzebeständigen und feuerfesten Dämmstoffen - Untersuchungen zu Ursachen für unterschiedliche Messergebnisse bei Verwendung verschiedener Messverfahren*. PhD thesis, Technische Universität Bergakademie Freiberg, 2009.
- [75] Y. Asakuma, M. Asada, Y. Kanazawa, and T. Yamamoto, “Thermal analysis with contact resistance of packed bed by a homogenization method,” *Powder Technology*, vol. 291, pp. 46–51, 2016.
- [76] M. Elstner, *Physikalische Chemie I: Thermodynamik und Kinetik*. Berlin, Heidelberg: Springer Berlin Heidelberg, 2017.
- [77] D. Wenger, *Metallhydridspeicher zur Wasserstoffversorgung und Kühlung*

- von Brennstoffzellenfahrzeugen. PhD thesis, Technische Universität München, 2009.
- [78] D. Hänel, *Molekulare Gasdynamik*. Berlin/Heidelberg: Springer-Verlag, 2006.
- [79] S. Parzinger, *Analytische Modellierung der temperatur- und gasdruck-abhängigen effektiven Wärmeleitfähigkeit von Pulvern*. PhD thesis, Technische Universität München, 2014.
- [80] C. Kittel, *Einführung in die Festkörperphysik*. München: Oldenbourg, 14 ed., 2006.
- [81] K. Kopitzki and P. Herzog, *Einführung in die Festkörperphysik*. Berlin, Heidelberg: Springer Berlin Heidelberg, 2017.
- [82] K. C. Smith and T. S. Fisher, “Models for metal hydride particle shape, packing, and heat transfer,” *International Journal of Hydrogen Energy*, vol. 37, no. 18, pp. 13417–13428, 2012.
- [83] J. Kapischke and J. Hapke, “Measurement of the effective thermal conductivity of a Mg-MgH₂ packed bed with oscillating heating,” *Experimental Thermal and Fluid Science*, vol. 17, no. 4, pp. 347–355, 1998.
- [84] C. M. Wang, Y. U. Chen, and S. F. Xiao, “Situation of research and development of thermal conductive magnesium alloys,” *Rare Metal Materials and Engineering*, vol. 44, no. 10, pp. 2596–2600, 2015.
- [85] The engineering toolbox - online calculator, figures and table showing thermal conductivity of hydrogen, H₂, at varying temperature and pressure, url: https://www.engineeringtoolbox.com/hydrogen-H2-thermal-conductivity-temperature-pressure-d_2106.html, accessed: 09.10.2019.
- [86] P. G. Klemens, K.-H. Hellwege, H. Landolt, R. Börnstein, and O. Madelung, eds., *Landolt-Börnstein Numerical data and functional relationships in science and technology: new series*. Berlin: Springer, 1991.
- [87] “Physical properties of magnesium,” International Magnesium Association, 2019, url: https://www.intlmag.org/page/basics_phys_prop_ima, accessed: 17.09.2019.
- [88] Kallweit, J.Hahne, E, “Effective thermal conductivity of metal hydride powders: measurement and theoretical modelling,” *Int. J. Heat Mass Transf.*, pp. 373–378, 1994.

Bibliography

- [89] M. Wierse, R. Werner, and M. Groll, “Magnesium hydride for thermal energy storage in a small-scale solar-thermal power station,” *Journal of The Less-Common Metals*, vol. 172-174, no. 3, pp. 1111–1121, 1991.
- [90] ASTM E1225-13, *Test Method for Thermal Conductivity of Solids Using the Guarded-Comparative-Longitudinal Heat Flow Technique*. West Conshohocken, PA: ASTM International, 2013.
- [91] C. V. Madhusudana, *Thermal Contact Conductance*. Mechanical Engineering Series, New York, NY: Springer, 1996.
- [92] A. Palacios, L. Cong, M. E. Navarro, Y. Ding, and C. Barreneche, “Thermal conductivity measurement techniques for characterizing thermal energy storage materials – a review,” *Renewable and Sustainable Energy Reviews*, vol. 108, pp. 32–52, 2019.
- [93] “ISO 22007-1:2015(E): Determination of thermal conductivity and thermal diffusivity,” tech. rep., International Organization for Standardization, 2017.
- [94] Hot Disk, *Hot Disk Thermal Constants Analyser Instruction Manual*, 3 ed., Apr. 2015.
- [95] J. Kallweit, *Effektive Wärmeleitfähigkeit von Metallhydrid-Materialien zur Speicherung von Wasserstoff*. PhD thesis, Universität Stuttgart, 1994.
- [96] Y. Ishido, M. Kawamura, and S. Ono, “Thermal conductivity of magnesium-nickel hydride powder beds in a hydrogen atmosphere,” *International Journal of Hydrogen Energy*, vol. 7, no. 2, pp. 173–182, 1982.
- [97] C. M. Stander and R. A. Pacey, “The lattice energy of magnesium hydride,” *Journal of Physics and Chemistry of Solids*, vol. 39, no. 8, pp. 829–832, 1978.
- [98] A. Chaise, P. de Rango, P. Marty, and D. Fruchart, “Experimental and numerical study of a magnesium hydride tank,” *International Journal of Hydrogen Energy*, vol. 35, no. 12, pp. 6311–6322, 2010.
- [99] T. M. Tritt, *Thermal Conductivity: Theory, Properties, and Applications*. Physics of Solids and Liquids, Boston, MA: Kluwer Academic/Plenum Publishers New York, 2004.
- [100] D. Zhao, X. Qian, X. Gu, S. A. Jajja, and R. Yang, “Measurement techniques for thermal conductivity and interfacial thermal conductance of bulk and thin film materials,” *Journal of Electronic Packaging*, vol. 138, no. 4, p. 040802, 2016.

- [101] Hot Disk, *Instruction Manual Hot Disk Thermal Constants Analyser Software Version 6.1*, 1 ed., Oct. 2011.
- [102] W. A. Deer, R. A. Howie, J. Zussman, W. A. Deer, and R. A. Howie, *An introduction to the rock-forming minerals*. Harlow, Essex: Longman, 1969.
- [103] P. Haines, P. G. Laye, S. B. Warrington, T. M. Group, G. R. Heal, D. M. Price, and R. Wilson, *Principles of Thermal Analysis and Calorimetry*, vol. v.29 of *RSC Paperbacks*. Cambridge: Royal Society of Chemistry, 2002.
- [104] Pacific Northwest National Laboratory, “H₂ tools: Basic hydrogen properties,” url: <https://h2tools.org/hyarc/hydrogen-data/basic-hydrogen-properties>, accessed: 05.04.2019.
- [105] U. Reinert, “Zusatzinfos zur Folie: Einfluß von Legierungselementen,” url: https://www.hs-bremen.de/internet/hsb/struktur/mitarbeiter/schubert/lehrveranstaltungen/werk/materialien/118_zusatzinfos_einflu...legierungselemente.pdf, accessed: 08.10.2019.
- [106] Metalcor GmbH, “Datenblatt 1.4980 (AISI 660),” url: <http://www.metalcor.de/datenblatt/78/>, accessed: 19.03.2019.
- [107] PSW GmbH, “Werkstoffe und ihre Zusammensetzung,” url: http://www.psw-gmbh.de/fileadmin/user_upload/technik/Allgemeines/3_Werkstoffe_und_ihre_Zusammensetzung007.pdf, accessed: 19.03.2019.
- [108] VDM Metals, “Aluchrom Y Hf, Werkstoffdatenblatt Nr. 4149,” 2017.
- [109] K. Schlichte, “Bericht 8-97 Die verwendeten Werkstoffe bei Zyklenversuchen,” MPI Bericht, 1997.
- [110] A. Reiser, *Untersuchung der Systeme Mg-MgH₂ und Mg-Fe-Mg₂FeH₆ als Wärmespeichermaterialien in einem Temperaturbereich um 500 °C*. PhD thesis, Universität Erlangen-Nürnberg, 1998.
- [111] W. Dai, S. Papeschi, D. Hanaor, and Y. Gan, “Influence of gas pressure on the effective thermal conductivity of ceramic breeder pebble beds,” *Fusion Engineering and Design*, vol. 118, pp. 45–51, 2017.
- [112] M. Bahrami, M. M. Yovanovich, and J. R. Culham, “Effective thermal conductivity of rough spherical packed beds,” *International Journal of Heat and Mass Transfer*, vol. 49, no. 19-20, pp. 3691–3701, 2006.
- [113] “Magnesiumhydrid,” url: <https://roempp.thieme.de/roempp4.0/do/data/RD-13-00126>, accessed: 25.09.2019.

Bibliography

- [114] S. D. Beattie, U. Setthanan, and G. S. McGrady, “Thermal desorption of hydrogen from magnesium hydride (MgH_2): An in situ microscopy study by environmental SEM and TEM,” *International Journal of Hydrogen Energy*, vol. 36, no. 10, pp. 6014–6021, 2011.
- [115] F. S. Yang, G. X. Wang, Z. X. Zhang, X. Y. Meng, and V. Rudolph, “Design of the metal hydride reactors - a review on the key technical issues,” *International Journal of Hydrogen Energy*, vol. 35, no. 8, pp. 3832–3840, 2010.
- [116] M. Verga, F. Armanasco, C. Guardamagna, C. Valli, A. Bianchin, F. Agresti, S. Lo Russo, A. Maddalena, and G. Principi, “Scaling up effects of Mg hydride in a temperature and pressure-controlled hydrogen storage device,” *International Journal of Hydrogen Energy*, vol. 34, no. 10, pp. 4602–4610, 2009.
- [117] J. Murray, H. Miller, P. Bird, and A. J. Goudy, “The effect of particle size and surface composition on the reaction rates of some hydrogen storage alloys,” *Journal of Alloys and Compounds*, vol. 231, no. 1-2, pp. 841–845, 1995.
- [118] S. Shriniwasan and S. S. V. Tatiparti, “Effect of Mg shell on MgH_2 dehydrogenation by morphological and mathematical analysis,” *Nanomaterials and Energy*, vol. 8, no. 2, pp. 1–10, 2019.
- [119] J. J. Reilly and R. H. Wiswall, “The reaction of hydrogen with alloys of magnesium and nickel and the formation of Mg_2NiH_4 ,” *Inorganic Chemistry*, vol. 7, no. 11, pp. 2254–2256, 1968.
- [120] D. E. Dedrick, M. P. Kanouff, B. C. Replogle, and K. J. Gross, “Thermal properties characterization of sodium alanates,” *Journal of Alloys and Compounds*, vol. 389, no. 1-2, pp. 299–305, 2005.
- [121] A. R. Sánchez, H. P. Klein, and M. Groll, “Expanded graphite as heat transfer matrix in metal hydride beds,” *International Journal of Hydrogen Energy*, vol. 28, no. 5, pp. 515–527, 2003.
- [122] Konoshima, “Magnesium compounds for thermal conductive fillers,” url: <http://www.konoshima.co.jp/eng/resdev/resdev04.html>, accessed: 25.09.2019.
- [123] M. Winter, “The periodic table of the elements by WebElements,” url: <https://www.webelements.com/>, accessed: 25.09.2019.
- [124] “Methods and results: Technical Committee ISO/TC 69, Applications of

- statistical methods,” tech. rep., International Organization for Standardization, Subcommittee SC 6, 1994.
- [125] M. Polanski, T. K. Nielsen, Y. Cerenius, J. Bystrzycki, and T. R. Jensen, “Synthesis and decomposition mechanisms of Mg_2FeH_6 studied by in-situ synchrotron X-ray diffraction and high-pressure DSC,” *International Journal of Hydrogen Energy*, vol. 35, no. 8, pp. 3578–3582, 2010.
- [126] Spectite inc., “Spectite pressure and vacuum sealed feedthroughs, sealing glands for process applications,” 2019, url: <http://www.spectite.com/general.htm>, accessed: 03.05.2019.